

# ATLASGAL-selected high-mass clumps in the inner Galaxy. VII. Characterisation of mid- $J$ CO emission

F. Navarete<sup>1,2</sup>, S. Leurini<sup>3,1</sup>, A. Giannetti<sup>4,1</sup>, F. Wyrowski<sup>1</sup>, J. S. Urquhart<sup>5,1</sup>,  
C. König<sup>1</sup>, T. Csengeri<sup>1</sup>, R. Güsten<sup>1</sup>, A. Daminieli<sup>2</sup>, and K. M. Menten<sup>1</sup>

<sup>1</sup> Max-Planck-Institut für Radioastronomie, Auf dem Hügel 69, 53121 Bonn, Germany  
e-mail: fnavarete@mpi.fr-bonn.mpg.de

<sup>2</sup> Universidade de São Paulo, Instituto de Astronomia, Geofísica e Ciências Atmosféricas, Departamento de Astronomia,  
Rua do Matão 1226, Cidade Universitária São Paulo-SP, 05508-090, Brazil

<sup>3</sup> INAF - Osservatorio Astronomico di Cagliari, Via della Scienza 5, I-09047, Selargius (CA)

<sup>4</sup> INAF - Istituto di Radioastronomia & Italian ALMA Regional Centre, Via P. Gobetti 101, I-40129 Bologna, Italy

<sup>5</sup> Centre for Astrophysics and Planetary Science, The University of Kent, Canterbury, Kent CT2 7NH, UK

## ABSTRACT

*Context.* High-mass stars are formed within massive molecular clumps, where a large number of stars form close together. The evolution of the clumps with different masses and luminosities is mainly regulated by its high-mass stellar content and the formation of such objects is still not well understood.

*Aims.* In this work, we characterise the mid- $J$  CO emission in a statistical sample of 99 clumps (TOP100) selected from the ATLASGAL survey that are representative of the Galactic proto-cluster population.

*Methods.* High-spatial resolution APEX-CHAMP<sup>+</sup> maps of the CO (6–5) and CO (7–6) transitions were obtained and combined with additional single-pointing APEX-FLASH<sup>+</sup> spectra of the CO (4–3) line. The data were convolved to a common angular resolution of 13''4. We analysed the line profiles by fitting the spectra with up to three Gaussian components, classified as narrow or broad, and computed CO line luminosities for each transition. Additionally, we defined a distance-limited sample of 72 sources within 5 kpc to check the robustness of our analysis against beam dilution effects. We have studied the correlations of the line luminosities and profiles for the three CO transitions with the clump properties and investigate if and how they change as a function of the evolution.

*Results.* All sources were detected above  $3\text{-}\sigma$  in all three CO transitions and most of the sources exhibit broad CO emission likely associated with molecular outflows. We find that the extension of the mid- $J$  CO emission is correlated with the size of the dust emission traced by the Herschel-PACS  $70\mu\text{m}$  maps. The CO line luminosity ( $L_{\text{CO}}$ ) is correlated with the luminosity and mass of the clumps. However, it does not correlate with the luminosity-to-mass ratio.

*Conclusions.* The dependency of the CO luminosity with the properties of the clumps is steeper for higher- $J$  transitions. Our data seem to exclude that this trend is biased by self-absorption features in the CO emission, but rather suggest that different  $J$  transitions arise from different regions of the inner envelope. Moreover, high-mass clumps show similar trends in CO luminosity as lower mass clumps, but are systematically offset towards larger values, suggesting that higher column density and (or) temperature (of unresolved) CO emitters are found inside high-mass clumps.

**Key words.** stars: formation – stars: protostars – ISM: molecules – ISM: kinematics and dynamics – line: profiles

## 1. Introduction

High-mass stars are responsible for the dynamical and chemical evolution of the interstellar medium and of their host galaxies by injecting heavier elements and energy in their surrounding environment by means of their strong UV emission and winds. Despite their importance, the processes that lead to the formation of high-mass stars are still not well understood (Zinnecker & Yorke 2007).

Observations at high-angular resolution have confirmed a high degree of multiplicity for high-mass stars, suggesting these objects are not formed in isolated systems (Grellmann et al. 2013). The same scenario is supported by three-dimensional simulations of high-mass star formation (Krumholz et al. 2009; Rosen et al. 2016). These objects are formed on a relatively short timescale ( $\sim 10^5$  yr), requiring large accretion rates ( $\sim 10^{-4} M_{\odot} \text{ yr}^{-1}$ , Hosokawa & Omukai 2009). Such conditions can only be achieved in the densest clumps in molecular

clouds, with sizes of  $\lesssim 1$  pc and masses of order  $100\text{--}1000 M_{\odot}$  (Bergin & Tafalla 2007). These clumps are associated with large visual extinctions, thus observations at long wavelengths are required to study their properties and the star formation process.

After molecular hydrogen ( $\text{H}_2$ ), which is difficult to observe directly in dense cold gas, carbon monoxide (CO) is the most abundant molecular species. Thus, rotational transitions of CO are commonly used to investigate the physics and kinematics of star-forming regions (SFRs). Traditionally, observations of CO transitions with low angular momentum quantum number  $J$  from  $J=1\text{--}0$  to  $4\text{--}3$  (here defined as low- $J$  transitions) have been used for this purpose (e.g. see Schulz et al. 1995, Zhang et al. 2001 and Beuther et al. 2002). These lines have upper level energies,  $E_u$ , lower than 55 K and are easily excited at relatively low temperatures and moderate densities. Therefore, low- $J$  CO lines are not selective tracers of the densest regions of SFRs, but are contaminated by emission from the ambient molecular cloud. On the other hand, higher- $J$  CO transitions are less contami-

nated by ambient gas emission and likely probe the warm gas directly associated with embedded young stellar objects (YSOs). In this paper we make use of the  $J=6-5$  and  $7-6$  lines of CO, with  $E_u \sim 116$  K and 155 K, respectively, and in the following we refer to them simply as mid- $J$  CO transitions. Over the past decade the Atacama Pathfinder Experiment telescope (APEX<sup>1</sup>, Güsten et al. 2006) has enabled routine observations of mid- $J$  CO lines, while *Herschel* and SOFIA have opened the possibility of spectroscopically resolved observations of even higher- $J$  transitions ( $J=10-9$  and higher, e.g. Gómez-Ruiz et al. 2012; San José-García et al. 2013, hereafter, SJG13 ; Leurini et al. 2015; Mottram et al. 2017). van Kempen et al. (2009a, hereafter, vK09) and van Kempen et al. (2009b) have shown the importance of mid- $J$  CO transitions in tracing warm gas in the envelopes and outflows of low-mass protostars. More recently, SJG13 used the High Frequency Instrument for the Far Infrared (HIFI, de Graauw et al. 2010) on board of *Herschel* to study a sample of low- and high-mass star-forming regions in high- $J$  transitions of several CO isotopologues (e.g. CO, <sup>13</sup>CO and C<sup>18</sup>O  $J=10-9$ ), finding that the link between entrained outflowing gas and envelope motions is independent of the source mass.

In this paper, we present CO ( $6-5$ ) and CO ( $7-6$ ) maps towards a sample of 99 high-mass clumps selected from the APEX Telescope Large Area Survey of the Galaxy (ATLASGAL), which has provided an unbiased coverage of the plane of the inner Milky Way in the continuum emission at  $870\mu\text{m}$  (Schuller et al. 2009). Complementary single-pointing observations of the CO ( $4-3$ ) line are also included in the analysis in order to characterise the CO emission towards the clumps. Section 2 describes the sample and Sect. 3 presents the observations and data reduction. In Sect. 4 we present the distribution and extent of the mid- $J$  CO lines and their line profiles, compute the CO line luminosities and the excitation temperature of the gas, and compare them with the clump properties. In Sect. 5 we discuss our results in the context of previous works. Finally, the conclusions are summarised in Sect. 6.

## 2. Sample

ATLASGAL detected the vast majority of all current and future high-mass star forming clumps ( $M_{\text{clump}} > 1000M_{\odot}$ ) in the inner Galaxy. Recently, Urquhart et al. (2018) completed the distance assignment for  $\sim 97$  per cent of the ATLASGAL sources and analysed their masses, luminosities and temperatures based on thermal dust emission, and discussed how these properties evolve. Despite the statistical relevance of the ATLASGAL sample, detailed spectroscopic observations are not feasible on the whole sample. Therefore, we defined the ATLASGAL Top 100 (hereafter, TOP100, Giannetti et al. 2014; König et al. 2017), a flux-limited sample of clumps selected from this survey with additional infrared (IR) selection criteria to ensure it encompasses a full range of luminosities and evolutionary stages (from  $70\mu\text{m}$ -weak quiescent clumps to H II regions). The 99 sources analysed in this paper are a sub-sample of the original TOP100 (König et al. 2017) and are classified as follows:

- Clumps which either do not display any point-like emission in the Hi-GAL Survey (Molinari et al. 2010)  $70\mu\text{m}$  images

<sup>1</sup> Based on observations with the APEX telescope under programme IDs M-087.F-0030-2011, M-093.F-0026-2014 and M-096.F-0005-2015. APEX is a collaboration between the Max-Planck-Institut für Radioastronomie, the European Southern Observatory, and the Onsala Space Observatory.

and (or) only show weak, diffuse emission at this wavelength (hereafter, 70w, 14 sources);

- Mid-IR weak sources that are either not associated with any point-like counterparts or the associated compact emission is weaker than  $2.6\text{Jy}$  in the MIPS GAL survey (Carey et al. 2009)  $24\mu\text{m}$  images (hereafter IRw, 31 sources);
- Mid-IR bright sources in an active phase of the high-mass star formation process, with strong compact emission seen in  $8\mu\text{m}$  and  $24\mu\text{m}$  images, but still not associated with radio continuum emission (hereafter IRb, 33 sources);
- Sources in a later phase of the high-mass star formation process that are still deeply embedded in their envelope, but are bright in the mid-IR and associated with radio continuum emission (H II regions, 21 sources).

König et al. (2017) analysed the physical properties of the TOP100 sample in terms of distance, mass and luminosity. They found that at least 85% of the sources have the ability to form high-mass stars and that most of them are likely gravitationally unstable and would collapse without the presence of a significant magnetic field. These authors showed that the TOP100 represents a statistically significant sample of high-mass star-forming clumps covering a range of evolutionary phases, from the coldest and quiescent  $70\mu\text{m}$ -weak to the most evolved clumps hosting H II regions, with no bias in terms of distance, luminosity and mass among the different classes. The masses and bolometric luminosities of the clumps range from  $\sim 20$  to  $5.2 \times 10^5 M_{\odot}$  and from  $\sim 60$  to  $3.6 \times 10^6 L_{\odot}$ , respectively. The distance of the clumps ranges between 0.86 and 12.6 kpc, and 72 of the 99 clumps have distances below 5 kpc. This implies that observations of the TOP100 at the same angular resolution sample quite different linear scales. In Appendix A, Table A.1, we list the main properties of the observed sources. We adopted the Compact Source Catalogue (CSC) names from Contreras et al. (2013) for the TOP100 sample although the centre of the maps may not exactly coincide with those positions (the average offset is  $\sim 5''.4$ , with values ranging between  $\sim 0''.5$ – $25''.8$ , see Table A.1).

In this paper, we investigate the properties of mid- $J$  CO lines for a sub-sample of the original TOP100 as part of our effort to observationally establish a solid evolutionary sequence for high-mass star formation. In addition to the dust continuum analysis of König et al. (2017), we further characterised the TOP100 in terms of the content of the shocked gas in outflows traced by SiO emission (Csengeri et al. 2016) and the ionised gas content (Kim et al. 2017), the CO depletion (Giannetti et al. 2014), and the progressive heating of gas due to feedback of the central objects (Giannetti et al. 2017; Tang et al. 2018). These studies confirm an evolution of the targeted properties with the original selection criteria and strengthen our initial idea that the TOP100 sample constitutes a valuable inventory of high-mass clumps in different evolutionary stages.

## 3. Observations and data reduction

### 3.1. CHAMP<sup>+</sup> observations

Observations of the TOP100 sample were performed with the APEX 12-m telescope on the following dates of 2014 May 17-20, July 10, 15-19, September 9-11 and 20. The CHAMP<sup>+</sup> (Kasemann et al. 2006; Güsten et al. 2008) multi-beam heterodyne receiver was used to map the sources simultaneously in the CO ( $6-5$ ) and CO ( $7-6$ ) transitions. Information about the instrument setup configuration is given in Table 1.

Table 1: Summary of the observations.

Trans.	$E_u$ (K)	Freq. (GHz)	Instr.	$\eta_{\text{mb}}$	Beam size (")	$\Delta V$ ( $\text{km s}^{-1}$ )	$T_{\text{sys}}$ (K)	rms (K)		Observed sources
								median	range	
CO(4–3)	55	461.04	FLASH <sup>+</sup>	0.60	13.4	0.953	1398 ± 761	0.35	0.12–1.50	98
CO(6–5)	116	691.47	CHAMP <sup>+</sup>	0.41	9.6	0.318	1300 ± 250	0.21	0.07–0.75	99
CO(7–6)	155	806.65	CHAMP <sup>+</sup>	0.34	8.2	0.273	5000 ± 1500	0.91	0.29–2.10	99

**Notes.** The columns are as follows: (1) observed transition; (2) upper-level energy of the transition; (3) rest frequency; (4) instrument; (5) main-beam efficiency ( $\eta_{\text{mb}}$ ); (6) beam size at the rest frequency; (7) spectral resolution; (8) mean systemic temperature of the observations; (9)-(10) median and range of the rms of the data of the single-pointing CO(4–3) spectra and the spectra extracted at central position of the CO(6–5) and CO(7–6) maps at their original resolution; (11) number of observed sources per transition (AGAL301.136+00.226 was not observed in CO(4–3)).

The CHAMP<sup>+</sup> array has  $2 \times 7$  pixels that operate simultaneously in the radio frequency tuning ranges 620–720 GHz in the low frequency array (LFA) and the other half in the range 780–950 GHz in the high frequency array (HFA), respectively. The half-power beam widths ( $\theta_{\text{mb}}$ ) are  $9''.0$  (at 691 GHz) and  $7''.7$  (807 GHz), and the beam-spacing is  $\sim 2.15 \theta_{\text{mb}}$  for both sub-arrays. The observations were performed in continuous on-the-fly (OTF) mode and maps of  $80'' \times 80''$  size, centred on the coordinates given in Table A.1, were obtained for each source. The area outside of the central  $60'' \times 60''$  region of each map is covered by only one pixel of the instrument, resulting in a larger rms near the edges of the map. The sky subtraction was performed by observing a blank sky field, offset from the central positions of the sources by  $600''$  in right ascension. The average precipitable water vapour (PWV) of the observations varied from 0.28 to 0.68 mm per day, having a median value of 0.50 mm. The average system temperatures ( $T_{\text{sys}}$ ) ranged from 1050 to 1550 K and 3500 to 6500 K, at 691 and 807 GHz, respectively. Pointing and focus were checked on planets at the beginning of each observing session. The pointing was also checked every hour on Saturn and Mars, and on hot cores (G10.47+0.03 B1, G34.26, G327.3–0.6, and NGC6334I) during the observations.

Each spectrum was rest-frequency corrected and baseline subtracted using the "Continuum and Line Analysis Single Dish Software" (CLASS), which is part of the GILDAS software<sup>2</sup>. The data were binned to a final spectral resolution of  $2.0 \text{ km s}^{-1}$  in order to improve the signal-to-noise ratio of the spectra. The baseline subtraction was performed using a first-order fit to the line-free channels outside a window of  $\pm 100 \text{ km s}^{-1}$  wide, centred on the systemic velocity,  $V_{\text{lsr}}$ , of each source. We used a broader window for sources exhibiting wings broader than  $\sim 80 \text{ km s}^{-1}$  (AGAL034.2572+00.1535, AGAL301.136–00.226, AGAL327.393+00.199, AGAL337.406–00.402, AGAL351.244+00.669 and AGAL351.774–00.537, see Table A.6). Antenna temperatures ( $T_{\text{A}}^*$ ) were converted to main-beam temperatures ( $T_{\text{mb}}$ ) using beam efficiencies of 0.41 at 691 GHz and 0.34 at 809 GHz<sup>3</sup>. Forward efficiencies are 0.95 in all observations. The gridding routine XY\_MAP in CLASS was used to construct the final datacubes. This routine convolves the gridded data with a Gaussian of one third of the beam telescope size, yielding a final angular resolution slightly coarser ( $9''.6$  for CO(6–5) and  $8''.2$  for CO(7–6)) than the original beam size ( $9''.0$  and  $7''.7$ , respectively). The final spectra at the central position of the maps have an average rms noise of 0.20 and 0.87 K for CO(6–5) and CO(7–6) data, respectively.

Figure 1 presents the ratio of the daily integrated flux to the corresponding average flux for the CO(6–5) transition of

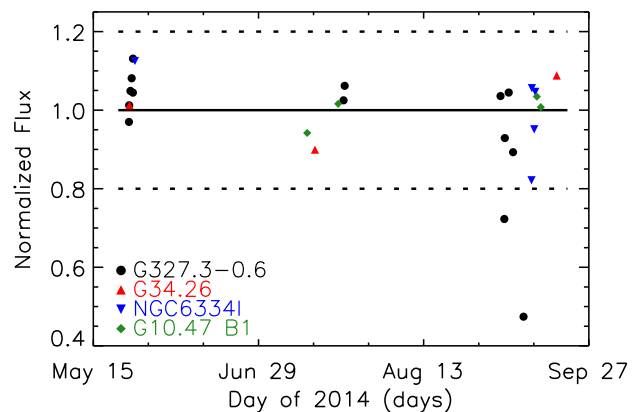


Fig. 1: Ratio of the daily integrated flux to the average flux of the CO(6–5) transition for the calibration sources observed during the campaign. A solid horizontal line is placed at 1.0 and the dashed lines indicate a deviation of 20% from unity.

each hot core used as calibrator as a function of the observing day. The deviation of the majority of the points with respect to their average value is consistent within a  $\pm 20\%$  limit; thus, this value was adopted as the uncertainty on the integrated flux for both mid- $J$  CO transitions. On September 10, the observations of G327.3–0.6 showed the largest deviation from the average flux of the source (points at  $y \sim 0.7$  and  $y \sim 0.5$  in Fig. 1). For this reason, we associate an uncertainty of 30% on the integrated flux of the sources AGAL320.881–00.397, AGAL326.661+00.519 and AGAL327.119+00.509, and of 50% for sources AGAL329.066–00.307 and AGAL342.484+00.182, observed immediately after these two scans on G327.3–0.6.

### 3.2. FLASH<sup>+</sup> observations

The FLASH<sup>+</sup> (Klein et al. 2014) heterodyne receiver on the APEX telescope was used to observe the central positions of the CHAMP<sup>+</sup> maps in CO(4–3) on 2011 June 15 and 24, August 11 and 12. Table 1 summarises the observational setup. The observations were performed in position switching mode with an offset position of  $600''$  in right ascension for sky-subtraction. Pointing and focus were checked on planets at the beginning of each observing session. The pointing was also regularly checked during the observations on Saturn and on hot cores (G10.62, G34.26, G327.3–0.6, NGC6334I and SGRB2(N)). The average PWV varied from 1.10 to 1.55 mm per day with a median value of 1.29 mm. The system temperatures of the observations ranged from 650 to 2150 K.

<sup>2</sup> <http://www.iram.fr/IRAMFR/GILDAS>

<sup>3</sup> [www3.mpi-fr-bonn.mpg.de/div/submmtech/heterodyne/champplus/champ\\_efficiencies.16-09-14.html](http://www3.mpi-fr-bonn.mpg.de/div/submmtech/heterodyne/champplus/champ_efficiencies.16-09-14.html)

The single-pointing observations were processed using GILDAS/CLASS software. The data were binned to a final spectral resolution of  $2.0 \text{ km s}^{-1}$  and a fitted line was subtracted to establish a straight baseline. The antenna temperatures were converted to  $T_{\text{mb}}$  by assuming beam and forward efficiencies of 0.60 and 0.95, respectively. The resulting CO (4–3) spectra have an average rms noise of 0.36 K. The uncertainty on the integrated flux of FLASH<sup>+</sup> data was estimated to be  $\sim 20\%$  based on the continuum flux of the sources observed during the pointing scans.

### 3.3. Spatial convolution of the mid-*J* CO data

The CO (6–5) and CO (7–6) data were convolved to a common angular resolution of  $13''.4$ , matching the beam size of the single-pointing CO (4–3) observations. The resulting spectra are shown in Appendix B.

The median rms of the convolved spectra are 0.35 K, 0.17 K and 0.87 K for the CO (4–3), CO (6–5) and CO (7–6) transitions, respectively. These values differ from those reported in Table 1 for the CHAMP<sup>+</sup> data where the rms at the original resolution of the dataset is given. Since our sources are not homogeneously distributed in distance (see Sect. 2), spectra convolved to the same angular resolution of  $13''.4$  sample linear scales between 0.06 and 0.84 pc. In order to study the effect of any bias introduced by sampling different linear scales within the clumps, the CO (6–5) and CO (7–6) data were also convolved to the same linear scale,  $\ell_{\text{lin}}$ , of  $\sim 0.24$  pc, which corresponds to an angular size  $\theta$  (in radians) of:

$$\theta = \tan^{-1} \left( \frac{\ell_{\text{lin}}}{d} \right) \quad (1)$$

that depends on the distance of the source. The choice of  $\ell_{\text{lin}}$  is driven by the nearest source, AGAL353.066+00.452, for which the part of the map with a relatively uniform rms (see Sect. 3.1) corresponds to a linear scale of  $\sim 0.24$  pc. Since we are limited by the beam size of the CO (6–5) observations ( $\sim 10''$ ), the same projected length can be obtained only for sources located at distances up to  $\sim 5.0$  kpc. This limit defines a sub-sample of 72 clumps (ten 70w, 20 IRw, 26 IRb and 16 H II regions).

The rest of the paper focuses on the properties of the full TOP100 sample based on the spectra convolved to  $13''.4$ . The properties of the distance-limited sub-sample differ from those of the  $13''.4$  data only for the line profile (see Sect. 4.2). A detailed comparison between the CO line luminosity and the properties of the clumps for the distance-limited sample is presented in Appendix C.1.

### 3.4. Self-absorption and multiple velocity components

The CO spectra of several clumps show a double-peak profile close to the ambient velocity (e.g. AGAL12.804–00.199, AGAL14.632–00.577, and AGAL333.134–00.431, see Fig. B.1). These complex profiles could arise from different velocity components in the beam or could be due to self-absorption given the likely high opacity of CO transitions close to the systemic velocity. To distinguish between these two scenarios, the  $13''.4$  CO spectra obtained in Sect. 3.3 were compared to the C<sup>17</sup>O (3–2) data from Giannetti et al. (2014) observed with a similar angular resolution ( $19''$ ). In the absence of C<sup>17</sup>O observations (AGAL305.192–00.006, AGAL305.209+00.206 and AGAL353.066+00.452), the C<sup>18</sup>O (2–1) profiles were used. Since the isotopologue line emission is usually optically thin (cf.

Giannetti et al. 2014), it provides an accurate determination of the systemic velocity of the sources and, therefore, can be used to distinguish between the presence of multiple components or self-absorption in the optically thick <sup>12</sup>CO lines. Thus, when C<sup>17</sup>O or C<sup>18</sup>O show a single peak corresponding in velocity to a dip in CO, we consider the CO spectra to be affected by self-absorption. Otherwise, if also the isotopologue data show a double-peak profile, the emission is likely due to two different velocity components within the beam. From the comparison with the CO isotopologues, we found 83 clumps with self-absorption features in the CO (4–3) line, 79 in the CO (6–5), 70 in the CO (7–6) transition. These numbers indicate that higher-*J* CO transitions tend to be less affected by self-absorption features when compared to the lower-*J* CO lines. Finally, only 15 objects do not display self-absorption features in any transitions. The CO spectra affected by self-absorption features are flagged with an asterisk symbol in Table A.6.

To assess the impact of self-absorption on the analysis presented in Sect. 4.3, in particular on the properties derived from the integrated flux of the CO lines, we compared the observed integrated intensity of each CO transition with the corresponding values obtained from the Gaussian fit presented in Sect. 3.5. This comparison indicated that self-absorption changes the offsets and the scatter of the data but not the slopes of the relations between the CO emission and the clump properties. Then, we investigated the ratio between the observed and the Gaussian integrated intensity values as a function of the evolutionary classes of the TOP100 sample. We found that 95% of the sources exhibit ratios between 0.7 and 1.0 for all three lines. We also note a marginal decrease on the ratios from the earliest 70w class ( $\sim 1.0$ ) to H II regions ( $\sim 0.8$ ), indicating that self-absorption does not significantly affect the results presented in the following sections. We further investigated the effects of self-absorption by studying the sub-sample of  $\sim 15$  sources not affected by self-absorption (that is, the sources that are not flagged with an asterisk symbol in Table A.6) and verified that the results presented in the following sections for the full sample are consistent with those of this sub-sample, although spanning a much broader range of clump masses and luminosities. More details on the analysis of the robustness of the relations reported in Sect. 4.3 are provided in Appendices C.1 and C.2. Five sources (see Appendix C.3) show a second spectral feature in the <sup>12</sup>CO transitions and in the isotopologue data of Giannetti et al. (2014) shifted in velocity from the rest velocity of the source. We compared the spatial distribution of the integrated intensity CO (6–5) emission with the corresponding ATLASGAL 870  $\mu\text{m}$  images (see Fig. C.5) for these five clumps. We found that in all sources the morphology of the integrated emission of one of the two peaks (labelled as P2 in Tables A.2 to A.4) has a different spatial distribution than the dust emission at 870  $\mu\text{m}$  and, thus, is likely not associated with the TOP100 clumps. These components are excluded from any further analysis in this paper.

### 3.5. Gaussian decomposition of the CO profiles

The convolved CO spectra were fitted using multiple Gaussian components. The fits were performed interactively using the MINIMIZE task in CLASS/GILDAS. A maximum number of three Gaussian components per spectrum was adopted. Each spectrum was initially fitted with one Gaussian component: if the residuals had sub-structures larger than  $3\text{-}\sigma$ , a second or even a third component was added. In case of self-absorption (see Sect. 3.4), the affected channels were masked before performing the fit. Any residual as narrow as the final velocity resolution of the data

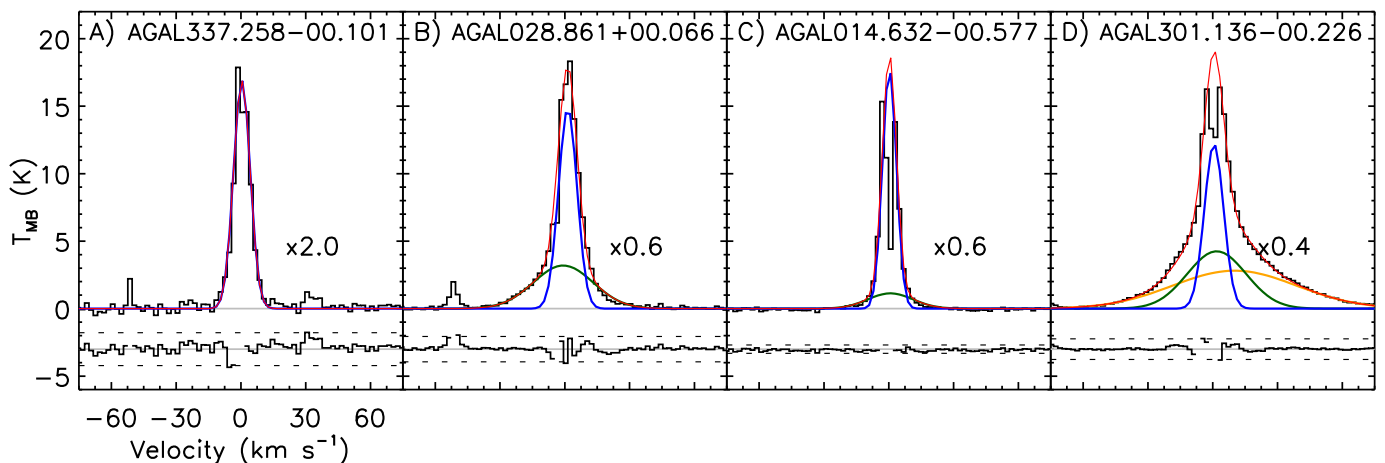


Fig. 2: Gaussian decomposition for the CO (6–5) line using up to 3 components. Panel A: single Gaussian fit; Panel B: two-components fit; Panel C: two-components fit (channels affected by self absorption are masked); Panel D: three-components fit (channels affected by self absorption are masked). The spectra, fits and residuals were multiplied by the factor shown in each panel. The Gaussian fits are shown in blue, green and yellow, ordered by their line width; the sum of all components is shown in red. The grey lines indicate the baseline and the dashed horizontal lines placed in the residuals correspond to the  $3\text{-}\sigma$  level. Self-absorption features larger than  $5\text{-}\sigma$  were masked out from the residuals.

Table 2: Results of the Gaussian fit of the CO spectra convolved to a common angular resolution of  $13''.4$ .

Transition	One comp.	Two Comp.	Three comp.
CO (4–3)	27 (7,8,3,4)	68 (4,13,21,4)	3 (0,0,1,1)
CO (6–5)	12 (6,4,1,1)	58 (8,18,20,7)	29 (0,7,12,7)
CO (7–6)	35 (14,14,6,1)	53 (0,16,24,10)	10 (0,1,3,6)

**Notes.** The columns are as follows: (1) CO transition, (2)–(4) number of sources fitted using (2) a single Gaussian component, (3) two and (4) three components. In each column, the values in parenthesis indicate the corresponding number of 70w, IRw, IRb and H II regions.

( $2.0\text{ km s}^{-1}$ ) was ignored. In particular for CO (4–3), absorption features shifted in velocity from the main line are detected in several sources. These features are likely due to emission in the reference position, and were also masked before fitting the data. Examples of the line profile decomposition are given in Fig. 2.

Each component was classified as narrow (N) or broad (B), adopting the scheme from San José-García et al. (2013). According to their definition, the narrow component has a full-width at half maximum (FWHM) narrower than  $7.5\text{ km s}^{-1}$ , otherwise it is classified as a broad component. Results of the Gaussian fit are presented in Tables A.2–A.4. In several cases, two broad components are needed to fit the spectrum. For the CO (6–5) data, 29 of the profiles required 3 components and, thus, two or three components have received the same classification. In these cases, they were named as, for example, B1, B2; ordered by their width. The P2 features mark secondary velocity components not associated with TOP100 clumps (see Sect. 3.4).

As a consequence of high opacity and self-absorption, the Gaussian decomposition of the line profile can be somewhat dubious. In some cases, and in particular for the CO (4–3) transition, the fit is unreliable (e.g. AGAL305.192–00.006 and AGAL333.134–00.431 in Fig. B.1). The sources associated with unreliable Gaussian decomposed CO profiles (32, 8 and 4 for CO (4–3), CO (6–5) and CO (7–6), respectively) are not shown in Tables A.2 to A.4 and their data are not included in the analysis presented in Sect. 4, as well as in that of the integrated prop-

Table 3: Statistics of the FWHM of the Gaussian components fitted on the CO line profiles convolved to a common angular resolution of  $13''.4$ .

Transition	Class.	$N$	FWHM ( $\text{km s}^{-1}$ )			
			Range	Mean	Median	$\sigma$
CO (4–3)	Narrow	28	3.23–7.47	6.27	6.57	1.14
	Broad	83	7.5–86.0	21.2	14.9	16.5
CO (6–5)	Narrow	48	2.55–7.48	5.69	6.91	1.36
	Broad	148	7.5–97.1	24.5	17.8	19.0
CO (7–6)	Narrow	32	2.00–7.38	5.90	6.32	1.25
	Broad	133	7.5–120.2	27.8	16.4	26.6

**Notes.** The table presents the statistics on the FWHM of the narrow and broad Gaussian velocity component, classified according to Sect. 3.5. The columns are as follows: (1) referred CO transition; (2) classification of the Gaussian component; (3) number of fitted components per class ( $N$ ); (4) the minimum and maximum value per class; (5) the mean, (6) the median, and (7) the standard deviation of the distribution.

erties of their line profiles (e.g. their integrated intensities and corresponding line luminosities, see Sect. 4.3).

The general overview of the fits are given in Table 2 and the statistics of FWHM of the narrow and broad Gaussian components are listed in Table 3. The spectrum of each source with its corresponding decomposition into Gaussian components is presented in Fig. B.1.

#### 4. Observational results

The whole sample is detected above a  $3\text{-}\sigma$  threshold in the single-pointing CO (4–3) data (source AGAL301.136–00.226 was not observed with FLASH<sup>+</sup>) and in the  $13''.4$  CO (6–5) and CO (7–6) spectra, with three 70w sources (AGAL030.893+00.139, AGAL351.571+00.762 and AGAL353.417–00.079) only marginally detected above the  $3\text{-}\sigma$  limit in CO (7–6).

In the rest of this section we characterise the CO emission towards the TOP100 sample through the maps of CO (6–5)

(Sect. 4.1) and the analysis of the CO line profiles for the spectra convolved to  $13''4$  (Sect. 4.2). In Sect. 4.3, we compute the CO line luminosities and compare them with the clump properties. Finally, in Sect. 4.4 we compute the excitation temperature of the gas.

#### 4.1. Extent of the CO emission

In Fig. 3 we present examples of the integrated intensity maps of the CO (6–5) emission as a function of the evolutionary class of the TOP100 clumps. The CO (6–5) maps of the full TOP100 sample are presented in Appendix B (see Fig. B.1).

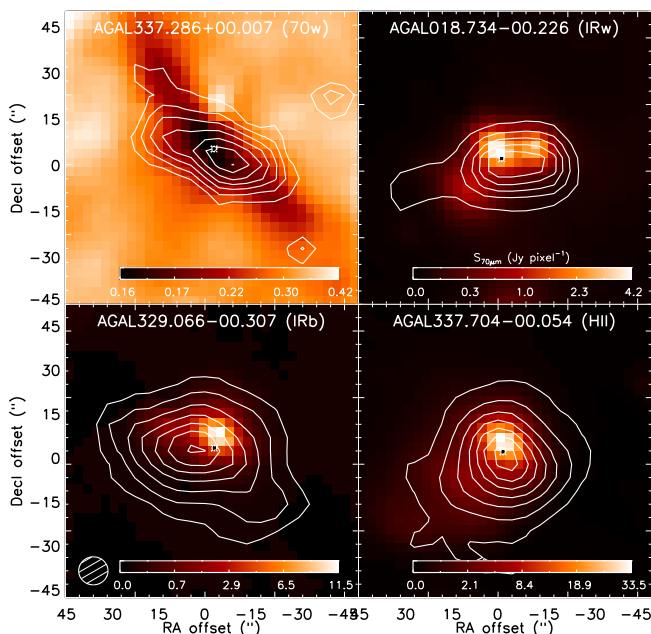


Fig. 3: Distribution of the CO (6–5) emission of four representative clumps of each evolutionary classes of the TOP100 clumps. The CO contours are presented on top of the *Herschel*/PACS maps at  $70\mu\text{m}$ . Each  $70\mu\text{m}$  map is scaled in according to the colour bar shown in the corresponding panel. The CO contours correspond to the emission integrated over the full-width at zero power (FWZP) of the CO (6–5) line, and the contour levels are shown from 20% to 90% of the peak emission of each map, in steps of 10%. The position of the CSC source from Contreras et al. (2013) is shown as a  $\times$  symbol. The beam size of the CO (6–5) observations is indicated in the left bottom region.

We estimated the linear size of the CO emission,  $\Delta s$ , defined as the average between the maximum and minimum elongation of the half-power peak intensity (50%) contour level of the CO (6–5) integrated intensity (see Table A.5). The uncertainty on  $\Delta s$  was estimated as the dispersion between the major and minor axis of the CO extent. The linear sizes of the CO emission ranges between 0.1 and 2.4 pc, with a median value of 0.5 pc. In order to investigate if  $\Delta s$  varies with evolution, we performed a non-parametric two-sided Kolmogorov-Smirnov (KS) test between pairs of classes (i.e. 70w vs. IRb; IRw vs. HII). The sub-samples were considered statistically different if their KS rank factor is close to 1 and associated with a low probability value,  $p$ , ( $p \leq 0.05$  for a significance  $\geq 2\sigma$ ). Our analysis indicates that there is no significant change in the extension of CO with evolution (KS  $\leq 0.37$ ,  $p \geq 0.05$  for all comparisons). The CO extent was further compared with the bolometric luminosity,

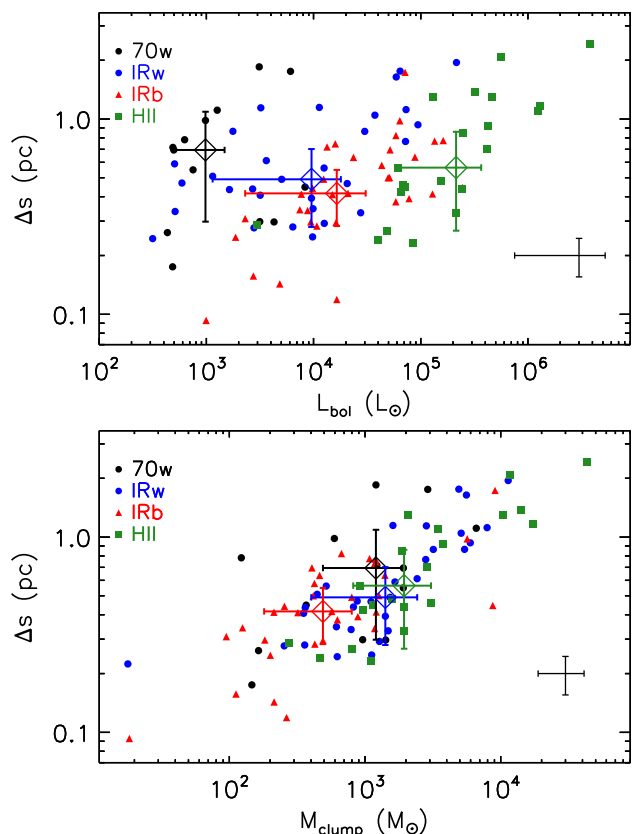


Fig. 4: Size of the CO (6–5) emission towards the TOP100 sample versus the bolometric luminosity (top) and the mass (bottom) of the sources. The median values for each class are shown as open diamonds and their error bars correspond to the absolute deviation of the data from their median value. The typical uncertainty is shown by the error bars on the bottom right of each plot.

$L_{\text{bol}}$ , and the mass of the clumps,  $M_{\text{clump}}$ , reported by König et al. (2017). The results are presented in Fig. 4.  $\Delta s$  shows a large scatter as a function of  $L_{\text{bol}}$  while it increases with  $M_{\text{clump}}$  ( $\rho = 0.72$ ,  $p < 0.001$  for the correlation with  $M_{\text{clump}}$   $\rho = 0.42$ ,  $p < 0.001$  for  $L_{\text{bol}}$ , where the  $\rho$  is the Spearman rank correlation factor and  $p$  its associated probability). This confirms that the extent of the CO emission is likely dependent of the amount of gas within the clumps, but not on their bolometric luminosity.

We derived the extent of the  $70\mu\text{m}$  emission ( $\Delta s_{70\mu\text{m}}$ ) towards the  $70\mu\text{m}$ -bright clumps by cross-matching the position of the TOP100 clumps with the sources from Molinari et al. (2016). Then,  $\Delta s_{70\mu\text{m}}$  was obtained by computing the average between the maximum and minimum FWHM reported on their work and the corresponding error was obtained as the standard deviation of the FWHM values. The values are also reported in Table A.5. Figure 5 compares the extent of the CO (6–5) emission with that of the  $70\mu\text{m}$  emission towards the  $70\mu\text{m}$  bright clumps. The extent of the emission of CO (6–5) and of the  $70\mu\text{m}$  continuum emission are correlated (Fig. 5,  $\rho = 0.67$ ,  $p < 0.001$ ), and in the majority of cases, the points are located above the equality line, suggesting that the gas probed by the CO (6–5) transition tends to be more extended than the dust emission probed by the PACS data towards the  $70\mu\text{m}$ -bright clumps.

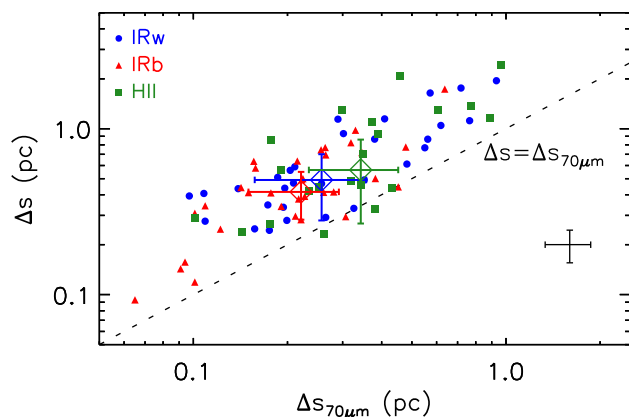


Fig. 5: Size of the CO (6–5) emission versus the size of the  $70\mu\text{m}$  emission from the *Herschel*-PACS images towards the  $70\mu\text{m}$ -bright clumps. The dashed line indicates  $y = x$ . The median values for the  $70\mu\text{m}$ -bright classes are shown as open diamonds and their error bars correspond to the absolute deviation of the data from their median value. The typical uncertainty, computed as the dispersion between the major and minor axis of the emission, is shown by the error bars on the bottom right of each plot.

#### 4.2. Line profiles

In the majority of the cases, the CO profiles are well fit with two Gaussian components, one for the envelope, one for high-velocity emission (see Table 2). A third component is required in some cases, in particular for the CO (6–5) data, which have the highest signal-to-noise ratio. The majority of sources fitted with a single Gaussian component are in the earliest stages of evolution (70w and IRw clumps), suggesting that the CO emission is less complex in earlier stages of high-mass star formation. We also detect non-Gaussian high-velocity wings likely associated with outflows in most of the CO (6–5) profiles. A detailed discussion of the outflow content in the TOP100 sample and of their properties will be presented in a forthcoming paper (Navarete et al., in prep.).

To minimise biases due to different sensitivities in the analysis of single spectra, we computed the average CO spectrum of each evolutionary class and normalised it by its peak intensity. The spectra were shifted to  $0\text{ km s}^{-1}$  using the correspondent  $V_{\text{lsr}}$  given in Table A.1. Then, the averaging was performed by scaling the intensity of each spectrum to the median distance of the sub-sample ( $d = 3.26\text{ kpc}$  for the distance-limited sample,  $d = 3.80\text{ kpc}$  for the full sample). The resulting spectra of the  $13''4$  dataset are shown in Fig. 6 while those of the distance-limited sub-sample are presented in Appendix C.1 (Fig. C.1). While the  $13''4$  data show no significant difference between the average profiles of IRw and IRb classes, in the distance-limited sub-sample the width (expressed through the full width at zero power, FWZP, to avoid any assumption on the profile) and the intensity of the CO lines progressively increase with the evolution of the sources (from 70w clumps towards H II regions) especially when the normalised profiles are considered. The difference between the two datasets is due to sources at large distances ( $d > 12\text{ kpc}$ ; AGAL018.606–00.074, AGAL018.734–00.226 and AGAL342.484+00.182) for which the observations sample a much larger volume of gas. The increase of line width with evolution is confirmed by the analysis of the individual FWZP values of the three CO lines, presented in Table A.6 (see Table 4 for the statistics on the full TOP100 sample).

Table 4: Statistics on the CO line profiles, convolved to a common angular resolution of  $13''4$ .

Transition	FWZP ( $\text{km s}^{-1}$ )			
	Range	Mean	Median	Standard deviation
CO (4–3)	10–134	47	42	25
CO (6–5)	14–162	62	54	34
CO (7–6)	4–142	39	30	27

**Notes.** The table presents the FWZP of the CO lines. The mid- $J$  CO lines were convolved to a common angular resolution of  $13''4$ . The columns are as follows: (1) referred CO line; (2) the minimum and maximum values, (3) the mean, (4) the median, and (5) the standard deviation of the distribution.

Despite the possible biases in the analysis of the line profiles (e.g. different sensitivities, different excitation conditions, complexity of the profiles), our data indicate that the CO emission is brighter in late evolutionary phases. The average spectra per class show also that the CO lines becomes broader towards more evolved phases likely due to the presence of outflows. Our study extends the work of Leurini et al. (2013) on one source of our sample, AGAL327.293–00.579. They mapped in CO (3–2), CO (6–5), CO (7–6) and in  $^{13}\text{CO}$  (6–5),  $^{13}\text{CO}$  (8–7) and  $^{13}\text{CO}$  (10–9) a larger area of the source than that presented here and found that, for all transitions, the spectra are dominated in intensity by the H II region rather than by younger sources (a hot core and an infrared dark cloud are also present in the area). They interpreted this result as an evidence that the bulk of the Galactic CO line emission comes from PDRs around massive stars, as suggested by Cubick et al. (2008) for FIR line emission. Based on this, we suggest that the increase in mid- $J$  CO brightness in the later stages of the TOP100 is due to a major contribution of PDR to the line emission. We notice however that the increase of width and of intensity of the CO lines with evolution can also be due to an increase with time of multiplicity of sources in the beam.

#### 4.3. The CO line luminosities

The intensity of the CO profiles ( $S_{\text{int}}$ , in  $\text{K km s}^{-1}$ ) was computed by integrating the CO emission over the velocity channels within the corresponding FWZP range. Then, the line luminosity ( $L_{\text{CO}}$ , in  $\text{K km s}^{-1} \text{ pc}^2$ ) of each CO line was calculated using Eq. 2 from Wu et al. (2005), assuming a source of size equal to the beam size of the data (see Sect. 3.3). The derived  $L_{\text{CO}}$  values are reported in Table A.6. The errors in the  $L_{\text{CO}}$  values are estimated by error propagation on the integrated flux (see Sect. 3.1) and considering an uncertainty of 20% in the distance. The median values of  $L_{\text{CO}}$ ,  $L_{\text{bol}}$ ,  $M_{\text{clump}}$  and  $L/M$ , the luminosity-to-mass ratio, per evolutionary class are summarised in Table 5. We also performed the same analysis on the data convolved to a common linear scale of  $0.24\text{ pc}$  (assuming the corresponding angular source size of  $0.24\text{ pc}$  to derive the line luminosity) and no significant differences in the slope of the trends were found. Therefore, the distance-limited sample will not be discussed any further in this section.

In Fig. 7 we show the cumulative distribution function (CDF) of the line luminosities for the three CO transitions:  $L_{\text{CO}}$  increases from 70w sources towards H II regions. Each evolutionary class was tested against the others by computing their two-sided KS coefficient (see Table 6). The most significant differences are found when comparing the earlier and later evolu-

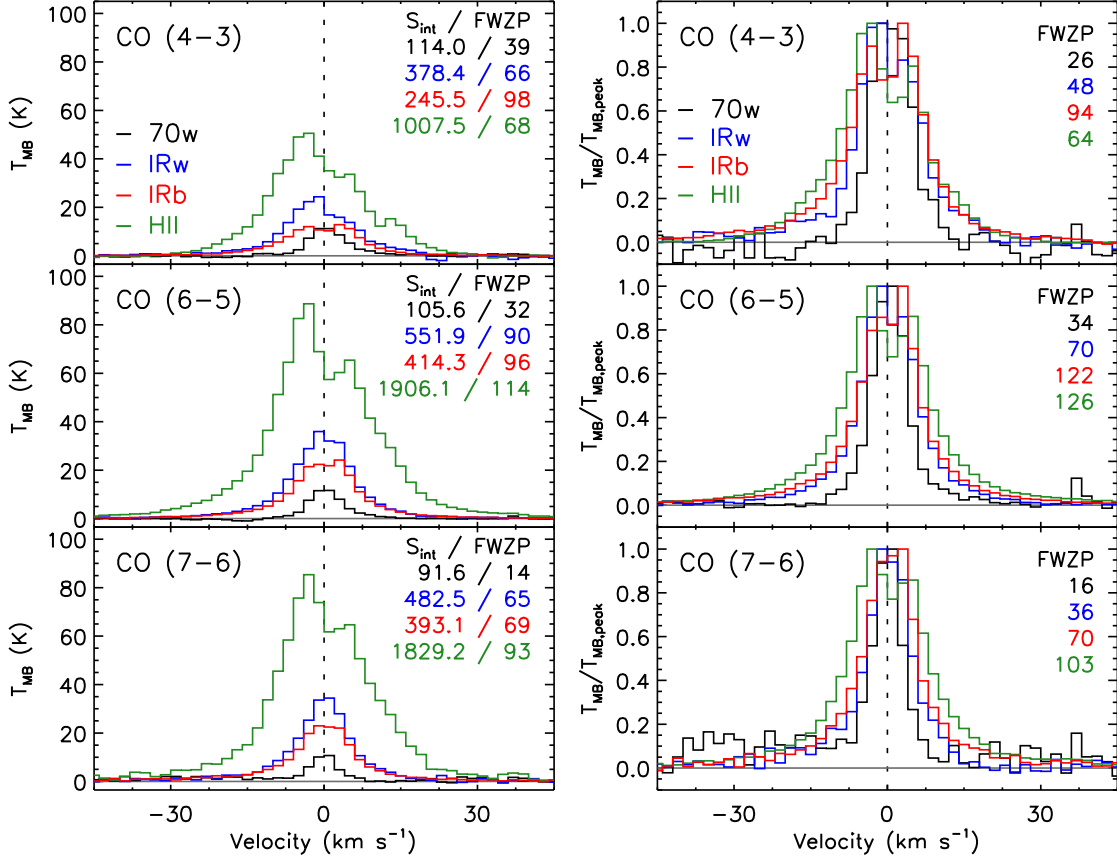


Fig. 6: Left: Average CO (4–3), CO (6–5) and CO (7–6) spectra convolved to 13.4'' beam of each evolutionary class scaled to the median distance of the whole sample ( $d = 3.80$  kpc). Right: Same plot, but the average CO spectra are normalised by their peak intensity. The baseline level is indicated by the solid grey line and the black dashed line is placed at 0 km s<sup>-1</sup>. The FWZP of the profiles are shown in the upper right side of the panels (in km s<sup>-1</sup> units), together with the integrated intensities ( $S_{\text{int}}$ , in K km s<sup>-1</sup> units) of the CO profiles shown in the left panels.

Table 5: Median values per class of the clump and CO profile properties.

Property	70w	IRw	IRb	H II
$L_{\text{bol}}$ ( $10^3 L_{\odot}$ )	1.26±0.83	9.6±8.4	16.5±1.4	21.4±1.5
$M_{\text{clump}}$ ( $10^3 M_{\odot}$ )	1.22±0.70	1.4±1.1	0.49±0.31	1.9±1.1
$L/M$ ( $L_{\odot}/M_{\odot}$ )	2.58±0.93	9.0±6.8	40±23	76±28
$L_{\text{CO}(4-3)}$ (K km s <sup>-1</sup> pc <sup>2</sup> )	9.8±8.5	30±23	21±15	119±58
$L_{\text{CO}(6-5)}$	5.1±4.0	16±12	19±12	51±44
$L_{\text{CO}(7-6)}$	4.7±3.6	11.8±8.6	14.8±9.7	48±45
FWZP <sub>CO(4-3)</sub> (km s <sup>-1</sup> )	24.0±6.0	34±12	52±16	62±18
FWZP <sub>CO(6-5)</sub>	26.0±6.0	42±14	72±22	102±28
FWZP <sub>CO(7-6)</sub>	12.0±2.0	24.0±6.0	38±14	66±20
$T_{\text{ex}}$ (K)	22.4±5.0	29.9±8.1	45±15	95±21

**Notes.** The median and the absolute deviation of the data from their median value are shown for the clump properties (bolometric luminosity, mass and luminosity-to-mass ratio), for the line luminosity and full width at zero power of the low- $J$  and mid- $J$  CO profiles convolved to the same angular size of 13.4'', and for the excitation temperature of the CO (6–5) emission.

tionary classes (70w and IRb, 70w and H II,  $\rho \geq 0.66$  for the CO (6–5) line), while no strong differences are found among the other classes ( $KS \leq 0.5$  and  $p \geq 0.003$  for the CO (6–5) transition). These results indicate that, although we observe an increase on the CO line luminosity from 70w clumps towards H II regions, no clear separation is found in the intermediate classes (IRw and IRb, see also Table 5).

We also plot  $L_{\text{CO}}$  against the bolometric luminosity of the clumps (Fig. 7), their mass and their luminosity-to-mass ratio

(Figs. 8 and 9 for the CO (6–5) line). The  $L/M$  ratio is believed to be a rough estimator of evolution in the star formation process for both low- (Saraceno et al. 1996) and high-mass regimes (e.g. Molinari et al. 2008), with small  $L/M$  values corresponding to embedded regions where (proto-)stellar activity is just starting, and high  $L/M$  values in sources with stronger radiative flux and that have accreted most of the mass (Molinari et al. 2016; Giannetti et al. 2017; Urquhart et al. 2018). In addition, the  $L/M$  ratio also reflects the properties of the most mas-



Table 6: Kolmogorov-Smirnov statistics of the CO line luminosity as a function of the evolutionary class of the clumps.

Classes	CO (4–3)	CO (6–5)	CO (7–6)
70w-IRw	0.48, $p = 0.05$	0.45, $p = 0.03$	0.46, $p = 0.02$
70w-IRb	0.35, $p = 0.25$	0.66, $p < 0.001$	0.66, $p < 0.001$
70w-H II	0.72, $p = 0.004$	0.80, $p < 0.001$	0.82, $p < 0.001$
IRw-IRb	0.29, $p = 0.23$	0.21, $p = 0.46$	0.24, $p = 0.26$
IRw-H II	0.41, $p = 0.15$	0.46, $p = 0.02$	0.47, $p = 0.01$
IRb-H II	0.62, $p = 0.004$	0.53, $p = 0.003$	0.52, $p = 0.003$

**Notes.** The rank KS and its corresponding probability ( $p$ ) are shown for each comparison. A  $p$ -value of  $< 0.001$  indicate a correlation at 0.001 significance level.  $p$ -values of 0.05, 0.002 and  $< 0.001$  represent the  $\sim 2$ , 3 and  $> 3 \sigma$  confidence levels.

Table 7: Parameters of the fits of  $L_{\text{CO}}$  as a function of the clump properties.

Transition	Property	$\alpha$	$\beta$	$\epsilon$
CO (4–3)	$L_{\text{bol}}$	$-0.86^{+0.24}_{-0.23}$	$0.55 \pm 0.05$	0.41
	$M_{\text{clump}}$	$-1.37^{+0.23}_{-0.19}$	$0.92 \pm 0.06$	0.34
	$L/M$	$+1.08^{+0.12}_{-0.14}$	$0.28 \pm 0.12$	0.63
CO (6–5)	$L_{\text{bol}}$	$-1.33^{+0.14}_{-0.13}$	$0.63 \pm 0.03$	0.25
	$M_{\text{clump}}$	$-1.58^{+0.23}_{-0.22}$	$0.92 \pm 0.07$	0.37
	$L/M$	$+0.74^{+0.09}_{-0.08}$	$0.46 \pm 0.09$	0.55
CO (7–6)	$L_{\text{bol}}$	$-1.64^{+0.12}_{-0.11}$	$0.68 \pm 0.03$	0.22
	$M_{\text{clump}}$	$-1.64^{+0.22}_{-0.24}$	$0.92 \pm 0.08$	0.43
	$L/M$	$+0.55^{+0.10}_{-0.08}$	$0.55 \pm 0.10$	0.54

**Notes.** The fits were performed by adjusting a model with three free parameters in the form of  $\log(y) = \alpha + \beta \log(x) \pm \epsilon$ , where  $\alpha$ ,  $\beta$  and  $\epsilon$  correspond to the intercept, the slope and the intrinsic scatter, respectively.

sive young stellar object embedded in the clump (Faúndez et al. 2004; Urquhart et al. 2013a). The fits were performed using a Bayesian approach, by adjusting a model with three free parameters (the intercept,  $\alpha$ , the slope,  $\beta$ , and the intrinsic scatter,  $\epsilon$ ). In order to obtain a statistically reliable solution, we computed a total of 100 000 iterations per fit. The parameters of the fits are summarised in Table 7. The correlation between  $L_{\text{CO}}$  and the clump properties was checked by computing their Spearman rank correlation factor and its associated probability ( $\rho$  and  $p$ , respectively, see Table 8). Since  $L_{\text{CO}}$  with  $L_{\text{bol}}$  and  $M_{\text{clump}}$  have the same dependence on the distance of the source, a partial Spearman correlation test was computed and the partial coefficient,  $\rho_p$ , was obtained (see Table 8).

In the right panel of Fig. 7, we show the CO line luminosity versus the bolometric luminosity of the TOP100 clumps. The plot indicates that  $L_{\text{CO}}$  increases with  $L_{\text{bol}}$  over the entire  $L_{\text{bol}}$  range covered by the TOP100 clumps ( $\sim 10^2$ - $10^6 L_{\odot}$ ). The Spearman rank test confirms that both quantities are well correlated for all CO lines ( $\rho \geq 0.7$ , with  $p < 0.001$ ), even when excluding the mutual dependence on distance ( $\rho_p \geq 0.81$ ). The results of the fits indicate a systematic increase in the slope of  $L_{\text{CO}}$  versus  $L_{\text{bol}}$  for higher- $J$  transitions:  $0.55 \pm 0.05$ ,  $0.63 \pm 0.03$  and  $0.68 \pm 0.03$  for the CO (4–3), CO (6–5) and CO (7–6), respectively. For the CO (6–5) and CO (7–6) lines, however, the slopes are consistent in within  $2\text{-}\sigma$ . Concerning the dependence of the CO luminosity on  $M_{\text{clump}}$  (see Fig. 8), the partial correlation tests indicates that the distance of the clumps plays a more substantial role in the correlation found between  $L_{\text{CO}}$  and  $M_{\text{clump}}$  ( $0.48 \leq \rho_p \leq 0.57$ )

Table 8: Spearman rank correlation statistics for the CO line luminosity as a function of the clump properties towards the TOP100 sample.

Property	CO (4–3)	CO (6–5)	CO (7–6)
$L_{\text{bol}}$	0.70, $p < 0.001$ ; $\rho_p = 0.81$	0.85, $p < 0.001$ ; $\rho_p = 0.91$	0.89, $p < 0.001$ ; $\rho_p = 0.92$
$M_{\text{clump}}$	0.75, $p < 0.001$ ; $\rho_p = 0.48$	0.70, $p < 0.001$ ; $\rho_p = 0.55$	0.67, $p < 0.001$ ; $\rho_p = 0.57$
$L/M$	0.24, $p = 0.05$	0.45, $p < 0.001$	0.50, $p < 0.001$

**Notes.** The rank  $\rho$  and its corresponding probability ( $p$ ) are shown for each comparison. A  $p$ -value of  $< 0.001$  indicate a correlation at 0.001 significance level.  $p$ -values of 0.05, 0.002 and  $< 0.001$  represent the  $\sim 2$ , 3 and  $> 3 \sigma$  confidence levels. For  $L_{\text{bol}}$  and  $M_{\text{clump}}$ , the partial correlation coefficient,  $\rho_p$ , is also shown.

than in the correlations found for  $L_{\text{CO}}$  vs.  $L_{\text{bol}}$ . Finally, we do not find any strong correlation between the CO line luminosity and  $L/M$  ( $\rho \leq 0.5$  for all transitions) although the median  $L_{\text{CO}}$  values per class do increase with  $L/M$  (Fig. 9). These findings are discussed in more detail in Sect. 5.

We further tested whether the steepness of the relations between  $L_{\text{CO}}$  and the clump properties is not affected by self-absorption by selecting only those clumps which do not show clear signs of self-absorption (see Sect. 3.5). This defines a sub-sample of 15 sources in the CO (4–3) line, 18 in the CO (6–5) line and 26 objects in the CO (7–6) transition. These sources are highlighted in Figs. 7, 8 and 9. Then, we repeated the fit of the relations between  $L_{\text{CO}}$  and the clump properties using these sub-samples, finding no significant differences in the slopes of the relations presented in Table 7. The result of the fits for the sub-sample of sources with no signs of self-absorption in their 13''4 spectra are summarised in Table 9 and the correlations between  $L_{\text{CO}}$  and the clump properties are listed in Table 10. The correlations are systematically weaker due to the smaller number of points than those obtained for the whole TOP100 sample (see Table 8). We found that the derived slopes for the relations between  $L_{\text{CO}}$  and  $L_{\text{bol}}$  increases from  $0.58 \pm 0.09$  to  $0.71 \pm 0.07$ , from the CO (4–3) to the CO (7–6) transition. Despite the larger errors in these relations, the slopes of the fits performed on these sources are not significantly different from those found for the whole TOP100 sample, confirming that at least the slopes of the relations found for the whole TOP100 sample are robust in terms of self-absorption effects. In addition, similar results were also found for the relations between  $L_{\text{CO}}$  and the mass of the clumps, while no strong correlation between  $L_{\text{CO}}$  and  $L/M$  was found for this sub-sample.

#### 4.4. The excitation temperature of the CO gas

The increase of  $L_{\text{CO}}$  with the bolometric luminosity of the source (see Fig. 7) suggests that the intensity of the CO transitions may depend on an average warmer temperature of the gas in the clumps due to an increase of the radiation field from the central source (see e.g. van Kempen et al. 2009a). To confirm this scenario, we computed the excitation temperature of the gas,  $T_{\text{ex}}$ , and compared it with the properties of the clumps.

Ideally, the intensity ratio of different CO transitions well separated in energy (e.g. CO (4–3) and CO (7–6)) allows a determination of the excitation temperature of the gas. However, most of the CO profiles in the TOP100 clumps are affected by self-absorption (see Sect. 3.4), causing a considerable underesti-

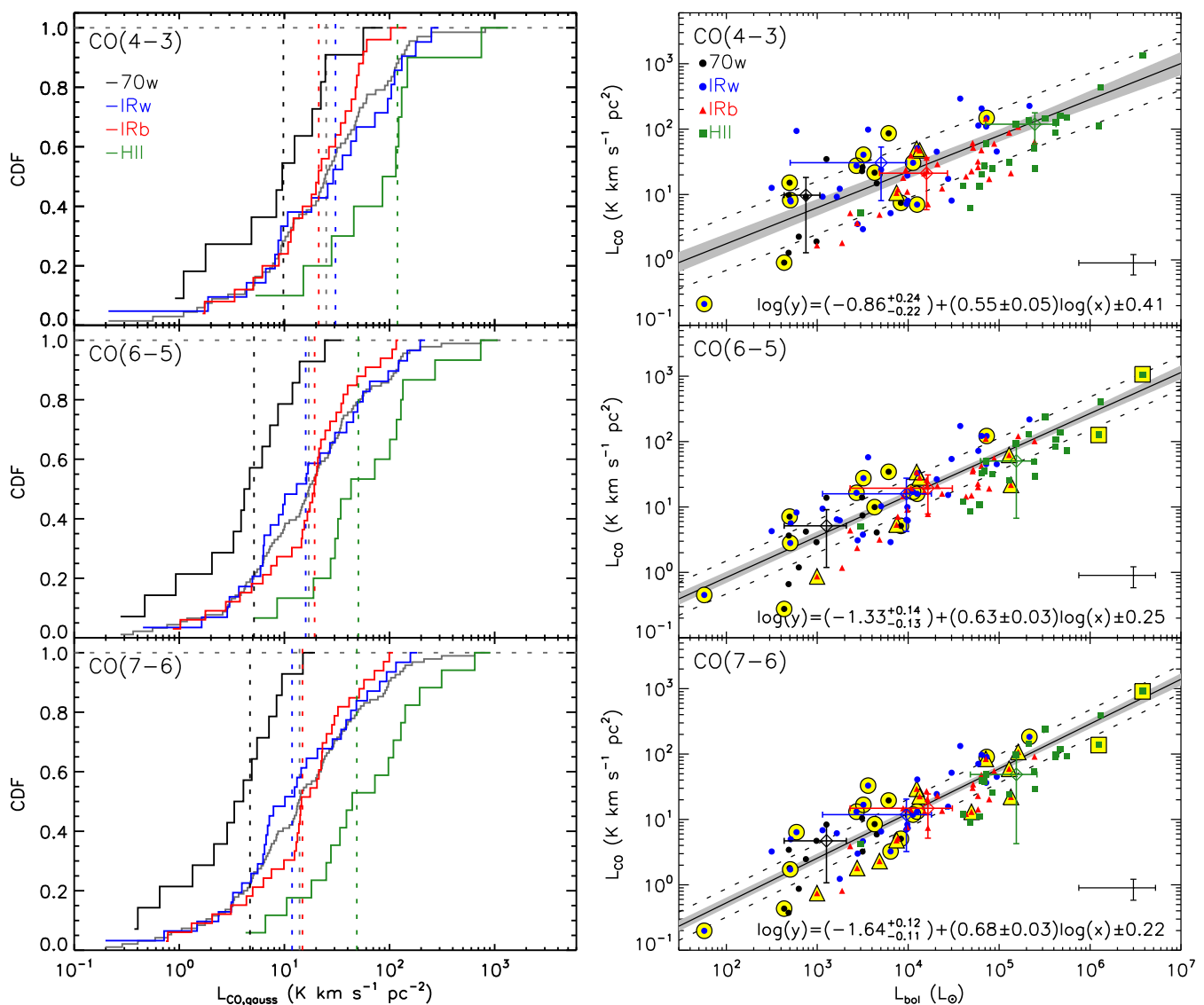


Fig. 7: Left panels: Cumulative distribution function of the line luminosity of the CO (4–3) (upper panel), CO (6–5) (middle) and CO (7–6) emission (bottom) towards the TOP100 sample. The median values per class are shown as vertical dashed lines in their corresponding colours. Right panels: Line luminosity of the same CO  $J$ -transitions versus the bolometric luminosity of the TOP100 sources. The median values for each class are shown as open diamonds and their error bars correspond to the absolute deviation of the data from their median value. Data points highlighted in yellow indicate those sources from which no signs of self-absorption features were identified in the spectrum convolved to  $13''.4$ . The typical error bars are shown at the bottom right side of the plots. The black solid line is the best fit, the light grey shaded area indicates the 68% uncertainty, and the dashed lines show the intrinsic scatter ( $\epsilon$ ) of the relation.

mate of the flux especially in CO (4–3) and leading to unreliable ratios. Moreover, the CO (6–5) and CO (7–6) lines are too close in energy to allow a reliable estimate of the temperature. Alternatively, the excitation temperature can be estimated using the peak intensity of optically thick lines. From the equation of radiative transport, the observed main beam temperature ( $T_{\text{mb}}$ ) can be written in terms of  $T_{\text{ex}}$  as:

$$T_{\text{mb}} = \frac{h\nu}{k} [J_{\nu}(T_{\text{ex}}) - J_{\nu}(T_{\text{bg}})] [1 - \exp(-\tau_{\nu})] \quad (2)$$

where  $J_{\nu}(T) = [\exp(h\nu/kT) - 1]^{-1}$ ,  $T_{\text{bg}}$  is the background temperature and  $\tau_{\nu}$  is the opacity of the source at the frequency  $\nu$ . In the following, we include only the cosmic background as background radiation. Assuming optically thick emission ( $\tau_{\nu} \gg 1$ ),

$T_{\text{ex}}$  is given by:

$$T_{\text{ex}} = \frac{h\nu/k}{\ln \left[ 1 + \frac{h\nu/k}{T_{\text{mb}} + (h\nu/k)J_{\nu}(T_{\text{bg}})} \right]} \quad (3)$$

We computed  $T_{\text{ex}}$  using the peak intensity of the CO (6–5) line from the Gaussian fit (Sect. 3.5) and also from its maximum observed value. Since CO (6–5) may be affected by self-absorption, the maximum observed intensity likely results in a lower limit of the excitation temperature. The values derived using both methods are reported in Table A.7.  $T_{\text{ex}}$  derived from the peak intensity of the Gaussian fit ranges between 14 and 143 K, with a median value of 35 K. The analysis based on the observed intensity delivers similar results ( $T_{\text{ex}}$  values range between 14 and 147 K, with a median value of 34 K).

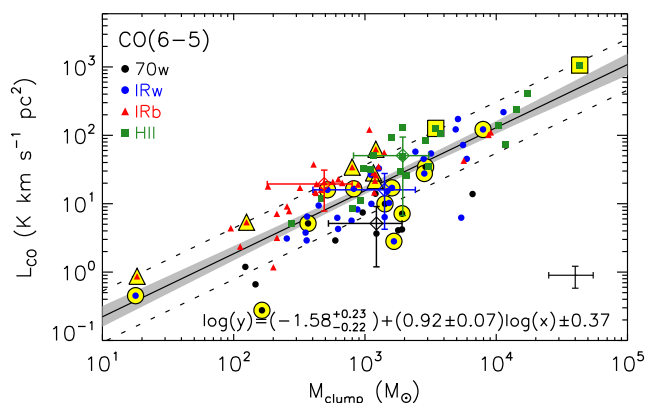


Fig. 8: Same as the right panel of Fig. 7, but displaying the line luminosity of the CO (6–5) emission as a function of the mass of the clumps. Data points highlighted in yellow indicate those sources from which no signs of self-absorption features were identified in the spectrum convolved to  $13''4$ .

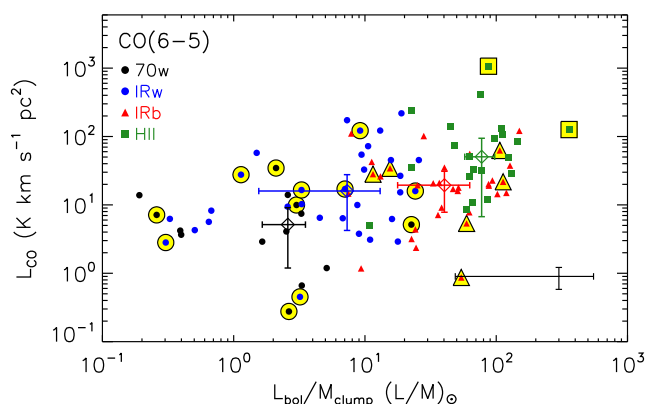


Fig. 9: Same as the right panel of Fig. 7, but displaying  $L_{\text{CO}}$  of the CO (6–5) line as a function of the  $L/M$  ratio of the TOP100 sources. Data points highlighted in yellow indicate those sources from which no signs of self-absorption features were identified in the spectrum convolved to  $13''4$ .

Table 9: Parameters of the fits of  $L_{\text{CO}}$  as a function of the clump properties for the TOP100 clumps that are not affected by self-absorption features.

Transition	Property	$\alpha$	$\beta$	$\epsilon$
CO (4–3)	$L_{\text{bol}}$	$-0.95^{+0.39}_{-0.39}$	$0.58 \pm 0.09$	0.56
	$M_{\text{clump}}$	$-1.60^{+0.28}_{-0.27}$	$1.00 \pm 0.09$	0.31
	$L/M$	$+1.19^{+0.23}_{-0.29}$	$0.19 \pm 0.24$	0.86
CO (6–5)	$L_{\text{bol}}$	$-1.54^{+0.30}_{-0.29}$	$0.68 \pm 0.08$	0.43
	$M_{\text{clump}}$	$-1.92^{+0.30}_{-0.28}$	$1.05 \pm 0.09$	0.38
	$L/M$	$+0.76^{+0.24}_{-0.23}$	$0.43 \pm 0.21$	0.83
CO (7–6)	$L_{\text{bol}}$	$-1.71^{+0.28}_{-0.29}$	$0.71 \pm 0.07$	0.33
	$M_{\text{clump}}$	$-1.95^{+0.34}_{-0.32}$	$1.02 \pm 0.11$	0.41
	$L/M$	$+0.57^{+0.22}_{-0.23}$	$0.53 \pm 0.20$	0.79

**Notes.** The fits were performed by adjusting a model with three free parameters in the form of  $\log(y) = \alpha + \beta \log(x) \pm \epsilon$ , where  $\alpha$ ,  $\beta$  and  $\epsilon$  correspond to the intercept, the slope and the intrinsic scatter, respectively.

The temperature of the gas increases with the evolutionary stage of the clumps and is well correlated with  $L_{\text{bol}}$

Table 10: Spearman rank correlation statistics for the CO line luminosity as a function of the clump properties for the TOP100 clumps that are not affected by self-absorption features.

Property	CO (4–3)	CO (6–5)	CO (7–6)
$L_{\text{bol}}$	0.56, $p = 0.03$ ; $\rho_p = 0.54$	0.81, $p < 0.001$ ; $\rho_p = 0.83$	0.83, $p < 0.001$ ; $\rho_p = 0.89$
$M_{\text{clump}}$	0.72, $p = 0.002$ ; $\rho_p = 0.24$	0.73, $p < 0.001$ ; $\rho_p = 0.50$	0.79, $p < 0.001$ ; $\rho_p = 0.45$
$L/M$	$-0.02$ , $p = 0.95$	$0.39$ , $p = 0.09$	$0.30$ , $p = 0.11$

**Notes.** The rank  $\rho$  and its corresponding probability ( $p$ ) are shown for each comparison. A  $p$ -value of  $< 0.001$  indicate a correlation at 0.001 significance level.  $p$ -values of 0.05, 0.002 and  $< 0.001$  represent the  $\sim 2$ , 3 and  $> 3 \sigma$  confidence levels. For  $L_{\text{bol}}$  and  $M_{\text{clump}}$ , the partial correlation coefficient,  $\rho_p$ , is also shown.

Table 11: Kolmogorov-Smirnov statistics of the excitation temperature of the CO (6–5) line as a function of the evolutionary class of the clumps.

Classes	Observed	Gaussian
70w-IRw	0.43, $p = 0.1$	0.48, $p = 0.02$
70w-IRb	0.83, $p < 0.001$	0.76, $p < 0.001$
70w-H II	1.00, $p < 0.001$	1.00, $p < 0.001$
IRw-IRb	0.56, $p < 0.001$	0.42, $p = 0.005$
IRw-H II	1.00, $p < 0.001$	0.93, $p < 0.001$
IRb-H II	0.68, $p = 0.001$	0.63, $p = 0.001$

**Notes.** The rank KS and its corresponding probability ( $p$ ) are shown for each comparison. A  $p$ -value of  $< 0.001$  indicate a correlation at 0.001 significance level.  $p$ -values of 0.05, 0.002 and  $< 0.001$  represent the  $\sim 2$ , 3 and  $> 3 \sigma$  confidence levels.

( $\rho = 0.69$ ,  $p < 0.001$ , see Fig. 10a). No significant correlation is found with  $M_{\text{clump}}$  ( $\rho = 0.09$ ,  $p = 0.37$ ). On the other hand, the excitation temperature is strongly correlated with  $L/M$  ( $\rho = 0.72$ ,  $p < 0.001$ ), suggesting a progressive warm-up of the gas in more evolved clumps. We further compared the  $T_{\text{ex}}$  values obtained from CO with temperature estimates based on other tracers ( $\text{C}^{17}\text{O}$  (3–2), methyl acetylene,  $\text{CH}_3\text{CCH}$ , ammonia, and the dust, Giannetti et al. 2014, 2017; König et al. 2017; Wien et al. 2012). All temperatures are well correlated ( $\rho \geq 0.44$ ,  $p < 0.001$ ), however, the warm-up of the gas is more evident in the other molecular species than in CO (cf. Giannetti et al. 2017).

## 5. Discussion

### 5.1. Opacity effects

In Sect. 3.4 we found that self-absorption features are present in most of the CO spectra analysed in this work. To address this, we investigated the effects of self-absorption on our analysis and concluded that they are negligible since more than 80% of the CO integrated intensities are recovered in the majority of the sources (Sect. 3.5). We also verified that the steepness of the relations between  $L_{\text{CO}}$  and the clump properties is not affected by self-absorption (Sect. 4.3).

In addition, the CO lines under examination are certainly optically thick, and their opacity is likely to decrease with  $J$ . Indeed, the comparison between  $L_{\text{CO}}$  for different CO transitions and the bolometric luminosity of the clumps (see Sect. 4.3) suggests a systematic increase in the slope

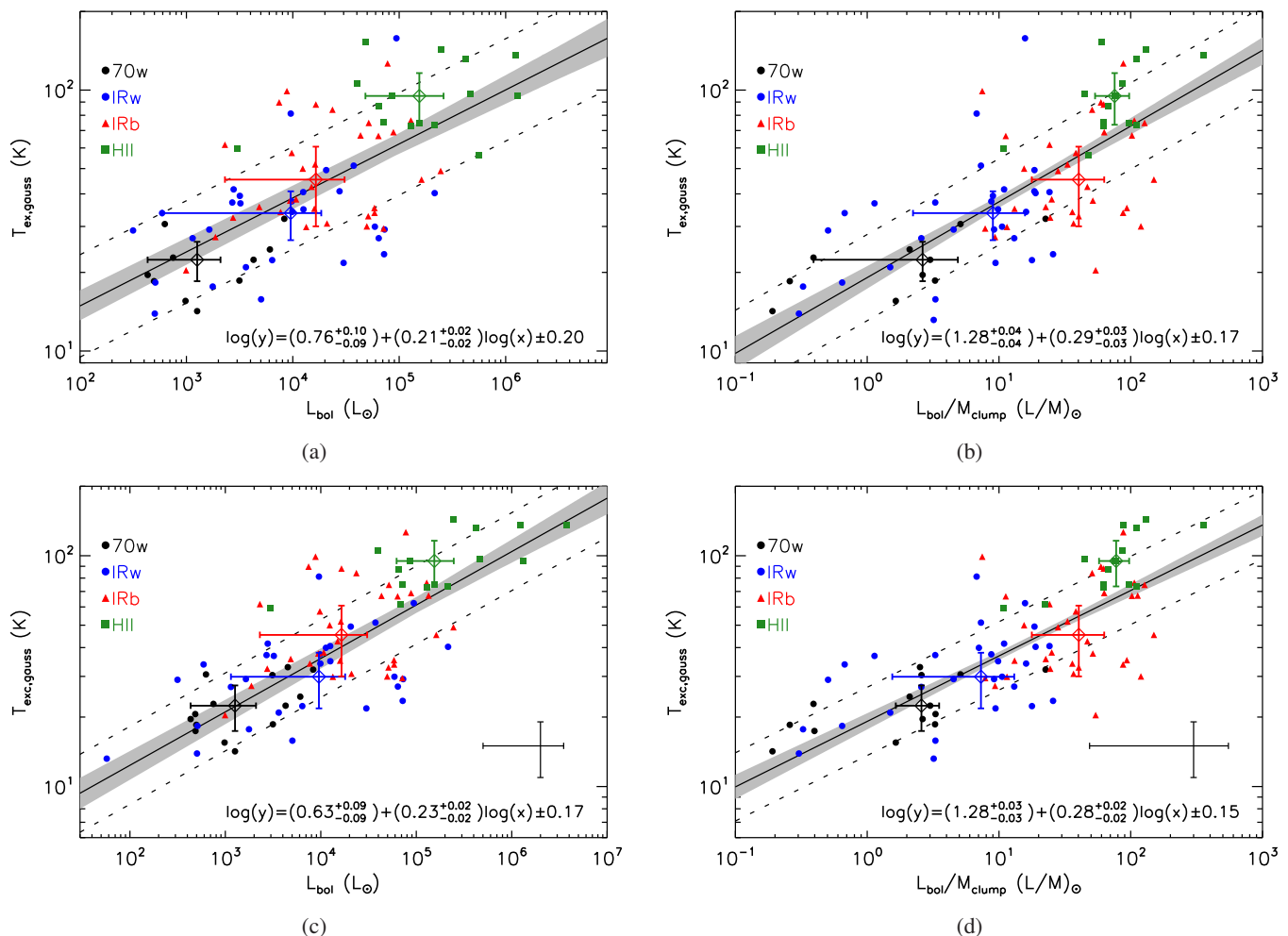


Fig. 10: Excitation temperature of the CO(6–5) line versus the bolometric luminosity of the TOP100 clumps (Left) and the luminosity-to-mass ratio (Right). The excitation temperature was derived using the peak of the Gaussian fit of the CO profiles. The median values for each class are shown as open diamonds and their error bars correspond to the median absolute deviation of the data from their median value. The black solid line is the best fit, the light grey shaded area indicates the 68% uncertainty, and the dashed lines show the intrinsic scatter ( $\epsilon$ ) of the relation. The best fit to the data is indicated by the filled black line.

of the relations as a function of  $J$  (see Table 7 for the derived power-law indices for  $L_{\text{CO}}$  versus  $L_{\text{bol}}$ ). Such a steepening of the slopes with  $J$  is even more evident when including the relation found by San José-García et al. (2013) for CO(10–9) line luminosity in a complementary sample of the TOP100. For the CO(10–9) transition, they derived,  $\log(L_{\text{CO}}) = (-2.9 \pm 0.2) + (0.84 \pm 0.06) \log(L_{\text{bol}})$ , which is steeper than the relations found towards lower- $J$  transitions reported in this work. In Sect. 5.4 we further discuss SJG13 results by analysing their low- and high-mass YSO sub-samples. Our findings suggest that there is a significant offset between the sub-samples, leading to a much steeper relation between  $L_{\text{CO}}$  and  $L_{\text{bol}}$  when considering their whole sample. However, the individual sub-samples follow similar power-law distributions, with power-law indices of  $(0.70 \pm 0.08)$  and  $(0.69 \pm 0.21)$  for the high- and low-mass YSOs, respectively.

In Fig. 11, we present the distribution of the power-law indices of the  $L_{\text{CO}}$  versus  $L_{\text{bol}}$  relations,  $\beta_J$ , as a function of their corresponding upper-level  $J$  number,  $J_{\text{up}}$ . We include also the datapoint from the  $J_{\text{up}} = 10$  line for the high-mass sources of SJG13 (see also discussion in Sect. 5.4. The best fit to the data,

$\beta_J = (0.44 \pm 0.11) + (0.03 \pm 0.02) J_{\text{up}}$ , confirms that the power-law index  $\beta_J$  gets steeper with  $J$ .

The fact that the opacity decreases with  $J$  could result in different behaviours of the line luminosities with  $L_{\text{bol}}$  for different transitions. This effect was recently discussed by Benz et al. (2016) who found that the value of the power-law exponents of the line luminosity of particular molecules and transitions depends mostly on the radius where the line gets optically thick. In the case of CO lines, the systematic increase on the steepness of the  $L_{\text{CO}}$  versus  $L_{\text{bol}}$  relation with  $J$  (see Table 7) suggests that higher  $J$  lines trace more compact gas closer to the source and, thus, a smaller volume of gas is responsible for their emission. Therefore, observations of distinct  $J$  transitions of the CO molecule, from CO(4–3) to CO(7–6) (and even higher  $J$  transitions, considering the CO(10–9) data from SJG13), suggest that the line emission arises and gets optically thick at different radii from the central sources, in agreement with Benz et al. (2016).

## 5.2. Evolution of CO properties with time

In Sect. 4.3, we showed that  $L_{\text{CO}}$  does not correlate with the evolutionary indicator  $L/M$ . This result is unexpected if we consider

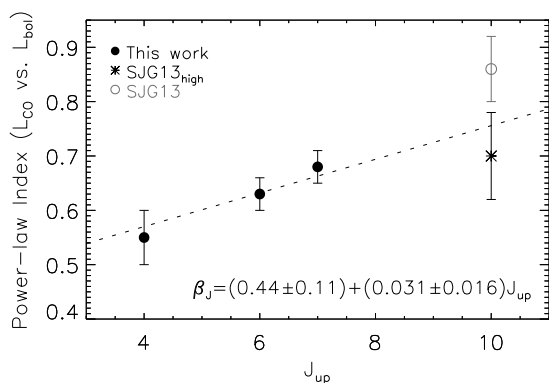


Fig. 11: Power-law indices of the  $L_{\text{CO}}$  versus  $L_{\text{bol}}$  relations for different  $J$  transitions as a function of the upper-level  $J$  number. The  $\beta$  indices from Table 7 (filled black circles) are plotted together with data from SJG13 (open grey circle, excluded from the fit) and the exponent derived for their high-luminosity subsample (\* symbol, see Fig. 12). The best fit is indicated by the dashed black line.

that in TOP100 the evolutionary classes are quite well separated in  $L/M$  (with median values of 2.6, 9.0, 40 and 76 for 70w, IRw, IRb and H II regions, respectively, König et al. 2017).

Previous work on SiO in sources with similar values of  $L/M$  as those of the TOP100 (e.g. Leurini et al. 2014 and Csengeri et al. 2016) found that the line luminosity of low-excitation SiO transitions does not increase with  $L/M$ , while the line luminosity of higher excitation SiO lines (i.e.  $J_{\text{up}} > 3$ ) seems to increase with time. Those authors interpreted these findings in terms of a change of excitation conditions with time which is not reflected in low excitation transitions. This effect likely applies also to low- and mid- $J$  CO lines with relatively low energies ( $\leq 155$  K); higher- $J$  CO transitions could be more sensitive to changes in excitation since they have upper level energies in excess of 300 K (e.g. CO (10–9) or higher  $J$  CO transitions). This hypothesis is strengthened by our finding that the excitation temperature of the gas increases with  $L/M$  (see Fig. 10b). This scenario can be tested with observations of high- $J$  CO transitions which are now made possible by the SOFIA telescope in the range  $J_{\text{up}} = 11$ –16. Also *Herschel*-PACS archive data could be used despite their coarse spectral resolution.

### 5.3. Do embedded H II regions still actively power molecular outflows?

In Sect. 4.2 we showed that H II regions have broad CO lines (see Fig. 6) likely associated with high-velocity outflowing gas. The H II sources in our sample are either compact or unresolved objects in the continuum emission at 5 GHz. Their envelopes still largely consist of molecular gas and have not yet been significantly dispersed by the energetic feedback of the YSOs. Our observations suggest that high-mass YSOs in this phase of evolution still power molecular outflows and are therefore accreting. This result is in agreement with the recent study of Urquhart et al. (2013b) and Cesaroni et al. (2015) who suggested that accretion might still be present during the early stages of evolution of H II regions based on the finding that the Lyman continuum luminosity of several H II regions appears in excess of that expected for a zero-age main-sequence star with the same bolometric luminosity. Such excess could be due to the so-called flashlight effect (e.g. Yorke & Bodenheimer 1999), where

most of the photons escape along the axis of a bipolar outflow. Indeed Cesaroni et al. (2016) further investigated the origin of the Lyman excess looking for infall and outflow signatures in the same sources. They found evidence for both phenomena although with low-angular resolution data. Alternatively, the high-velocity emission seen in CO in the TOP100 in this work and in SiO in the ultra-compact H II regions of Cesaroni et al. (2016) could be associated with other younger unresolved sources in the clump and not directly associated with the most evolved object in the cluster. Clearly, high angular resolution observations (e.g. with ALMA) are needed to shed light on the origin of the high-velocity emission and confirm whether indeed the high-mass YSO ionising the surrounding gas is still actively accreting.

### 5.4. CO line luminosities from low- to high-luminosity sources

In this section, we further study the correlation between  $L_{\text{CO}}$  and the bolometric luminosity of the clumps for different CO transitions to investigate the possible biases that can arise when comparing data with very different linear resolutions. This is important in particular when comparing galactic observations to the increasing number of extragalactic studies of mid- and high- $J$  CO lines (e.g. Weiß et al. 2007; Decarli et al. 2016). We use results from SJG13 for the high energy CO (10–9) line (with a resolution of  $\sim 20''$ ) and from the CO (6–5) and CO (7–6) transitions observed with APEX by vK09. The sources presented by SJG13 cover a broad range of luminosities (from  $< 1 L_{\odot}$  to  $\sim 10^5 L_{\odot}$ ) and are in different evolutionary phases. On the other hand, the sample studied by vK09 consists of eight low-mass YSOs with bolometric luminosities  $\lesssim 30 L_{\odot}$ .

To investigate the dependence of the line luminosity in different CO transitions on  $L_{\text{bol}}$  from low- to high-mass star-forming clumps, we first divided the sources from SJG13 into low- ( $L_{\text{bol}} < 50 L_{\odot}$ ) and high-luminosity ( $L_{\text{bol}} > 50 L_{\odot}$ ) objects. In this way and assuming the limit  $L_{\text{bol}} = 50 L_{\odot}$  adopted by SJG13 as a separation between low- and high-mass YSOs, we defined a subsample of low-mass sources (the targets of vK09 for CO (6–5) and CO (7–6), and those of SJG13 with  $L_{\text{bol}} < 50 L_{\odot}$  for CO  $J = 10$ –9) and one of intermediate- to high-mass clumps (the TOP100 for the mid- $J$  CO lines and the sources from SJG13 with  $L_{\text{bol}} > 50 L_{\odot}$  for CO (10–9)).

In the upper panels of Fig. 12 we compare our data with those of vK09 for the CO (6–5) and CO (7–6) transitions. We could not include the sources of SJG13 in this analysis because observations in the CO (6–5) or CO (7–6) lines are not available. We calculated the CO line luminosity of their eight low-mass YSOs using the integrated intensities centred on the YSO on scales of  $\sim 0.01$  pc (see their Table 3). In order to limit biases due to different beam sizes, we recomputed the CO luminosities from the central position of our map at the original resolution of the CHAMP+ data (see Table 1), probing linear scales ranging from  $\sim 0.04$  to 0.6 pc. We performed three fits on the data: we first considered only the original sources of vK09 and the TOP100 separately, and then combined both samples. The derived power-law indices of the CO (6–5) data are  $0.59 \pm 0.25$  and  $0.59 \pm 0.04$  for the low- and high-luminosity sub-samples, respectively. Although the power-law indices derived for the two sub-samples are consistent within  $1-\sigma$ , the fits are offset by roughly one order of magnitude (from  $-2.75$  to  $-1.54$  dex), indicating that  $L_{\text{CO}}$  values are systematically larger towards high-luminosity sources. Indeed, the change on the offsets explains reasonably well the steeper power-law index found when combining both sub-samples ( $0.74 \pm 0.03$ ). Similar results are found

for CO(7–6), although the difference between the offsets are slight smaller ( $\sim 0.8$  dex). The bottom panel of Fig. 12 presents the CO(10–9) luminosity for the SJG13 sample with the best fit of their low- and high-luminosity sources separately. The derived power-law indices are  $0.69 \pm 0.21$  and  $0.70 \pm 0.08$  for the low- and high-luminosity sub-samples, respectively. The fits are offset by roughly 0.3 dex, which also explains the steeper slope of  $0.84 \pm 0.06$  found by SJG13 when fitting the two sub-samples simultaneously.

We interpret the shift in CO line luminosities between low- and high-luminosity sources as a consequence of the varying linear resolution and sampled volume of gas of the data across the  $L_{\text{bol}}$  axis. In high-mass sources, mid- $J$  CO lines trace extended gas (see the maps presented in Figs. B.1 for the TOP100) probably due to the effect of clustered star formation. Since the data presented in Fig. 12 are taken with comparable angular resolutions, the volume of gas sampled by the data is increasing with  $L_{\text{bol}}$  because sources with high luminosities are on average more distant. For the CO(10–9) data, the two sub-samples are likely differently affected by beam dilution. In close-by low-mass YSOs, the CO(10–9) line is dominated by emission from UV heated outflow cavities (van Kempen et al. 2010) and therefore is extended. In high-mass YSOs, the CO(10–9) line is probably emitted in the inner part of passively heated envelope (Karska et al. 2014) and therefore could suffer from beam dilution. This could explain the smaller offset in the CO(10–9) line luminosity between the low- and high-luminosity sub-samples.

SJG13 and San José-García et al. (2016) found a similar increase in the slope of the line luminosity of the CO(10–9) and of H<sub>2</sub>O transitions versus  $L_{\text{bol}}$  when including extragalactic sources (see Fig. 14 of SJG13 and Fig. 9 of San José-García et al. 2016). These findings clearly outline the difficulties of comparing observations of such different scales and the problems to extend Galactic relations to extragalactic objects.

## 6. Summary

A sample of 99 sources, selected from the ATLASGAL 870  $\mu\text{m}$  survey and representative of the Galactic population of star-forming clumps in different evolutionary stages (from 70  $\mu\text{m}$ -weak clumps to H II regions), was characterised in terms of their CO(4–3), CO(6–5) and CO(7–6) emission.

We first investigated the effects of different linear resolutions on our data. By taking advantage of our relatively high angular resolution maps in the CO(6–5) and CO(7–6) lines, we could study the influence of different beam sizes on the observed line profiles and on the integrated emission. We first convolved the CO(6–5) and CO(7–6) data to a common linear size of  $\sim 0.24$  pc using a distance limited sub-sample of clumps and then to a common angular resolution of  $13''$ , including the single-pointing CO(4–3) data. We verified that the results typically do not depend on the spatial resolution of the data, at least in the range of distances sampled by our sources. The only difference between the two methods is found when comparing the average spectra for each evolutionary class: indeed, only when using spectra that sample the same volume of gas (i.e. same linear resolution) it is possible to detect an increase in line width from 70  $\mu\text{m}$  clumps to H II regions, while the line widths of each evolutionary class are less distinct in the spectra smoothed to the same angular size due to sources at large distances ( $> 12$  kpc). This result is encouraging for studies of large samples of SF regions across the Galaxy based on single-pointing observations.

The analysis of the CO emission led to the following results:

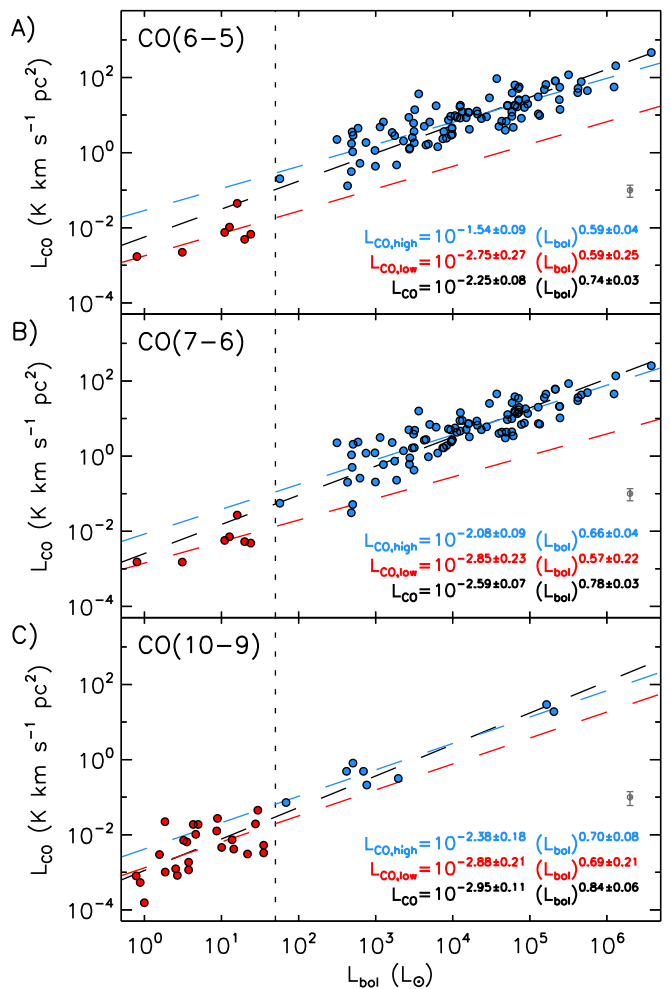


Fig. 12: CO line luminosity as a function of the bolometric luminosity for the CO(6–5) (upper panel), CO(7–6) (middle) and CO(10–9) (bottom) transitions. The fits were performed on the whole dataset (all points, shown with black contours), on the low- and high-luminosity sub-samples (points filled in red and blue, respectively). The CO(6–5) and CO(7–6) data towards low-luminosity sources are from van Kempen et al. (2009a); the CO(10–9) data are from San José-García et al. (2013). The dashed vertical line at  $L_{\text{bol}} = 50 L_{\odot}$  marks the transition from low- to high-mass YSOs. The typical error bars are shown in the bottom right side of the plots.

1. All the sources were detected in the CO(4–3), CO(6–5) and CO(7–6) transitions.
2. The spatial distribution of the CO(6–5) emission ranges between 0.1 and 2.4 pc. The sizes of mid- $J$  CO emission display a moderate correlation with the sub-mm dust mass of the clumps, suggesting that the extension of the gas probed by the CO is linked to the available amount of the total gas in the region. In addition, the CO(6–5) extension is also correlated with the infrared emission probed by the *Herschel*-PACS 70  $\mu\text{m}$  maps towards the 70  $\mu\text{m}$ -bright clumps.
3. The CO profiles can be decomposed using up to three velocity components. The majority of the spectra are well fitted by two components, one narrow ( $\text{FWHM} < 7.5 \text{ km s}^{-1}$ ) and one broad; 30% of the sources need a third and broader component for the CO(6–5) line profile.
4. The FWZP of the CO lines increases with the evolution of the clumps (with median values of 26, 42, 72 and 94 for

70w, IRw, IRb clumps and H II regions, respectively, for the CO(6–5) transition). H II regions are often associated with broad velocity components, with FWHM values up to  $\sim 100 \text{ km s}^{-1}$ . This suggests that accretion, resulting in outflows, is still undergoing in the more evolved clumps of the TOP100.

5. The CO line luminosity increases with the bolometric luminosity of the sources, although it does not seem to increase neither with the mass nor with the  $L/M$  ratio of the clumps.
6. The dependence of the CO luminosity as a function of the bolometric luminosity of the source seems to get steeper with  $J$ . This likely reflects the fact that higher  $J$  CO transitions are more sensitive to the temperature of the gas and likely arise from an inner part of the envelope. These findings are quite robust in terms of self-absorption present in most of the  $^{12}\text{CO}$  emission.
7. The excitation temperature of the clumps was evaluated based on the peak intensity of the Gaussian fit of the CO(6–5) spectra. We found that  $T_{\text{ex}}$  increases as a function of the bolometric luminosity and the luminosity-to-mass ratio of the clumps, as expected for a warming up of the gas from 70w clumps towards H II regions. The observed CO emission towards more luminous and distant objects likely originates from multiple sources within the linear scale probed by the size of beam (up to 0.84 pc), thus, are systematically larger than the emission from resolved and nearby less luminous objects, from which the CO emission is integrated over smaller linear scales ( $\sim 0.01$  pc). We found that the line luminosity of the CO lines shows similar slopes as a function of the bolometric luminosity for low-mass and high-mass star-forming sources. However, as a consequence, the distribution of the CO line luminosity versus the bolometric luminosity follows steeper power-laws when combining low- and high-luminosity sources.

*Acknowledgements.* F.N. thanks to *Fundação de Amparo à Pesquisa do Estado de São Paulo* (FAPESP) for support through processes 2013/11680-2, 2014/20522-4 and 2017/18191-8. T.Cs. acknowledges support from the *Deutsche Forschungsgemeinschaft, DFG* via the SPP (priority programme) 1573 'Physics of the ISM'. We thank the useful comments and suggestions made by an anonymous referee that led to a much improved version of this work.

## References

Benz, A. O., Bruderer, S., van Dishoeck, E. F., et al. 2016, *A&A*, 590, A105  
 Bergin, E. A. & Tafalla, M. 2007, *ARA&A*, 45, 339  
 Beuther, H., Walsh, A., Schilke, P., et al. 2002, *A&A*, 390, 289  
 Carey, S. J., Noriega-Crespo, A., Mizuno, D. R., et al. 2009, *PASP*, 121, 76  
 Cesaroni, R., Pestalozzi, M., Beltrán, M. T., et al. 2015, *A&A*, 579, A71  
 Cesaroni, R., Sánchez-Monge, Á., Beltrán, M. T., et al. 2016, *A&A*, 588, L5  
 Contreras, Y., Schuller, F., Urquhart, J. S., et al. 2013, *A&A*, 549, A45  
 Csengeri, T., Leurini, S., Wyrowski, F., et al. 2016, *A&A*, 586, A149  
 Csengeri, T., Urquhart, J. S., Schuller, F., et al. 2014, *A&A*, 565, A75  
 Cubick, M., Stutzki, J., Ossenkopf, V., Kramer, C., & Röllig, M. 2008, *A&A*, 488, 623  
 de Graauw, T., Helmich, F. P., Phillips, T. G., et al. 2010, *A&A*, 518, L6  
 Decarli, R., Walter, F., Aravena, M., et al. 2016, *ApJ*, 833, 70  
 Faúndez, S., Bronfman, L., Garay, G., et al. 2004, *A&A*, 426, 97  
 Giannetti, A., Leurini, S., Wyrowski, F., et al. 2017, *A&A*  
 Giannetti, A., Wyrowski, F., Brand, J., et al. 2014, *A&A*, 570, A65  
 Gómez-Ruiz, A. I., Gusdorf, A., Leurini, S., et al. 2012, *A&A*, 542, L9  
 Grellmann, R., Preibisch, T., Ratzka, T., et al. 2013, *A&A*, 550, A82  
 Güsten, R., Baryshev, A., Bell, A., et al. 2008, in *Society of Photo-Optical Instrumentation Engineers (SPIE) Conference Series*, Vol. 7020, *Society of Photo-Optical Instrumentation Engineers (SPIE) Conference Series*, 10  
 Güsten, R., Nyman, L. Á., Schilke, P., et al. 2006, *A&A*, 454, L13  
 Hosokawa, T. & Omukai, K. 2009, *ApJ*, 691, 823  
 Karska, A., Herpin, F., Bruderer, S., et al. 2014, *A&A*, 562, A45

Kasemann, C., Güsten, R., Heyminck, S., et al. 2006, in *Society of Photo-Optical Instrumentation Engineers (SPIE) Conference Series*, Vol. 6275, *Society of Photo-Optical Instrumentation Engineers (SPIE) Conference Series*, 0  
 Kim, W.-J., Wyrowski, F., Urquhart, J. S., Menten, K. M., & Csengeri, T. 2017, *A&A*, 602, A37  
 Klein, T., Ciechanowicz, M., Leinz, C., et al. 2014, *IEEE Trans. on Terahertz Science and Technology*, 4, 588  
 König, C., Urquhart, J. S., Csengeri, T., et al. 2017, *A&A*, 599, A139  
 Krumholz, M. R., Klein, R. I., McKee, C. F., Offner, S. S. R., & Cunningham, A. J. 2009, *Science*, 323, 754  
 Leurini, S., Codella, C., López-Sepulcre, A., et al. 2014, *A&A*, 570, A49  
 Leurini, S., Wyrowski, F., Herpin, F., et al. 2013, *A&A*, 550, A10  
 Leurini, S., Wyrowski, F., Wiesemeyer, H., et al. 2015, *A&A*, 584, A70  
 Molinari, S., Pezzuto, S., Cesaroni, R., et al. 2008, *A&A*, 481, 345  
 Molinari, S., Schisano, E., Elia, D., et al. 2016, *A&A*, 591, A149  
 Molinari, S., Swinyard, B., Bally, J., et al. 2010, *PASP*, 122, 314  
 Mottram, J. C., van Dishoeck, E. F., Kristensen, L. E., et al. 2017, *A&A*, 600, A99  
 Rosen, A. L., Krumholz, M. R., McKee, C. F., & Klein, R. I. 2016, *MNRAS*, 463, 2553  
 San José-García, I., Mottram, J. C., Kristensen, L. E., et al. 2013, *A&A*, 553, A125  
 San José-García, I., Mottram, J. C., van Dishoeck, E. F., et al. 2016, *A&A*, 585, A103  
 Saraceno, P., Andre, P., Ceccarelli, C., Griffin, M., & Molinari, S. 1996, *A&A*, 309, 827  
 Schuller, F., Menten, K. M., Contreras, Y., et al. 2009, *A&A*, 504, 415  
 Schulz, A., Henkel, C., Beckmann, U., et al. 1995, *A&A*, 295, 183  
 Tang, X. D., Henkel, C., Wyrowski, F., et al. 2018, *A&A*, 611, A6  
 Urquhart, J. S., König, C., Giannetti, A., et al. 2018, *MNRAS*, 473, 1059  
 Urquhart, J. S., Moore, T. J. T., Schuller, F., et al. 2013a, *MNRAS*, 431, 1752  
 Urquhart, J. S., Thompson, M. A., Moore, T. J. T., et al. 2013b, *MNRAS*, 435, 400  
 van Kempen, T. A., Kristensen, L. E., Herczeg, G. J., et al. 2010, *A&A*, 518, L121  
 van Kempen, T. A., van Dishoeck, E. F., Güsten, R., et al. 2009a, *A&A*, 507, 1425  
 van Kempen, T. A., van Dishoeck, E. F., Hogerheijde, M. R., & Güsten, R. 2009b, *A&A*, 508, 259  
 Weiß, A., Downes, D., Neri, R., et al. 2007, *A&A*, 467, 955  
 Wielen, M., Wyrowski, F., Schuller, F., et al. 2012, *A&A*, 544, A146  
 Wu, J., Evans, II, N. J., Gao, Y., et al. 2005, *ApJ*, 635, L173  
 Yorke, H. W. & Bodenheimer, P. 1999, *ApJ*, 525, 330  
 Zhang, X., Lee, Y., Bolatto, A., & Stark, A. A. 2001, *ApJ*, 553, 274  
 Zinnecker, H. & Yorke, H. W. 2007, *ARA&A*, 45, 481

## **Appendix A: Full tables**

Here, we present the full version of tables shown in the paper. Table A.1 presents the properties of the observed clumps. Tables A.2, A.3 and A.4 present the Gaussian components of each source for the CO (4–3), CO (6–5) and CO (7–6) transitions, respectively. The extension of the CO (6–5) emission is listed in Table A.5. Table A.6 displays the integrated properties of the CO lines studied in this work. Finally, the excitation temperature derived from the CO (6–5) spectra is presented in Table A.7.



Table A.1: Properties of the TOP100 sources.

ID	CSC Name	RA(J2000) (HH:MM:SS)	DEC(J2000) (DD:MM:SS)	Offset CSC (",")	GCSC Name	Offset GCSC (",")	$V_{\text{lsr}}$ ( $\text{km s}^{-1}$ )	$d$ (kpc)	$\log\left(\frac{L_{\text{bol}}}{L_{\odot}}\right)$	$\log\left(\frac{M_{\text{clump}}}{M_{\odot}}\right)$	Class
1	AGAL008.684-00.367	18:06:23.27	-21:37:12.7	(+2.5,+6.8)	G008.6834-0.3675	(+1.9,+4.7)	37.3	4.8	4.44	3.17	IRw
2	AGAL008.706-00.414	18:06:36.81	-21:37:18.1	(-1.9,-1.7)	G008.7064-0.4136	(-1.3,+1.5)	37.6	4.8	2.70	3.22	IRw
3	AGAL010.444-00.017	18:08:44.94	-19:54:32.0	(-3.2,-4.7)	G010.4446-0.0178	(-0.8,-4.0)	74.8	8.6	4.05	3.21	IRw
4	AGAL010.472+00.027	18:08:38.24	-19:51:49.6	(-1.0,+0.6)	G010.4722+0.0277	(-3.1,+0.3)	66.3	8.6	5.67	4.02	H II
5	AGAL010.624-00.384	18:10:28.87	-19:55:47.4	(+0.0,-0.7)	G010.6237-0.3833	(-4.6,-0.6)	-2.8	5.0	5.63	3.58	H II
6	AGAL012.804-00.199	18:14:13.75	-17:55:31.2	(-5.4,-13.6)	G012.8057-0.1994	(-2.9,-9.2)	35.3	2.4	5.39	3.27	H II
7	AGAL013.178+00.059	18:14:00.77	-17:28:37.8	(+6.8,-2.1)	G013.1768+0.0599	(+2.9,-3.0)	49.3	2.4	3.92	2.57	70w
8	AGAL013.658-00.599	18:17:24.25	-17:22:11.9	(+1.2,+2.1)	G013.6570-0.5992	(+1.6,+0.7)	47.4	4.5	4.32	2.76	IRb
9	AGAL014.114-00.574	18:18:13.21	-16:57:17.4	(-0.5,-2.3)	G014.1145-0.5745	(+1.6,-2.0)	19.5	2.6	3.50	2.55	IRw
10	AGAL014.194-00.194	18:16:58.81	-16:42:15.6	(+0.1,-1.7)	G014.1944-0.1939	(-0.2,-0.6)	38.9	3.9	3.43	2.91	IRw
11	AGAL014.492-00.139	18:17:22.19	-16:25:00.3	(-0.4,+2.0)	G014.4918-0.1389	(+0.2,+0.6)	39.5	3.9	2.88	3.28	70w
12	AGAL014.632-00.577	18:19:14.82	-16:30:02.0	(+7.7,+0.2)	G014.6323-0.5763	(+6.4,+1.7)	17.9	1.8	3.44	2.40	IRw
13	AGAL015.029-00.669	18:20:22.64	-16:11:42.7	(-3.6,+5.7)	G015.0292-0.6706	(+4.2,+1.8)	18.5	2.0	5.13	3.08	IRb
14	AGAL018.606-00.074	18:25:08.35	-12:45:22.8	(-0.8,-0.5)	G018.6057-0.0747	(+0.8,-2.0)	44.9	4.3	2.77	2.94	IRw
15	AGAL018.734-00.226	18:25:56.21	-12:42:49.3	(-2.6,-0.4)	G018.7344-0.2261	(+1.1,-0.3)	40.8	12.5	4.86	3.90	IRw
16	AGAL018.888-00.474	18:27:07.58	-12:41:39.5	(+1.2,+1.5)	G018.8870-0.4741	(-0.3,-0.3)	65.4	4.7	3.51	3.45	IRw
17	AGAL019.882-00.534	18:29:14.71	-11:50:25.4	(-6.5,-1.6)	G019.8832-0.5347	(-1.1,-0.4)	43.7	3.7	4.09	2.90	IRb
18	AGAL022.376+00.447	18:30:24.22	-09:10:38.9	(-1.4,+3.2)	G022.3752+0.4472	(-1.6,+1.0)	52.9	4.0	2.50	2.80	IRw
19	AGAL023.206-00.377	18:34:55.09	-08:49:18.1	(-0.4,+1.2)	G023.2056-0.3772	(-3.7,+1.1)	76.8	4.6	4.10	3.11	IRw
20	AGAL024.629+00.172	18:35:35.71	-07:18:08.7	(-2.7,-7.6)	G024.6294+0.1731	(-2.9,-6.0)	114.5	7.7	3.70	3.18	IRw
21	AGAL028.564-00.236	18:44:17.89	-03:59:44.3	(+1.8,+5.1)	G028.5637-0.2358	(-0.2,+3.8)	86.5	5.5	3.25	3.73	IRw
22	AGAL028.861+00.066	18:43:46.20	-03:35:29.2	(-2.0,-3.8)	G028.8614+0.0664	(-0.0,-0.9)	103.0	7.4	5.21	3.03	IRb
23	AGAL030.818-00.056	18:47:46.60	-01:54:30.1	(+2.0,+4.4)	G030.8166-0.0561	(+1.2,+1.0)	97.8	4.9	4.80	3.75	IRb
24	AGAL030.848-00.081	18:47:55.43	-01:53:37.7	(-1.1,+7.0)	G030.8472-0.0817	(+3.7,+4.4)	93.8	4.9	3.49	3.08	70w
25	AGAL030.893+00.139	18:47:13.69	-01:45:07.6	(-6.1,+2.4)	G030.8930+0.1383	(-1.9,+2.6)	106.7	4.9	2.70	3.28	70w
26	AGAL031.412+00.307	18:47:34.40	-01:12:46.5	(-1.9,+3.5)	G031.4120+0.3076	(-4.8,+2.3)	97.1	4.9	4.84	3.49	H II
27	AGAL034.258+00.154	18:53:18.68	+01:14:58.5	(-3.9,+1.6)	G034.2572+0.1535	(-1.2,-0.3)	58.1	1.6	4.68	2.91	H II
28	AGAL034.401+00.226	18:53:18.78	+01:24:38.7	(+0.4,-1.7)	G034.4005+0.2262	(-2.6,-2.4)	56.9	1.6	3.48	2.44	H II
29	AGAL034.411+00.234	18:53:18.31	+01:25:24.6	(-2.8,-1.9)	G034.4112+0.2344	(-1.0,-0.0)	57.6	1.6	3.68	2.33	IRb
30	AGAL034.821+00.351	18:53:38.29	+01:50:28.2	(-3.2,-0.4)	G034.8206+0.3504	(-3.8,-2.1)	56.5	1.6	3.44	2.05	IRb
31	AGAL035.197-00.742	18:58:13.09	+02:40:38.9	(-2.6,-0.5)	G035.1976-0.7427	(-0.2,-0.7)	33.4	2.2	4.37	2.67	IRb
32	AGAL037.554+00.201	18:59:10.06	+04:12:18.5	(-0.9,-2.0)	G037.5537+0.2006	(-1.5,-3.8)	85.2	6.7	4.71	3.10	IRb
33	AGAL043.166+00.011	19:10:13.64	+09:06:16.7	(-3.5,-6.3)	G043.1668+0.0115	(-3.0,-2.3)	4.9	11.1	6.58	4.64	H II
34	AGAL049.489-00.389	19:23:43.30	+14:30:26.5	(+13.5,+3.2)	G049.4888-0.3882	(+12.9,+3.7)	56.6	5.4	5.75	4.07	H II
35	AGAL053.141+00.069	19:29:17.52	+17:56:22.3	(+3.4,-4.8)	G053.1415+0.0701	(+0.1,-1.2)	21.5	1.6	3.36	1.98	IRb
36	AGAL059.782+00.066	19:43:11.06	+23:44:05.4	(-2.4,-1.6)	G059.7830+0.0657	(-2.1,+0.6)	22.2	2.2	3.99	2.41	IRb
37	AGAL301.136-00.226	12:35:35.51	-63:02:30.5	(-10.5,-1.6)	G301.1365-0.2256	(-5.2,-1.4)	-39.3	4.4	5.33	3.29	H II
38	AGAL305.192-00.006	13:11:14.92	-62:47:26.6	(-14.3,+0.2)	G305.1935-0.0059	(-4.3,+0.1)	-34.2	3.8	4.10	2.71	IRw
39	AGAL305.209+00.206	13:11:13.72	-62:34:38.5	(+6.7,-3.6)	G305.2083+0.2063	(-2.3,-2.3)	-42.2	3.8	4.95	3.15	IRb
40	AGAL305.562+00.014	13:14:26.54	-62:44:27.3	(-1.7,+3.2)	G305.5628+0.0137	(-0.3,+1.5)	-39.8	3.8	4.71	2.61	IRb
41	AGAL305.794-00.096	13:16:34.48	-62:49:45.7	(-25.3,+5.1)	G305.7949-0.0965	(-18.6,+2.8)	-40.9	3.8	2.99	2.77	70w
42	AGAL309.384-00.134	13:47:22.79	-62:18:09.8	(+21.0,+0.1)	G309.3826-0.1332	(+7.4,+1.9)	-51.3	5.3	4.20	3.08	IRb
43	AGAL310.014+00.387	13:51:38.19	-61:39:17.3	(+3.0,+4.1)	G310.0135+0.3877	(-0.4,+4.0)	-41.3	3.6	4.70	2.62	IRb

Table A.1: continued.

ID	CSC Name	RA(J2000) (HH:MM:SS)	DEC(J2000) (DD:MM:SS)	Offset CSC (",")	GCSC Name	Offset GCSC (",")	$V_{\text{lsr}}$ ( $\text{km s}^{-1}$ )	$d$ (kpc)	$\log\left(\frac{L_{\text{bol}}}{L_{\odot}}\right)$	$\log\left(\frac{M_{\text{clump}}}{M_{\odot}}\right)$	Class
44	AGAL313.576+00.324	14:20:08.44	-60:42:07.0	(-3.2,+2.0)	G313.5763+0.3243	(+1.1,+2.7)	-46.9	3.8	3.97	2.26	IRb
45	AGAL316.641-00.087	14:44:18.46	-59:55:17.8	(+4.9,+4.5)	G316.6403-0.0877	(+2.1,+3.0)	-17.7	1.2	3.00	1.26	IRb
46	AGAL317.867-00.151	14:53:16.76	-59:26:36.9	(-1.7,+4.1)	G317.8680-0.1514	(+6.0,+3.2)	-40.6	3.0	3.22	2.56	IRw
47	AGAL318.779-00.137	14:59:33.29	-59:00:36.6	(-0.8,+1.9)	G318.7790-0.1376	(+1.0,+1.0)	-39.4	2.8	3.81	2.56	IRw
48	AGAL320.881-00.397	15:14:33.61	-58:11:31.9	(-7.8,+1.5)	G320.8803-0.3970	(-9.1,+2.2)	-46.0	10.0	3.78	3.46	70w
49	AGAL326.661+00.519	15:45:03.20	-54:09:13.9	(-5.2,+2.7)	G326.6607+0.5190	(-4.7,+2.4)	-39.8	1.8	3.87	2.10	IRb
50	AGAL326.987-00.032	15:49:08.36	-54:23:04.7	(-0.4,-3.1)	G326.9871-0.0317	(-4.8,-1.3)	-58.6	4.0	3.06	2.65	IRw
51	AGAL327.119+00.509	15:47:33.56	-53:52:41.9	(-6.7,-2.0)	G327.1197+0.5099	(-8.4,+0.8)	-83.7	5.5	4.77	2.83	IRb
52	AGAL327.393+00.199	15:50:19.55	-53:57:04.6	(-10.6,-0.3)	G327.3928+0.1984	(-8.8,-2.2)	-89.2	5.9	4.13	3.07	IRb
53	AGAL329.029-00.206	16:00:31.50	-53:12:38.8	(+6.7,-14.3)	G329.0303-0.2022	(-2.7,-1.8)	-43.2	11.5	5.33	4.06	IRw
54	AGAL329.066-00.307	16:01:09.93	-53:16:05.4	(-2.6,+2.1)	G329.0656-0.3076	(-1.3,+1.0)	-41.9	11.6	4.85	3.96	IRb
55	AGAL330.879-00.367	16:10:20.62	-52:06:11.0	(-4.9,+3.9)	G330.8788-0.3681	(-5.2,+1.3)	-62.6	4.2	5.19	3.20	H II
56	AGAL330.954-00.182	16:09:53.25	-51:54:54.8	(-6.0,+0.1)	G330.9545-0.1828	(-5.0,+0.1)	-92.0	9.3	6.12	4.24	H II
57	AGAL331.709+00.582	16:10:06.19	-50:50:28.6	(+7.8,+0.9)	G331.7084+0.5834	(+0.7,+1.4)	-67.3	10.5	4.57	3.71	IRw
58	AGAL332.094-00.421	16:16:16.62	-51:18:26.0	(+0.2,+1.7)	G332.0946-0.4210	(+0.8,+2.3)	-57.5	3.6	4.77	2.80	IRb
59	AGAL332.826-00.549	16:20:10.69	-50:53:19.6	(+3.3,+4.1)	G332.8262-0.5493	(+5.2,+4.6)	-57.4	3.6	5.38	3.29	H II
60	AGAL333.134-00.431	16:21:02.20	-50:35:12.6	(+4.0,+2.3)	G333.1341-0.4314	(+4.7,-0.6)	-53.5	3.6	5.62	3.46	H II
61	AGAL333.284-00.387	16:21:30.64	-50:26:54.3	(+5.8,-4.7)	G333.2841-0.3868	(+4.7,-3.9)	-52.4	3.6	5.11	3.32	H II
62	AGAL333.314+00.106	16:19:28.79	-50:04:42.9	(-1.5,+1.2)	G333.3139+0.1057	(-3.4,-0.4)	-46.5	3.6	4.03	2.63	IRb
63	AGAL333.604-00.212	16:22:09.58	-50:06:01.1	(-0.6,+1.7)	G333.6036-0.2130	(-1.5,-1.4)	-47.1	3.6	6.09	3.54	H II
64	AGAL333.656+00.059	16:21:11.83	-49:52:16.7	(-4.5,+0.6)	G333.6563+0.0587	(+0.8,+0.4)	-85.2	5.3	3.63	3.15	70w
65	AGAL335.789+00.174	16:29:47.62	-48:15:51.4	(-5.0,-0.4)	G335.7896+0.1737	(+2.1,+0.0)	-50.6	3.7	4.31	3.04	IRw
66	AGAL336.958-00.224	16:36:17.29	-47:40:49.1	(-3.7,+3.2)	G336.9574-0.2247	(-0.1,+1.5)	-71.3	10.9	3.56	3.38	IRw
67	AGAL337.176-00.032	16:36:18.70	-47:23:24.5	(+2.5,+4.3)	G337.1751-0.0324	(+0.3,+2.3)	-68.2	11.0	4.77	3.75	IRw
68	AGAL337.258-00.101	16:36:56.58	-47:22:29.1	(-4.8,+1.2)	G337.2580-0.1012	(-0.9,+1.3)	-68.3	11.0	4.48	3.50	IRw
69	AGAL337.286+00.007	16:36:34.63	-47:16:50.9	(-0.7,+0.6)	G337.2860+0.0083	(-1.0,+2.9)	-107.5	9.4	3.10	3.82	70w
70	AGAL337.406-00.402	16:38:51.00	-47:27:58.8	(-0.2,+1.0)	G337.4052-0.4024	(+0.1,-0.6)	-40.9	3.3	4.93	3.04	H II
71	AGAL337.704-00.054	16:38:29.69	-47:00:38.2	(-0.8,-2.9)	G337.7045-0.0535	(+1.0,-0.3)	-47.4	12.3	5.50	4.15	H II
72	AGAL337.916-00.477	16:41:10.51	-47:08:06.7	(+2.5,+2.3)	G337.9154-0.4773	(+2.5,+1.5)	-39.5	3.2	5.11	3.08	IRb
73	AGAL338.066+00.044	16:39:28.79	-46:40:30.4	(-4.2,-4.2)	G338.0663+0.0445	(-5.2,-2.1)	-70.1	4.7	3.50	2.98	70w
74	AGAL338.786+00.476	16:40:22.30	-45:51:05.3	(+3.6,-0.4)	G338.7851+0.4767	(-3.3,+0.3)	-64.0	4.5	2.69	3.09	70w
75	AGAL338.926+00.554	16:40:34.50	-45:41:46.7	(-3.2,+4.9)	G338.9249+0.5539	(-2.7,+2.9)	-61.6	4.4	4.97	3.78	IRw
76	AGAL339.623-00.122	16:46:06.21	-45:36:49.5	(+6.0,+2.9)	G339.6225-0.1220	(+5.8,+3.8)	-34.6	3.0	4.18	2.50	IRb
77	AGAL340.374-00.391	16:50:02.85	-45:12:45.2	(-5.8,+3.1)	G340.3736-0.3904	(-6.7,+2.4)	-43.4	3.6	2.71	2.90	IRw
78	AGAL340.746-01.001	16:54:04.02	-45:18:46.7	(-7.1,+1.8)	G340.7456-1.0014	(-6.3,-0.4)	-29.4	2.8	3.89	2.33	IRb
79	AGAL340.784-00.097	16:50:15.36	-44:42:30.1	(-4.7,-2.1)	G340.7848-0.0968	(-5.5,+1.3)	-101.7	10.0	4.86	3.45	IRw
80	AGAL341.217-00.212	16:52:18.19	-44:26:53.1	(-3.2,-1.2)	G341.2179-0.2122	(-1.0,+0.7)	-43.6	3.7	4.21	2.69	IRb
81	AGAL342.484+00.182	16:55:02.31	-43:12:59.2	(+2.3,-2.0)	G342.4836+0.1831	(-0.4,-2.7)	-41.6	12.6	4.81	3.69	IRw
82	AGAL343.128-00.062	16:58:17.47	-42:52:09.3	(-3.1,+4.8)	G343.1271-0.0632	(-1.0,+2.0)	-30.3	3.0	4.86	3.06	H II
83	AGAL343.756-00.164	17:00:50.14	-42:26:14.7	(-0.8,+2.0)	G343.7559-0.1640	(-1.5,+2.3)	-28.2	2.9	4.00	2.79	IRw
84	AGAL344.227-00.569	17:04:07.71	-42:18:41.3	(+2.3,+0.8)	G344.2275-0.5688	(-0.4,+1.7)	-22.3	2.5	3.99	3.05	IRw
85	AGAL345.003-00.224	17:05:11.26	-41:29:06.6	(-3.6,-1.2)	G345.0029-0.2241	(-3.3,-1.2)	-26.9	3.0	4.81	2.99	H II
86	AGAL345.488+00.314	17:04:28.26	-40:46:26.1	(-0.6,+0.7)	G345.4871+0.3142	(-0.9,-0.6)	-17.7	2.2	4.79	2.97	H II

Table A.1: continued.

ID	CSC Name	RA(J2000) (HH:MM:SS)	DEC(J2000) (DD:MM:SS)	Offset CSC (",")	GCSC Name	Offset GCSC (",")	$V_{\text{lsr}}$ ( $\text{km s}^{-1}$ )	$d$ (kpc)	$\log\left(\frac{L_{\text{bol}}}{L_{\odot}}\right)$	$\log\left(\frac{M_{\text{clump}}}{M_{\odot}}\right)$	Class
87	AGAL345.504+00.347	17:04:23.18	-40:44:23.3	(-2.3,-1.6)	G345.5045+0.3481	(-5.8,+0.4)	-17.8	2.3	4.64	2.63	IRb
88	AGAL345.718+00.817	17:03:06.25	-40:17:04.2	(+0.5,-2.1)	G345.7172+0.8176	(-1.9,-2.5)	-11.2	1.6	3.27	2.30	IRb
89	AGAL351.131+00.771	17:19:34.58	-35:56:47.7	(-0.6,+0.3)	G351.1314+0.7709	(+1.5,+1.8)	-5.3	1.8	2.80	2.09	70w
90	AGAL351.161+00.697	17:19:56.97	-35:57:52.2	(+7.0,+2.2)	G351.1598+0.6982	(+0.4,+0.4)	-6.5	1.8	3.94	3.07	IRb
91	AGAL351.244+00.669	17:20:19.14	-35:54:42.0	(-10.5,-0.3)	G351.2437+0.6687	(-8.1,-3.0)	-3.4	1.8	4.89	2.95	IRb
92	AGAL351.416+00.646	17:20:53.65	-35:47:00.8	(-8.3,-2.2)	G351.4161+0.6464	(-12.8,-0.1)	-7.4	1.3	4.60	2.67	H II
93	AGAL351.444+00.659	17:20:55.49	-35:45:07.8	(-12.7,-4.0)	G351.4441+0.6579	(-7.9,-6.9)	-4.3	1.3	3.98	3.15	IRw
9494	AGAL351.571+00.762	17:20:51.05	-35:35:22.4	(-2.4,-2.9)	G351.5719+0.7631	(-0.7,+1.7)	-3.4	1.3	2.64	2.22	70w
95	AGAL351.581-00.352	17:25:25.30	-36:12:47.2	(-4.7,+2.1)	G351.5815-0.3528	(+0.3,+3.0)	-95.4	6.8	5.39	3.94	IRb
96	AGAL351.774-00.537	17:26:42.55	-36:09:21.5	(+2.7,+0.7)	G351.7747-0.5369	(+2.5,+3.2)	-2.8	1.0	4.22	2.42	IRb
97	AGAL353.066+00.452	17:26:13.58	-34:31:54.8	(-3.5,+1.3)	G353.0670+0.4519	(-0.4,+3.6)	1.5	0.9	1.76	1.25	IRw
98	AGAL353.417-00.079	17:29:19.13	-34:32:14.6	(-1.3,+9.7)	G353.4173-0.0803	(+2.9,+6.8)	-54.9	6.1	3.65	3.25	70w
99	AGAL354.944-00.537	17:35:12.04	-33:30:28.0	(-3.3,+3.9)	G354.9437-0.5381	(-4.2,+1.0)	-5.6	1.9	2.68	2.17	70w

**Notes.** The columns are as follows: (1) ID of each source; (2) name from the ATLASGAL-CSC catalogue from Contreras et al. (2013); (3)–(4) Equatorial coordinates (J2000) of the central position of the CHAMP<sup>+</sup> maps; (5) offset between the CSC and the central position of the CHAMP<sup>+</sup> maps; (6) name from the ATLASGAL-GCSC catalogue from Csengeri et al. (2014); (7) offset between GCSC and the central position of the CHAMP<sup>+</sup> maps; (8) the local standard rest velocity ( $V_{\text{lsr}}$ ) from the C<sup>17</sup>O (3–2) data from Giannetti et al. (2014); (9)–(11) distances, bolometric luminosities and clump masses from König et al. (2017); (12) classification of the clump: 70  $\mu\text{m}$  weak (70w), infrared weak (IRw), infrared bright (IRb) or H II regions (H II) from König et al. (2017).

Table A.2: Gaussian decomposition of the CO (4–3) profiles towards the TOP100 sample.

ID	CSC Name	C <sub>1</sub>	V <sub>peak</sub> (km s <sup>-1</sup> )	FWHM (km s <sup>-1</sup> )	T <sub>peak</sub> (K)	C <sub>2</sub>	V <sub>peak</sub> (km s <sup>-1</sup> )	FWHM (km s <sup>-1</sup> )	T <sub>peak</sub> (K)	C <sub>3</sub>	V <sub>peak</sub> (km s <sup>-1</sup> )	FWHM (km s <sup>-1</sup> )	T <sub>peak</sub> (K)
2	AGAL008.706–00.414	N	38.1	7.1	4.9	–	–	–	–	–	–	–	–
3	AGAL010.444–00.017	B	73.8	9.3	3.1	P2	65.2	4.9	2.1	–	–	–	–
4	AGAL010.472+00.027	N	64.6	6.2	22.8	B	68.0	12.7	11.1	–	–	–	–
5	AGAL010.624–00.384	B	–2.8	12.7	51.2	–	–	–	–	–	–	–	–
6	AGAL012.804–00.199	B	36.6	14.9	43.6	–	–	–	–	–	–	–	–
7	AGAL013.178+00.059	B	48.3	11.8	9.2	–	–	–	–	–	–	–	–
8	AGAL013.658–00.599	N	48.6	7.1	8.7	B	46.4	49.5	1.6	–	–	–	–
10	AGAL014.194–00.194	B1	40.1	9.1	10.4	B2	39.7	23.4	3.4	–	–	–	–
11	AGAL014.492–00.139	N	40.1	7.5	7.9	B	27.2	70.9	0.7	–	–	–	–
12	AGAL014.632–00.577	B1	17.4	7.6	14.0	B2	22.1	13.8	1.2	–	–	–	–
13	AGAL015.029–00.669	B	19.6	9.3	55.0	–	–	–	–	–	–	–	–
14	AGAL018.606–00.074	B	45.2	7.5	9.9	–	–	–	–	–	–	–	–
15	AGAL018.734–00.226	N	39.4	4.9	11.0	B	39.6	27.8	1.4	–	–	–	–
16	AGAL018.888–00.474	B	65.7	11.9	14.3	–	–	–	–	–	–	–	–
17	AGAL019.882–00.534	B1	44.3	11.0	18.2	B2	43.1	27.8	6.5	B3	86.6	29.2	0.3
19	AGAL023.206–00.377	B1	78.1	16.7	13.0	B2	87.5	64.1	1.4	–	–	–	–
20	AGAL024.629+00.172	N	114.0	3.2	3.3	B	116.7	13.9	2.5	–	–	–	–
21	AGAL028.564–00.236	B	87.2	8.4	5.9	–	–	–	–	–	–	–	–
23	AGAL030.818–00.056	B1	97.3	8.0	25.3	B2	101.7	19.2	5.6	–	–	–	–
24	AGAL030.848–00.081	N1	102.9	7.0	3.6	N2	94.4	7.5	9.2	–	–	–	–
25	AGAL030.893+00.139	N	106.7	6.2	8.3	P2	94.3	2.0	4.2	–	–	–	–
28	AGAL034.401+00.226	B1	57.5	11.6	19.1	B2	56.8	51.0	1.1	–	–	–	–
29	AGAL034.411+00.234	B1	57.9	10.7	14.3	B2	62.9	42.9	1.6	–	–	–	–
31	AGAL035.197–00.742	B1	34.5	9.0	27.1	B2	31.2	15.7	11.9	–	–	–	–
32	AGAL037.554+00.201	N	85.7	7.1	11.3	B	82.7	16.9	7.2	–	–	–	–
33	AGAL043.166+00.011	B1	–1.1	11.8	39.0	B2	13.2	17.3	24.0	B3	2.8	33.4	6.6
35	AGAL053.141+00.069	B1	23.3	9.2	20.6	B2	23.4	42.1	1.4	–	–	–	–
36	AGAL059.782+00.066	B1	22.2	8.1	24.1	B2	21.0	26.0	3.0	–	–	–	–
39	AGAL305.209+00.206	N	–44.6	6.1	15.7	B	–40.3	17.3	18.2	–	–	–	–
40	AGAL305.562+00.014	N	–38.8	6.7	25.1	B	–41.0	14.2	13.6	–	–	–	–
42	AGAL309.384–00.134	B	–50.6	11.8	13.2	–	–	–	–	–	–	–	–
44	AGAL313.576+00.324	B1	–47.9	9.3	10.0	B2	–40.4	17.0	4.5	–	–	–	–
45	AGAL316.641–00.087	N	–16.9	7.2	9.9	B	–22.2	26.9	2.7	–	–	–	–
46	AGAL317.867–00.151	B	–38.4	10.3	11.9	–	–	–	–	–	–	–	–
47	AGAL318.779–00.137	B1	–38.4	8.8	6.0	B2	–47.4	72.7	1.0	–	–	–	–
48	AGAL320.881–00.397	N	–45.5	6.4	11.7	–	–	–	–	–	–	–	–
49	AGAL326.661+00.519	N1	–39.7	3.8	31.6	N2	–38.0	7.2	13.7	–	–	–	–
50	AGAL326.987–00.032	B1	–57.9	9.1	7.0	B2	–57.6	14.4	2.5	–	–	–	–
52	AGAL327.393+00.199	B1	–89.3	9.4	10.5	B2	–86.3	86.0	1.0	–	–	–	–
54	AGAL329.066–00.307	B1	–41.9	11.1	7.2	B2	–47.6	15.0	3.1	–	–	–	–
55	AGAL330.879–00.367	B1	–64.7	17.5	26.7	B2	–78.6	32.2	7.0	–	–	–	–
57	AGAL331.709+00.582	B1	–67.2	9.9	15.3	B2	–64.7	24.2	9.2	–	–	–	–
58	AGAL332.094–00.421	B1	–57.6	12.2	16.9	B2	–56.4	29.9	3.2	–	–	–	–
61	AGAL333.284–00.387	B	–52.3	8.0	41.8	–	–	–	–	–	–	–	–
62	AGAL333.314+00.106	B1	–45.7	11.3	16.5	B2	–49.9	51.2	2.9	–	–	–	–
63	AGAL333.604–00.212	N	–46.8	7.2	25.2	B	–46.4	24.0	28.8	–	–	–	–
64	AGAL333.656+00.059	N	–83.9	6.5	10.7	–	–	–	–	–	–	–	–
65	AGAL335.789+00.174	B1	–50.0	10.2	13.6	B2	–49.7	24.2	9.4	–	–	–	–
66	AGAL336.958–00.224	B	–71.9	8.8	7.1	–	–	–	–	–	–	–	–
67	AGAL337.176–00.032	N	–70.4	4.5	5.9	B	–70.5	16.9	3.1	P2	–79.3	2.9	4.1
68	AGAL337.258–00.101	N	–69.1	6.2	6.1	–	–	–	–	–	–	–	–
73	AGAL338.066+00.044	N	–68.9	7.3	4.2	B	–63.9	34.6	1.8	P2	–39.0	9.7	3.8
74	AGAL338.786+00.476	N	–62.4	6.8	7.2	–	–	–	–	–	–	–	–
76	AGAL339.623–00.122	B1	–32.3	11.2	15.6	B2	–29.1	30.9	3.2	–	–	–	–
78	AGAL340.746–01.001	N	–29.4	7.4	15.5	B2	–23.8	13.7	3.5	–	–	–	–
79	AGAL340.784–00.097	B1	–102.4	9.7	10.0	B2	–102.6	35.5	1.0	–	–	–	–
81	AGAL342.484+00.182	B1	–42.4	8.2	7.5	B2	–47.5	15.3	4.0	–	–	–	–
82	AGAL343.128–00.062	B1	–29.2	15.7	25.1	B2	–29.3	35.4	10.5	–	–	–	–
87	AGAL345.504+00.347	N	–16.9	6.7	28.6	B	–16.6	20.7	15.1	–	–	–	–

Table A.2: continued.

ID	CSC Name	C <sub>1</sub>	V <sub>peak</sub> (km s <sup>-1</sup> )	FWHM (km s <sup>-1</sup> )	T <sub>peak</sub> (K)	C <sub>2</sub>	V <sub>peak</sub> (km s <sup>-1</sup> )	FWHM (km s <sup>-1</sup> )	T <sub>peak</sub> (K)	C <sub>3</sub>	V <sub>peak</sub> (km s <sup>-1</sup> )	FWHM (km s <sup>-1</sup> )	T <sub>peak</sub> (K)
88	AGAL345.718+00.817	B	-13.0	9.0	11.4	–	–	–	–	–	–	–	–
89	AGAL351.131+00.771	N	-5.6	5.0	15.3	–	–	–	–	–	–	–	–
91	AGAL351.244+00.669	B1	-3.3	9.3	47.8	B2	3.6	26.0	5.5	–	–	–	–
94	AGAL351.571+00.762	N	-3.6	6.0	8.1	–	–	–	–	–	–	–	–
96	AGAL351.774-00.537	B1	-1.7	17.4	28.4	B2	-10.7	53.3	7.2	–	–	–	–
97	AGAL353.066+00.452	N	-1.6	5.2	5.4	–	–	–	–	–	–	–	–
99	AGAL354.944-00.537	N	-5.9	5.4	5.9	–	–	–	–	–	–	–	–

**Notes.** The columns are as follows: (1)-(2) ID and CSC name of the source (given in Table A.1); (3), (7), (11) the classification of each fitted Gaussian component (C<sub>1</sub>, C<sub>2</sub> and C<sub>3</sub>), into narrow (N), broad (B) or secondary peaks (P2) as discussed in the main text; (4)-(6), (8)-(10), (12)-(14) the central velocity (V<sub>peak</sub>), full width at half maximum (FWHM) and peak temperature (T<sub>peak</sub>) is presented for each component.

Table A.3: Gaussian decomposition of the CO (6–5) profiles towards the TOP100 sample.

ID	CSC Name	C <sub>1</sub>	V <sub>peak</sub> (km s <sup>-1</sup> )	FWHM (km s <sup>-1</sup> )	T <sub>peak</sub> (K)	C <sub>2</sub>	V <sub>peak</sub> (km s <sup>-1</sup> )	FWHM (km s <sup>-1</sup> )	T <sub>peak</sub> (K)	C <sub>3</sub>	V <sub>peak</sub> (km s <sup>-1</sup> )	FWHM (km s <sup>-1</sup> )	T <sub>peak</sub> (K)
2	AGAL008.706-00.414	N	38.3	6.3	3.4	–	–	–	–	–	–	–	–
3	AGAL010.444-00.017	N	74.3	3.3	3.1	B	74.7	12.0	2.6	P2	65.4	2.0	1.7
4	AGAL010.472+00.027	N	66.0	7.1	72.7	B	69.0	14.9	13.3	–	–	–	–
5	AGAL010.624-00.384	B1	-2.4	11.4	108.1	B2	-2.5	24.1	7.8	–	–	–	–
6	AGAL012.804-00.199	B1	35.1	10.3	105.9	B2	39.8	18.5	28.4	–	–	–	–
7	AGAL013.178+00.059	B1	49.0	9.7	17.8	B2	59.6	26.0	0.8	–	–	–	–
8	AGAL013.658-00.599	N	48.2	5.5	12.2	B1	46.6	15.5	4.4	B2	42.1	62.3	1.4
10	AGAL014.194-00.194	N	39.8	5.3	13.6	B1	40.5	14.4	8.0	B2	35.8	29.1	1.8
11	AGAL014.492-00.139	N	40.1	5.6	8.7	B	40.1	23.5	1.5	–	–	–	–
12	AGAL014.632-00.577	B1	18.2	7.9	26.4	B2	18.4	32.6	1.3	–	–	–	–
13	AGAL015.029-00.669	N	20.9	6.9	75.3	B	18.6	10.9	60.3	–	–	–	–
14	AGAL018.606-00.074	N	45.8	4.4	15.0	B	45.6	10.4	4.8	–	–	–	–
15	AGAL018.734-00.226	N	40.1	6.4	12.9	B	40.1	26.6	3.2	–	–	–	–
16	AGAL018.888-00.474	B1	65.6	9.1	19.9	B2	69.4	20.7	3.1	–	–	–	–
17	AGAL019.882-00.534	N	45.3	6.5	18.5	B1	45.5	17.8	15.5	B3	64.1	70.9	1.8
18	AGAL022.376+00.447	N	52.5	3.1	11.6	B	53.8	10.4	4.1	–	–	–	–
19	AGAL023.206-00.377	B1	78.3	12.7	17.6	B2	77.8	37.3	3.5	–	–	–	–
20	AGAL024.629+00.172	B1	114.8	7.8	4.3	B2	120.5	40.1	0.5	–	–	–	–
21	AGAL028.564-00.236	N	86.1	5.6	4.6	B	87.6	16.1	1.6	–	–	–	–
22	AGAL028.861+00.066	B1	105.0	10.5	24.8	B2	102.0	32.0	6.4	–	–	–	–
23	AGAL030.818-00.056	N	97.5	6.6	35.9	B1	98.2	14.2	13.7	B2	100.3	52.5	2.4
24	AGAL030.848-00.081	N	95.5	5.5	5.1	B	96.5	12.5	7.5	–	–	–	–
25	AGAL030.893+00.139	N	106.8	5.8	7.0	P2	97.0	5.2	4.5	–	–	–	–
26	AGAL031.412+00.307	N	97.5	7.3	42.8	B	100.2	29.3	4.2	–	–	–	–
28	AGAL034.401+00.226	N	58.5	7.0	17.0	B1	58.0	12.1	26.1	B2	59.4	42.8	1.6
29	AGAL034.411+00.234	B1	57.9	10.1	19.6	B2	57.4	41.3	2.0	–	–	–	–
30	AGAL034.821+00.351	N	57.9	5.9	11.3	B	56.4	18.9	7.4	–	–	–	–
31	AGAL035.197-00.742	B1	34.3	9.5	46.2	B2	32.5	20.0	22.9	–	–	–	–
32	AGAL037.554+00.201	N	85.7	6.4	12.2	B	84.3	15.6	7.1	–	–	–	–
33	AGAL043.166+00.011	B1	-0.5	12.9	56.0	B2	15.2	13.5	32.3	B3	2.1	42.3	13.1
35	AGAL053.141+00.069	N	22.3	7.2	37.2	B	21.0	17.0	10.8	–	–	–	–
36	AGAL059.782+00.066	B1	22.8	8.4	37.2	B2	22.0	24.6	5.3	–	–	–	–
37	AGAL301.136-00.226	B1	-38.3	9.9	34.4	B2	-37.3	31.1	14.0	B3	-28.8	65.4	10.4
38	AGAL305.192-00.006	N	-33.7	7.5	22.4	B	-34.4	19.9	4.6	–	–	–	–
39	AGAL305.209+00.206	B1	-42.4	10.9	43.7	B2	-40.1	33.2	10.1	–	–	–	–
40	AGAL305.562+00.014	N	-38.9	5.7	38.7	B	-40.0	14.9	21.2	–	–	–	–
41	AGAL305.794-00.096	B	-41.7	9.2	4.6	–	–	–	–	–	–	–	–
42	AGAL309.384-00.134	B1	-51.0	8.6	18.3	B2	-51.0	22.3	3.0	–	–	–	–
43	AGAL310.014+00.387	B1	-42.6	10.1	13.9	B2	-46.8	35.0	3.0	–	–	–	–
44	AGAL313.576+00.324	N	-46.7	7.4	19.4	B	-43.5	27.7	4.2	–	–	–	–
45	AGAL316.641-00.087	B1	-16.7	9.1	5.4	B2	-21.5	28.3	3.1	–	–	–	–
46	AGAL317.867-00.151	B	-39.9	11.2	15.7	–	–	–	–	–	–	–	–
47	AGAL318.779-00.137	N	-40.0	5.4	7.7	B	-38.7	20.7	2.2	–	–	–	–
48	AGAL320.881-00.397	N	-45.7	4.6	8.9	B	-44.6	10.5	2.9	–	–	–	–

Table A.3: continued.

ID	CSC Name	C <sub>1</sub>	V <sub>peak</sub> (km s <sup>-1</sup> )	FWHM (km s <sup>-1</sup> )	T <sub>peak</sub> (K)	C <sub>2</sub>	V <sub>peak</sub> (km s <sup>-1</sup> )	FWHM (km s <sup>-1</sup> )	T <sub>peak</sub> (K)	C <sub>3</sub>	V <sub>peak</sub> (km s <sup>-1</sup> )	FWHM (km s <sup>-1</sup> )	T <sub>peak</sub> (K)
49	AGAL326.661+00.519	N	-39.4	3.3	57.6	B	-38.4	7.6	18.1	-	-	-	-
50	AGAL326.987-00.032	N	-58.2	5.9	9.9	B1	-55.2	16.3	3.6	B2	-54.1	56.4	0.6
51	AGAL327.119+00.509	N	-83.9	6.3	18.1	B	-83.4	20.5	2.9	-	-	-	-
52	AGAL327.393+00.199	B1	-88.9	8.2	14.8	B2	-90.7	27.7	1.5	-	-	-	-
53	AGAL329.029-00.206	B1	-44.2	10.5	20.9	B2	-49.7	17.0	6.5	B3	-64.1	62.7	0.6
54	AGAL329.066-00.307	B1	-42.2	8.0	12.6	B2	-43.7	17.7	3.3	-	-	-	-
55	AGAL330.879-00.367	B1	-60.3	10.0	42.7	B2	-68.8	13.0	23.3	B3	-73.2	38.6	11.3
56	AGAL330.954-00.182	B1	-92.5	9.8	50.3	B2	-93.6	26.7	29.1	-	-	-	-
57	AGAL331.709+00.582	N	-66.1	5.7	8.6	B1	-66.3	13.4	14.9	B3	-63.9	36.3	2.9
58	AGAL332.094-00.421	B1	-57.6	12.4	12.5	B2	-54.5	23.7	9.2	-	-	-	-
61	AGAL333.284-00.387	B	-51.1	8.0	57.9	-	-	-	-	-	-	-	-
62	AGAL333.314+00.106	N	-45.1	7.1	11.1	B1	-47.1	15.2	12.2	B2	-45.9	64.9	1.2
63	AGAL333.604-00.212	B1	-44.1	11.9	85.0	B2	-48.1	25.3	38.4	-	-	-	-
64	AGAL333.656+00.059	N	-84.6	6.4	9.0	B	-84.5	23.4	0.8	-	-	-	-
65	AGAL335.789+00.174	N	-50.4	6.1	20.1	B1	-49.9	19.6	14.9	B2	-55.9	68.3	0.8
66	AGAL336.958-00.224	N	-72.4	4.8	6.7	B	-73.1	29.7	2.3	-	-	-	-
67	AGAL337.176-00.032	N	-69.8	3.4	12.2	B	-72.0	13.8	4.5	P2	-79.4	3.1	4.5
68	AGAL337.258-00.101	B	-67.8	9.6	9.2	-	-	-	-	-	-	-	-
69	AGAL337.286+00.007	N	-106.0	7.4	3.6	P2	-73.9	3.8	1.5	-	-	-	-
70	AGAL337.406-00.402	N	-40.7	6.8	69.8	B1	-40.3	23.5	8.7	B2	-28.2	83.2	3.1
72	AGAL337.916-00.477	B1	-40.1	10.7	38.1	B1	-43.7	28.1	18.5	B2	-52.0	56.9	6.5
73	AGAL338.066+00.044	N	-69.3	4.9	4.5	B	-68.7	21.7	2.3	P2	-39.9	8.2	3.7
74	AGAL338.786+00.476	N	-63.8	7.1	6.0	-	-	-	-	-	-	-	-
75	AGAL338.926+00.554	N	-62.5	6.4	131.4	B1	-60.4	16.3	11.3	B2	-62.5	49.1	2.5
76	AGAL339.623-00.122	N	-32.9	6.2	14.1	B1	-31.9	18.0	12.7	B2	-25.6	58.6	1.8
77	AGAL340.374-00.391	B1	-44.5	10.7	5.3	B	-38.7	50.8	1.3	-	-	-	-
78	AGAL340.746-01.001	N	-29.3	6.9	18.3	B1	-23.8	13.4	2.7	B2	-15.3	49.0	1.0
79	AGAL340.784-00.097	N	-101.4	6.9	8.1	B	-101.0	18.3	2.6	-	-	-	-
80	AGAL341.217-00.212	N	-43.5	4.1	26.6	B1	-41.5	12.3	7.5	B2	-44.9	37.9	3.6
81	AGAL342.484+00.182	N	-42.2	5.9	8.4	B	-45.1	17.2	6.4	-	-	-	-
82	AGAL343.128-00.062	B1	-29.2	16.5	46.2	B2	-26.2	39.8	14.1	-	-	-	-
83	AGAL343.756-00.164	B1	-27.2	8.4	19.1	B2	-25.5	23.2	1.2	-	-	-	-
84	AGAL344.227-00.569	B1	-22.3	10.1	17.8	B2	-27.8	29.3	6.1	-	-	-	-
85	AGAL345.003-00.224	B1	-26.9	7.5	51.2	B2	-27.3	20.6	17.8	B3	-13.4	97.1	2.6
87	AGAL345.504+00.347	B1	-16.8	8.2	31.3	B2	-16.0	19.4	19.7	B3	-1.6	43.3	1.5
88	AGAL345.718+00.817	B	-12.2	7.8	14.4	-	-	-	-	-	-	-	-
89	AGAL351.131+00.771	N	-5.1	4.7	17.5	-	-	-	-	-	-	-	-
90	AGAL351.161+00.697	B1	-5.3	9.2	60.2	B2	-8.5	22.2	26.6	-	-	-	-
91	AGAL351.244+00.669	B1	-2.9	8.6	96.6	B2	0.6	25.4	13.4	B3	8.7	72.3	1.4
92	AGAL351.416+00.646	B1	-6.5	9.5	70.5	B2	-12.4	34.2	18.8	B3	-25.1	96.5	3.2
93	AGAL351.444+00.659	B1	-4.1	8.9	37.7	B2	-4.1	15.0	19.9	B3	-8.3	40.0	8.4
94	AGAL351.571+00.762	N	-4.1	3.5	8.2	-	-	-	-	-	-	-	-
95	AGAL351.581-00.352	B1	-95.4	10.7	23.9	B2	-97.2	29.2	10.2	B3	-131.9	70.0	0.6
96	AGAL351.774-00.537	B1	-1.3	10.6	36.0	B2	-0.8	26.3	22.9	B3	-10.2	61.3	14.9
97	AGAL353.066+00.452	B	-1.0	7.6	16.5	-	-	-	-	-	-	-	-
98	AGAL353.417-00.079	N	-55.6	2.7	1.9	B	-53.8	9.0	1.8	-	-	-	-
99	AGAL354.944-00.537	N	-5.7	2.6	13.1	B	-5.2	8.8	2.0	-	-	-	-

**Notes.** The columns are as follows: (1)-(2) ID and CSC name of the source (given in Table A.1); (3), (7), (11) the classification of each fitted Gaussian component (C<sub>1</sub>, C<sub>2</sub> and C<sub>3</sub>), into narrow (N), broad (B) or secondary peaks (P2) as discussed in the main text; (4)-(6), (8)-(10), (12)-(14) the central velocity (V<sub>peak</sub>), full width at half maximum (FWHM) and peak temperature (T<sub>peak</sub>) is presented for each component.

Table A.4: Gaussian decomposition of the CO (7–6) profiles towards the TOP100 sample.

ID	CSC Name	C <sub>1</sub>	V <sub>peak</sub> (km s <sup>-1</sup> )	FWHM (km s <sup>-1</sup> )	T <sub>peak</sub> (K)	C <sub>2</sub>	V <sub>peak</sub> (km s <sup>-1</sup> )	FWHM (km s <sup>-1</sup> )	T <sub>peak</sub> (K)	C <sub>3</sub>	V <sub>peak</sub> (km s <sup>-1</sup> )	FWHM (km s <sup>-1</sup> )	T <sub>peak</sub> (K)
1	AGAL008.684-00.367	B1	38.3	9.4	15.1	B2	50.2	27.1	1.8	-	-	-	-
2	AGAL008.706-00.414	N	39.8	6.8	2.4	-	-	-	-	-	-	-	-
3	AGAL010.444-00.017	N	75.0	7.0	3.8	P2	66.6	3.7	1.8	-	-	-	-
4	AGAL010.472+00.027	N	66.1	7.2	63.4	B	70.6	20.1	8.2	-	-	-	-

Table A.4: continued.

ID	CSC Name	C <sub>1</sub>	V <sub>peak</sub> (km s <sup>-1</sup> )	FWHM (km s <sup>-1</sup> )	T <sub>peak</sub> (K)	C <sub>2</sub>	V <sub>peak</sub> (km s <sup>-1</sup> )	FWHM (km s <sup>-1</sup> )	T <sub>peak</sub> (K)	C <sub>3</sub>	V <sub>peak</sub> (km s <sup>-1</sup> )	FWHM (km s <sup>-1</sup> )	T <sub>peak</sub> (K)
5	AGAL010.624–00.384	B1	–2.4	9.7	88.4	B2	–1.6	17.4	30.2	–	–	–	–
6	AGAL012.804–00.199	B1	35.0	10.0	107.1	B2	39.8	17.4	28.4	–	–	–	–
7	AGAL013.178+00.059	B	49.2	11.0	16.0	–	–	–	–	–	–	–	–
8	AGAL013.658–00.599	N	48.3	6.5	10.0	B	43.6	69.9	2.9	–	–	–	–
9	AGAL014.114–00.574	N	19.4	4.2	20.4	B	19.9	14.3	6.3	–	–	–	–
10	AGAL014.194–00.194	B1	40.1	7.7	11.1	B2	41.3	29.2	3.6	–	–	–	–
11	AGAL014.492–00.139	B	39.8	10.3	5.5	–	–	–	–	–	–	–	–
12	AGAL014.632–00.577	N	17.9	7.1	26.3	B	21.3	20.2	1.8	–	–	–	–
13	AGAL015.029–00.669	B1	20.7	7.7	104.6	B2	18.8	13.7	25.0	–	–	–	–
14	AGAL018.606–00.074	B	45.2	7.5	10.2	–	–	–	–	–	–	–	–
15	AGAL018.734–00.226	N	40.4	6.7	10.1	B	44.9	46.0	2.6	–	–	–	–
16	AGAL018.888–00.474	N	65.8	5.7	13.2	B	66.0	18.0	6.2	–	–	–	–
17	AGAL019.882–00.534	N	45.1	6.6	13.1	B1	45.0	17.2	14.9	B2	65.7	96.9	2.3
18	AGAL022.376+00.447	N	53.3	6.3	7.6	–	–	–	–	–	–	–	–
19	AGAL023.206–00.377	B1	78.0	11.6	18.4	B2	78.2	50.0	3.6	–	–	–	–
20	AGAL024.629+00.172	B	115.8	7.8	3.7	–	–	–	–	–	–	–	–
21	AGAL028.564–00.236	N	86.4	4.0	3.3	–	–	–	–	–	–	–	–
22	AGAL028.861+00.066	B1	104.6	12.2	21.5	B2	80.0	81.9	3.4	–	–	–	–
23	AGAL030.818–00.056	N	97.9	7.4	48.2	B	96.6	50.5	5.6	–	–	–	–
24	AGAL030.848–00.081	B	96.2	10.9	9.5	–	–	–	–	–	–	–	–
25	AGAL030.893+00.139	N	106.3	2.0	7.2	P2	95.0	3.5	3.9	–	–	–	–
26	AGAL031.412+00.307	B1	97.6	7.5	40.5	B2	97.4	85.6	2.7	–	–	–	–
27	AGAL034.258+00.154	B1	57.7	8.9	71.7	B2	63.8	37.4	8.7	–	–	–	–
28	AGAL034.401+00.226	B1	58.0	10.3	29.6	B2	63.5	64.3	2.0	–	–	–	–
29	AGAL034.411+00.234	B1	58.2	10.4	16.3	B2	61.9	65.6	2.3	–	–	–	–
30	AGAL034.821+00.351	N	57.7	6.9	11.4	B	59.2	28.2	5.0	–	–	–	–
31	AGAL035.197–00.742	B1	34.6	8.9	38.8	B2	32.8	20.1	19.6	–	–	–	–
32	AGAL037.554+00.201	B1	85.5	7.7	12.8	B2	88.0	52.3	3.1	–	–	–	–
33	AGAL043.166+00.011	B1	15.9	12.1	30.9	B2	0.2	14.1	49.8	B3	–1.9	70.9	6.5
35	AGAL053.141+00.069	N	22.4	6.3	30.5	B	21.1	16.0	11.8	–	–	–	–
36	AGAL059.782+00.066	B1	22.7	8.7	29.6	B2	21.6	28.0	4.0	–	–	–	–
37	AGAL301.136–00.226	B1	–38.4	9.5	37.8	B2	–36.8	32.7	14.8	B3	–22.9	70.3	7.8
38	AGAL305.192–00.006	B1	–33.9	7.9	15.2	B2	–34.1	24.5	3.0	–	–	–	–
39	AGAL305.209+00.206	B1	–42.5	10.7	45.0	B2	–37.5	43.1	6.8	–	–	–	–
40	AGAL305.562+00.014	N	–38.7	5.9	50.2	B	–42.7	17.8	11.3	–	–	–	–
41	AGAL305.794–00.096	B	–42.5	11.1	5.7	–	–	–	–	–	–	–	–
42	AGAL309.384–00.134	B	–51.3	10.4	17.4	–	–	–	–	–	–	–	–
43	AGAL310.014+00.387	B1	–42.7	8.7	15.5	B2	–43.1	35.1	4.7	–	–	–	–
44	AGAL313.576+00.324	N	–46.8	6.4	19.4	B	–43.0	25.2	3.4	–	–	–	–
45	AGAL316.641–00.087	B	–17.8	17.1	5.9	–	–	–	–	–	–	–	–
46	AGAL317.867–00.151	B	–39.7	8.2	17.3	–	–	–	–	–	–	–	–
47	AGAL318.779–00.137	B	–38.3	7.9	10.3	–	–	–	–	–	–	–	–
48	AGAL320.881–00.397	N	–45.4	4.9	8.6	–	–	–	–	–	–	–	–
49	AGAL326.661+00.519	N	–39.4	4.0	69.0	–	–	–	–	–	–	–	–
50	AGAL326.987–00.032	B	–57.4	8.1	12.1	–	–	–	–	–	–	–	–
51	AGAL327.119+00.509	B	–84.0	9.9	11.4	–	–	–	–	–	–	–	–
52	AGAL327.393+00.199	B	–88.9	9.4	14.8	–	–	–	–	–	–	–	–
53	AGAL329.029–00.206	N	–43.8	7.1	15.8	B	–46.4	16.2	11.0	–	–	–	–
54	AGAL329.066–00.307	N	–42.0	6.7	12.4	B	–47.5	29.0	3.1	–	–	–	–
55	AGAL330.879–00.367	B1	–61.3	12.7	40.6	B2	–69.5	22.2	19.3	B3	–78.8	88.3	3.6
56	AGAL330.954–00.182	B1	–92.4	10.0	51.6	B2	–94.1	26.8	24.4	–	–	–	–
57	AGAL331.709+00.582	B1	–65.9	8.9	11.6	B2	–66.5	29.4	5.5	–	–	–	–
58	AGAL332.094–00.421	B1	–57.4	7.6	19.4	B2	–55.2	26.4	9.9	–	–	–	–
61	AGAL333.284–00.387	B	–51.2	7.6	55.9	–	–	–	–	–	–	–	–
62	AGAL333.314+00.106	B1	–45.9	10.7	16.9	B2	–58.7	90.9	2.2	–	–	–	–
63	AGAL333.604–00.212	B1	–44.1	11.9	94.3	B2	–49.0	24.1	40.8	–	–	–	–
64	AGAL333.656+00.059	B	–85.7	9.9	5.5	–	–	–	–	–	–	–	–
65	AGAL335.789+00.174	N	–49.7	5.2	20.1	B1	–50.6	19.5	13.3	B2	–72.3	116.4	1.2
66	AGAL336.958–00.224	N	–71.7	7.3	6.3	–	–	–	–	–	–	–	–
67	AGAL337.176–00.032	B1	–68.6	8.2	11.2	B2	–66.7	32.7	2.4	P2	–79.2	4.7	5.2

Table A.4: continued.

ID	CSC Name	C <sub>1</sub>	V <sub>peak</sub> (km s <sup>-1</sup> )	FWHM (km s <sup>-1</sup> )	T <sub>peak</sub> (K)	C <sub>2</sub>	V <sub>peak</sub> (km s <sup>-1</sup> )	FWHM (km s <sup>-1</sup> )	T <sub>peak</sub> (K)	C <sub>3</sub>	V <sub>peak</sub> (km s <sup>-1</sup> )	FWHM (km s <sup>-1</sup> )	T <sub>peak</sub> (K)
68	AGAL337.258–00.101	B	-68.1	10.1	8.6	–	–	–	–	–	–	–	–
69	AGAL337.286+00.007	B	-105.6	8.3	3.0	–	–	–	–	–	–	–	–
70	AGAL337.406–00.402	N	-40.9	5.4	75.5	B	-40.5	16.2	13.2	B	-24.9	61.1	2.0
71	AGAL337.704–00.054	B1	-47.2	11.1	24.7	B2	-40.4	68.9	3.0	–	–	–	–
72	AGAL337.916–00.477	B1	-40.3	10.6	40.8	B2	-46.1	33.1	18.4	B3	-46.9	113.4	3.0
73	AGAL338.066+00.044	B	-69.9	13.3	3.3	P2	-13.5	10.5	2.8	–	–	–	–
74	AGAL338.786+00.476	B	-63.7	8.9	5.7	–	–	–	–	–	–	–	–
75	AGAL338.926+00.554	B1	-62.3	8.6	43.2	B2	-60.9	26.9	6.5	–	–	–	–
76	AGAL339.623–00.122	N	-33.8	7.0	14.3	B	-32.2	21.6	9.7	–	–	–	–
77	AGAL340.374–00.391	B1	-44.3	8.2	6.6	B2	-43.5	61.0	1.6	–	–	–	–
78	AGAL340.746–01.001	B1	-28.9	7.5	15.6	B2	-18.6	30.2	3.4	–	–	–	–
79	AGAL340.784–00.097	B	-101.6	10.1	8.0	–	–	–	–	–	–	–	–
80	AGAL341.217–00.212	N	-43.1	5.6	28.2	B	-46.2	68.9	3.7	–	–	–	–
81	AGAL342.484+00.182	B1	-42.4	9.6	9.6	B2	-40.8	67.9	2.3	–	–	–	–
82	AGAL343.128–00.062	B1	-29.1	18.4	47.8	B2	-23.3	52.3	8.2	–	–	–	–
83	AGAL343.756–00.164	B	-27.1	7.8	22.2	–	–	–	–	–	–	–	–
84	AGAL344.227–00.569	B1	-22.1	7.7	16.2	B2	-25.3	30.3	8.0	–	–	–	–
85	AGAL345.003–00.224	B1	-26.6	8.7	38.9	B2	-27.3	21.4	17.1	B3	-13.3	108.3	3.3
87	AGAL345.504+00.347	B1	-16.7	9.4	37.4	B2	-14.1	24.9	9.2	–	–	–	–
88	AGAL345.718+00.817	N	-11.5	5.5	15.3	–	–	–	–	–	–	–	–
89	AGAL351.131+00.771	N	-5.4	4.7	13.7	–	–	–	–	–	–	–	–
90	AGAL351.161+00.697	B1	-6.4	11.0	79.2	B2	-8.9	28.0	11.5	–	–	–	–
91	AGAL351.244+00.669	B1	-2.9	8.4	108.6	B2	0.8	25.7	13.7	B3	19.9	120.2	2.0
92	AGAL351.416+00.646	B1	-7.0	8.5	59.0	B2	-11.7	31.7	17.0	B3	-19.5	76.3	5.4
93	AGAL351.444+00.659	B1	-4.3	11.0	45.6	B2	-6.9	28.0	12.2	–	–	–	–
94	AGAL351.571+00.762	N	-4.2	4.4	11.9	–	–	–	–	–	–	–	–
95	AGAL351.581–00.352	B1	-96.0	14.6	18.4	B2	-101.1	58.1	4.4	–	–	–	–
96	AGAL351.774–00.537	B1	-1.6	16.4	40.8	B2	-6.1	57.8	20.2	–	–	–	–
97	AGAL353.066+00.452	N	-1.2	6.6	10.6	–	–	–	–	–	–	–	–
98	AGAL353.417–00.079	N	-55.4	5.1	6.1	–	–	–	–	–	–	–	–
99	AGAL354.944–00.537	N	-5.2	6.4	5.1	–	–	–	–	–	–	–	–

**Notes.** The columns are as follows: (1)-(2) ID and CSC name of the source (given in Table A.1); (3), (7), (11) the classification of each fitted Gaussian component (C<sub>1</sub>, C<sub>2</sub> and C<sub>3</sub>), into narrow (N), broad (B) or secondary peaks (P2) as discussed in the main text; (4)-(6), (8)-(10), (12)-(14) the central velocity (V<sub>peak</sub>), full width at half maximum (FWHM) and peak temperature (T<sub>peak</sub>) is presented for each component.

Table A.5: Extension of the CO (6–5) and the *Herschel*-PACS 70 μm emission towards the TOP100 clumps.

ID	CSC Name	CO (6–5)					PACS 70 μm				
		Δθ <sub>max</sub> (")	Δθ <sub>min</sub> (")	Δθ <sub>avg</sub> (")	Δs <sub>avg</sub> (pc)	σ <sub>s</sub> (pc)	Δθ <sub>max</sub> (")	Δθ <sub>min</sub> (")	Δθ <sub>avg</sub> (")	Δs <sub>avg</sub> (pc)	σ <sub>s</sub> (pc)
1	AGAL008.684–00.367	16.8	11.7	14.2	0.331	0.085	12.9	15.2	14.1	0.326	0.038
2	AGAL008.706–00.414	30.5	20.3	25.4	0.589	0.130	–	–	–	–	–
3	AGAL010.444–00.017	38.1	17.2	27.6	1.146	0.256	10.3	9.4	9.9	0.409	0.025
4	AGAL010.472+00.027	41.2	21.1	31.2	1.292	0.280	15.2	14.1	14.7	0.607	0.032
5	AGAL010.624–00.384	47.3	29.7	38.5	0.924	0.193	15.2	17.3	16.2	0.389	0.036
6	AGAL012.804–00.199	88.5	57.9	73.2	0.852	0.173	13.3	17.1	15.2	0.177	0.031
7	AGAL013.178+00.059	47.3	29.7	38.5	0.448	0.094	–	–	–	–	–
8	AGAL013.658–00.599	25.9	12.5	19.2	0.416	0.101	13.8	12.2	13.0	0.281	0.024
9	AGAL014.114–00.574	45.8	19.6	32.7	0.407	0.089	9.0	8.3	8.6	0.108	0.006
10	AGAL014.194–00.194	27.5	18.8	23.1	0.438	0.098	10.9	9.8	10.4	0.196	0.014
11	AGAL014.492–00.139	36.6	21.9	29.2	0.549	0.119	–	–	–	–	–
12	AGAL014.632–00.577	36.6	25.8	31.2	0.277	0.059	11.3	13.2	12.3	0.109	0.012
13	AGAL015.029–00.669	91.5	68.9	80.2	0.770	0.155	34.6	20.4	27.5	0.264	0.097
14	AGAL018.606–00.074	24.4	20.3	22.3	0.470	0.105	10.5	9.4	9.9	0.209	0.018
15	AGAL018.734–00.226	24.4	12.5	18.5	1.117	0.272	14.0	11.3	12.7	0.765	0.112
16	AGAL018.888–00.474	62.5	36.8	49.7	1.141	0.235	15.2	10.0	12.6	0.290	0.085
17	AGAL019.882–00.534	35.1	20.3	27.7	0.492	0.107	13.7	11.4	12.5	0.222	0.029
18	AGAL022.376+00.447	13.7	11.7	12.7	0.244	0.065	10.0	8.2	9.1	0.175	0.025
19	AGAL023.206–00.377	13.7	12.5	13.1	0.292	0.076	12.5	11.2	11.9	0.265	0.021



Table A.5: continued.

ID	CSC Name	CO (6–5)					PACS 70 $\mu$ m				
		$\Delta\theta_{\max}$ (")	$\Delta\theta_{\min}$ (")	$\Delta\theta_{\text{avg}}$ (")	$\Delta s_{\text{avg}}$ (pc)	$\sigma_s$ (pc)	$\Delta\theta_{\max}$ (")	$\Delta\theta_{\min}$ (")	$\Delta\theta_{\text{avg}}$ (")	$\Delta s_{\text{avg}}$ (pc)	$\sigma_s$ (pc)
20	AGAL024.629+00.172	13.7	12.5	13.1	0.491	0.128	10.0	8.8	9.4	0.352	0.033
21	AGAL028.564–00.236	38.1	27.4	32.8	0.865	0.183	–	–	–	–	–
22	AGAL028.861+00.066	27.5	15.7	21.6	0.775	0.178	14.5	12.1	13.3	0.478	0.059
23	AGAL030.818–00.056	51.9	30.5	41.2	0.979	0.204	14.6	13.2	13.9	0.330	0.024
24	AGAL030.848–00.081	91.5	64.2	77.8	1.849	0.374	–	–	–	–	–
25	AGAL030.893+00.139	38.1	20.3	29.2	0.694	0.151	–	–	–	–	–
26	AGAL031.412+00.307	19.8	18.8	19.3	0.458	0.105	15.1	13.7	14.4	0.343	0.024
27	AGAL034.258+00.154	41.2	29.7	35.5	0.268	0.056	26.5	20.1	23.3	0.176	0.034
28	AGAL034.401+00.226	51.9	24.3	38.1	0.288	0.061	13.9	12.7	13.3	0.101	0.006
29	AGAL034.411+00.234	19.8	18.0	18.9	0.143	0.033	12.7	11.4	12.0	0.091	0.007
30	AGAL034.821+00.351	27.5	14.1	20.8	0.157	0.037	13.0	11.9	12.5	0.094	0.006
31	AGAL035.197–00.742	88.5	31.3	59.9	0.636	0.132	15.2	14.1	14.7	0.156	0.008
32	AGAL037.554+00.201	18.3	12.5	15.4	0.501	0.125	12.3	11.1	11.7	0.382	0.027
33	AGAL043.166+00.011	61.0	29.0	45.0	2.423	0.505	22.5	13.2	17.8	0.961	0.354
34	AGAL049.489–00.389	114.5	43.1	78.8	2.066	0.440	18.9	15.9	17.4	0.457	0.055
35	AGAL053.141+00.069	61.0	18.8	39.9	0.309	0.067	13.6	12.4	13.0	0.101	0.006
36	AGAL059.782+00.066	62.5	21.9	42.2	0.442	0.094	15.3	11.9	13.6	0.142	0.026
37	AGAL301.136–00.226	18.3	12.5	15.4	0.329	0.082	18.7	17.1	17.9	0.381	0.024
38	AGAL305.192–00.006	35.1	25.8	30.4	0.561	0.120	12.2	9.9	11.1	0.204	0.029
39	AGAL305.209+00.206	45.8	23.5	34.7	0.638	0.136	10.7	12.6	11.7	0.215	0.024
40	AGAL305.562+00.014	48.8	26.6	37.7	0.695	0.146	15.2	13.6	14.4	0.265	0.021
41	AGAL305.794–00.096	77.8	29.0	53.4	0.983	0.205	–	–	–	–	–
42	AGAL309.384–00.134	38.1	19.6	28.8	0.746	0.163	8.2	11.6	9.9	0.256	0.062
43	AGAL310.014+00.387	30.5	26.6	28.5	0.500	0.107	13.0	12.6	12.8	0.224	0.005
44	AGAL313.576+00.324	18.3	14.1	16.2	0.297	0.072	11.0	12.2	11.6	0.212	0.015
45	AGAL316.641–00.087	19.8	12.5	16.1	0.093	0.023	12.3	10.3	11.3	0.065	0.008
46	AGAL317.867–00.151	41.2	19.6	30.4	0.435	0.095	8.2	11.2	9.7	0.139	0.031
47	AGAL318.779–00.137	25.9	15.7	20.8	0.280	0.065	–	–	–	–	–
48	AGAL320.881–00.397	38.1	34.4	36.2	1.753	0.366	–	–	–	–	–
49	AGAL326.661+00.519	44.2	33.7	39.0	0.343	0.071	13.0	11.7	12.4	0.109	0.008
50	AGAL326.987–00.032	33.6	19.6	26.6	0.509	0.112	10.3	9.1	9.7	0.186	0.016
51	AGAL327.119+00.509	36.6	25.0	30.8	0.823	0.176	11.5	12.4	11.9	0.319	0.017
52	AGAL327.393+00.199	29.0	21.1	25.0	0.719	0.158	12.8	11.3	12.1	0.346	0.032
53	AGAL329.029–00.206	50.3	19.6	35.0	1.946	0.423	21.1	12.4	16.7	0.932	0.345
54	AGAL329.066–00.307	35.1	26.6	30.8	1.732	0.369	14.5	8.2	11.4	0.637	0.249
55	AGAL330.879–00.367	25.9	21.9	23.9	0.482	0.106	16.7	15.1	15.9	0.320	0.024
56	AGAL330.954–00.182	29.0	22.7	25.9	1.168	0.254	19.3	20.1	19.7	0.890	0.024
57	AGAL331.709+00.582	21.4	19.6	20.5	1.046	0.237	11.7	12.5	12.1	0.619	0.029
58	AGAL332.094–00.421	22.9	20.3	21.6	0.377	0.085	13.2	11.6	12.4	0.217	0.020
59	AGAL332.826–00.549	29.0	21.1	25.0	0.437	0.096	29.4	20.1	24.7	0.431	0.115
60	AGAL333.134–00.431	45.8	34.4	40.1	0.700	0.145	22.7	17.3	20.0	0.349	0.066
61	AGAL333.284–00.387	86.9	61.0	73.9	1.291	0.261	21.9	12.4	17.2	0.299	0.118
62	AGAL333.314+00.106	16.8	15.7	16.2	0.283	0.068	13.4	11.9	12.6	0.221	0.018
63	AGAL333.604–00.212	73.2	53.2	63.2	1.103	0.224	24.7	17.9	21.3	0.372	0.085
64	AGAL333.656+00.059	12.2	11.0	11.6	0.297	0.082	–	–	–	–	–
65	AGAL335.789+00.174	29.0	23.5	26.2	0.467	0.101	15.9	13.0	14.4	0.257	0.036
66	AGAL336.958–00.224	12.2	11.0	11.6	0.612	0.168	9.5	8.7	9.1	0.482	0.031
67	AGAL337.176–00.032	41.2	20.3	30.8	1.641	0.357	9.1	12.4	10.7	0.572	0.125
68	AGAL337.258–00.101	18.3	14.1	16.2	0.864	0.210	11.0	10.1	10.5	0.562	0.034
69	AGAL337.286+00.007	33.6	14.9	24.2	1.109	0.256	–	–	–	–	–
70	AGAL337.406–00.402	15.3	14.1	14.7	0.232	0.058	17.1	15.9	16.5	0.261	0.013
71	AGAL337.704–00.054	24.4	21.9	23.1	1.376	0.304	15.6	10.4	13.0	0.772	0.220
72	AGAL337.916–00.477	30.5	22.7	26.6	0.413	0.090	17.0	16.7	16.8	0.261	0.004
73	AGAL338.066+00.044	13.7	12.5	13.1	0.298	0.078	–	–	–	–	–
74	AGAL338.786+00.476	33.6	32.1	32.8	0.715	0.151	–	–	–	–	–
75	AGAL338.926+00.554	61.0	26.6	43.8	0.934	0.196	12.7	15.6	14.2	0.302	0.044
76	AGAL339.623–00.122	35.1	21.1	28.1	0.410	0.089	12.9	11.3	12.1	0.177	0.017
77	AGAL340.374–00.391	22.9	15.7	19.3	0.336	0.078	–	–	–	–	–
78	AGAL340.746–01.001	36.6	25.0	30.8	0.412	0.088	11.9	10.5	11.2	0.150	0.014

Table A.5: continued.

ID	CSC Name	CO (6–5)					PACS 70 $\mu$ m				
		$\Delta\theta_{\max}$ (")	$\Delta\theta_{\min}$ (")	$\Delta\theta_{\text{avg}}$ (")	$\Delta s_{\text{avg}}$ (pc)	$\sigma_s$ (pc)	$\Delta\theta_{\max}$ (")	$\Delta\theta_{\min}$ (")	$\Delta\theta_{\text{avg}}$ (")	$\Delta s_{\text{avg}}$ (pc)	$\sigma_s$ (pc)
79	AGAL340.784–00.097	16.8	14.9	15.8	0.767	0.186	11.2	11.5	11.4	0.550	0.013
80	AGAL341.217–00.212	18.3	14.9	16.6	0.295	0.071	17.3	17.3	17.3	0.307	0.000
81	AGAL342.484+00.182	35.1	22.7	28.9	1.758	0.379	12.8	10.8	11.8	0.718	0.082
82	AGAL343.128–00.062	42.7	18.0	30.4	0.447	0.099	18.4	16.0	17.2	0.253	0.025
83	AGAL343.756–00.164	29.0	20.3	24.6	0.347	0.076	12.6	12.0	12.3	0.173	0.006
84	AGAL344.227–00.569	27.5	13.3	20.4	0.249	0.059	13.8	11.9	12.8	0.157	0.017
85	AGAL345.003–00.224	39.7	18.0	28.9	0.422	0.093	16.7	15.2	16.0	0.234	0.016
86	AGAL345.488+00.314	61.0	43.8	52.4	0.564	0.115	18.5	16.9	17.7	0.190	0.012
87	AGAL345.504+00.347	68.6	37.6	53.1	0.579	0.119	14.9	14.0	14.4	0.158	0.007
88	AGAL345.718+00.817	38.1	27.4	32.8	0.248	0.052	14.6	17.6	16.1	0.122	0.016
89	AGAL351.131+00.771	91.5	86.1	88.8	0.783	0.158	–	–	–	–	–
90	AGAL351.161+00.697	42.7	34.4	38.6	0.340	0.071	25.1	18.1	21.6	0.191	0.044
91	AGAL351.244+00.669	53.4	35.2	44.3	0.391	0.081	33.3	18.3	25.8	0.227	0.094
92	AGAL351.416+00.646	48.8	25.0	36.9	0.240	0.051	23.0	20.9	22.0	0.143	0.010
93	AGAL351.444+00.659	73.2	47.7	60.4	0.393	0.080	17.3	12.6	15.0	0.097	0.022
94	AGAL351.571+00.762	53.4	27.4	40.4	0.262	0.055	–	–	–	–	–
95	AGAL351.581–00.352	13.7	13.3	13.5	0.446	0.114	14.2	13.2	13.7	0.452	0.021
96	AGAL351.774–00.537	33.6	15.7	24.6	0.119	0.027	21.8	20.0	20.9	0.101	0.006
97	AGAL353.066+00.452	83.9	23.5	53.7	0.224	0.047	–	–	–	–	–
98	AGAL353.417–00.079	–	–	–	–	–	–	–	–	–	–
99	AGAL354.944–00.537	22.9	14.9	18.9	0.175	0.041	–	–	–	–	–

**Notes.** The extension of the CO emission is measured from the 50% peak contour on the maps presented in Appendix B. The columns are as follows: (1) ID of the source; (2) the CSC name of the ATLASGAL clump; (3) the maximum elongation of the CO emission (in arcseconds); (4) the minimum elongation of the CO emission (in arcseconds); (5) the average size of the CO emission (in arcseconds); (6) the linear size of the CO emission (in parsecs), considering the average between the data presented in columns (3)-(4) and taking into account the distance of the source from Table A.1; (7) error of the linear extent of the CO emission, considering an uncertainty of 1.5" on the angular sizes presented in columns (3)-(4); (8)-(12) same as columns (3)-(7) but for the extension of the *Herschel*-PACS 70  $\mu$ m emission towards the 70  $\mu$ m-bright clumps. Columns (8) and (9) are extracted from Molinari et al. (2016).

Table A.6: Integrated properties of the CO emission profiles convolved to 13''4.

ID	CSC Name	CO(4-3)						CO(6-5)						CO(7-6)					
		rms	FWZP	$S_{\text{int}}$	$L_{\text{CO}}$	$\sigma_L$	*	rms	FWZP	$S_{\text{int}}$	$L_{\text{CO}}$	$\sigma_L$	*	rms	FWZP	$S_{\text{int}}$	$L_{\text{CO}}$	$\sigma_L$	*
1	AGAL008.684-00.367	0.16	32	79.30	17.38	6.02	*	0.23	38	69.86	15.26	5.29	*	1.28	24	71.81	15.69	5.43	*
2	AGAL008.706-00.414	0.12	18	37.48	8.21	2.85		0.18	20	12.89	2.82	0.98		0.82	10	7.88	1.72	0.60	
3	AGAL010.444-00.017	0.22	28	43.70	30.65	10.62		0.16	26	24.39	17.05	5.91		0.37	24	16.95	11.85	4.10	
4	AGAL010.472+00.027	0.28	42	228.67	160.37	55.55	*	0.43	44	197.14	137.81	47.74	*	0.91	32	170.60	119.26	41.31	*
5	AGAL010.624-00.384	0.19	44	535.01	125.76	43.57	*	0.15	60	458.13	107.34	37.18	*	0.87	38	421.05	98.65	34.17	*
6	AGAL012.804-00.199	0.15	52	452.52	25.01	8.66	*	0.15	60	529.02	29.14	10.09	*	0.43	46	532.39	29.32	10.16	*
7	AGAL013.178+00.059	0.13	66	134.91	7.45	2.58		0.22	40	93.44	5.15	1.78		0.90	24	92.03	5.07	1.76	
8	AGAL013.658-00.599	0.15	94	151.85	29.11	10.08	*	0.16	98	109.50	20.92	7.25	*	0.92	80	120.92	23.10	8.00	*
9	AGAL014.114-00.574	0.14	40	46.68	2.96	1.02	*	0.12	38	59.85	3.78	1.31	*	0.40	24	73.35	4.63	1.60	*
10	AGAL014.194-00.194	0.17	48	189.30	27.62	9.57		0.14	50	113.51	16.51	5.72		0.52	40	90.43	13.15	4.56	
11	AGAL014.492-00.139	0.19	44	64.86	9.32	3.23	*	0.18	28	29.37	4.21	1.46	*	1.09	10	17.26	2.47	0.86	*
12	AGAL014.632-00.577	0.17	44	110.21	3.54	1.23	*	0.19	40	96.73	3.10	1.07	*	0.40	26	93.95	3.01	1.04	*
13	AGAL015.029-00.669	0.17	36	564.08	21.22	7.35	*	0.21	38	580.80	21.77	7.54	*	1.14	26	588.89	22.08	7.65	*
14	AGAL018.606-00.074	0.16	22	65.14	93.93	32.54	*	0.10	28	45.94	8.24	2.85	*	0.41	18	35.66	6.39	2.21	*
15	AGAL018.734-00.226	0.19	48	99.23	148.27	51.36		0.17	50	81.83	121.87	42.22		0.86	28	60.64	90.32	31.29	
16	AGAL018.888-00.474	0.17	38	188.78	40.69	14.10		0.20	52	128.67	27.64	9.58		1.05	22	77.99	16.76	5.80	
17	AGAL019.882-00.534	0.19	88	389.08	50.00	17.32		0.50	94	267.32	34.24	11.86		0.64	84	229.71	29.42	10.19	
18	AGAL022.376+00.447	0.14	62	84.15	12.66	4.39	*	0.28	22	28.50	4.27	1.48	*	1.24	14	21.57	3.23	1.12	*
19	AGAL023.206-00.377	0.20	98	253.96	51.33	17.78	*	0.11	82	162.87	32.81	11.37	*	0.37	88	202.84	40.87	14.16	*
20	AGAL024.629+00.172	0.29	26	41.95	23.99	8.31	*	0.21	24	17.99	10.25	3.55	*	0.91	10	11.49	6.55	2.27	*
21	AGAL028.564-00.236	0.25	18	43.03	12.26	4.25	*	0.22	28	21.99	6.24	2.16	*	1.15	4	4.35	1.23	0.43	*
22	AGAL028.861+00.066	0.37	42	206.51	108.78	37.68	*	0.44	64	230.64	121.10	41.95	*	1.27	50	205.30	107.79	37.34	*
23	AGAL030.818-00.056	0.27	48	207.05	47.69	16.52	*	0.22	108	185.22	42.53	14.73	*	0.90	66	209.78	48.17	16.69	*
24	AGAL030.848-00.081	0.14	24	99.20	22.85	7.92	*	0.21	32	60.99	14.00	4.85	*	0.99	22	45.63	10.48	3.63	*
25	AGAL030.893+00.139	0.20	22	65.85	15.17	5.25		0.21	28	31.09	7.14	2.47		1.45	6	7.86	1.80	0.63	
26	AGAL031.412+00.307	0.32	44	118.49	27.29	9.45	*	0.24	66	154.61	35.50	12.30	*	0.37	54	166.62	38.25	13.25	*
27	AGAL034.258+00.154	0.47	58	267.05	6.23	2.16	*	0.52	106	371.07	8.64	2.99	*	0.47	80	383.48	8.92	3.09	*
28	AGAL034.401+00.226	0.14	62	227.22	5.30	1.84	*	0.13	94	217.43	5.06	1.75	*	0.41	50	183.55	4.27	1.48	*
29	AGAL034.411+00.234	0.18	92	210.08	4.90	1.70	*	0.28	86	136.45	3.18	1.10	*	1.24	24	99.08	2.31	0.80	*
30	AGAL034.821+00.351	0.18	104	156.90	3.66	1.27	*	0.19	50	101.50	2.36	0.82	*	1.34	22	77.53	1.80	0.63	*
31	AGAL035.197-00.742	0.26	42	269.51	12.40	4.30	*	0.09	76	348.76	16.00	5.54	*	0.34	46	295.51	13.55	4.69	*
32	AGAL037.554+00.201	0.15	44	142.11	61.38	21.26	*	0.26	38	81.59	35.13	12.17	*	1.56	26	70.58	30.39	10.53	*
33	AGAL043.166+00.011	0.52	66	1128.22	1335.97	462.80	*	0.25	132	904.50	1067.60	369.83		1.59	84	771.20	910.26	315.32	
34	AGAL049.489-00.389	0.63	58	542.23	152.25	52.74	*	0.39	82	264.61	74.06	25.65	*	0.91	70	327.19	91.57	31.72	*
35	AGAL053.141+00.069	0.15	76	211.85	5.20	1.80	*	0.14	72	179.15	4.39	1.52	*	0.35	38	159.77	3.91	1.35	*
36	AGAL059.782+00.066	0.24	56	246.98	11.05	3.83	*	0.12	66	204.38	9.12	3.16	*	0.43	40	170.32	7.60	2.63	*
37	AGAL301.136-00.226	0.34	134	730.69	135.71	47.01		0.88	130	705.32	130.58	45.23	*	1.62	126	780.76	144.54	50.07	
38	AGAL305.192-00.006	1.57	12	50.73	7.03	2.43		0.66	30	115.42	15.94	5.52		1.06	26	95.41	13.18	4.56	
39	AGAL305.209+00.206	1.60	36	433.43	60.04	20.80	*	0.22	96	403.76	55.75	19.31	*	0.83	70	396.50	54.75	18.97	*
40	AGAL305.562+00.014	0.40	32	376.91	52.21	18.09	*	0.23	38	271.66	37.51	12.99	*	1.65	26	248.49	34.31	11.89	*
41	AGAL305.794-00.096	0.34	22	13.80	1.91	0.66	*	0.22	24	21.01	2.90	1.00	*	1.62	16	34.13	4.71	1.63	*
42	AGAL309.384-00.134	0.53	26	133.61	36.55	12.66	*	0.21	44	95.86	26.14	9.05	*	1.58	26	99.76	27.20	9.42	*
43	AGAL310.014+00.387	0.45	48	182.21	22.78	7.89	*	0.21	74	120.32	14.99	5.19	*	1.27	30	104.86	13.07	4.53	*

Table A.6: continued.

ID	CSC Name	CO(4-3)					CO(6-5)					CO(7-6)							
		rms	FWZP	$S_{\text{int}}$	$L_{\text{CO}}$	$\sigma_{\text{L}}$	rms	FWZP	$S_{\text{int}}$	$L_{\text{CO}}$	$\sigma_{\text{L}}$	rms	FWZP	$S_{\text{int}}$	$L_{\text{CO}}$	$\sigma_{\text{L}}$			
44	AGAL313.576+00.324	0.35	42	174.54	23.93	8.29	*	0.21	60	131.00	17.90	6.20	*	1.18	28	104.31	14.25	4.94	*
45	AGAL316.641-00.087	0.35	54	122.67	1.67	0.58	*	0.22	40	64.08	0.87	0.30	*	1.42	30	55.15	0.75	0.26	*
46	AGAL317.867-00.151	0.35	22	110.70	9.24	3.20	*	0.23	42	77.81	6.48	2.24	*	1.49	20	73.94	6.15	2.13	*
47	AGAL318.779-00.137	0.33	36	70.07	5.19	1.80	*	0.21	30	39.33	2.91	1.01	*	1.18	16	43.92	3.25	1.12	*
48	AGAL320.881-00.397	0.43	28	90.61	86.40	29.93	*	0.16	26	36.39	34.59	14.26	*	0.91	10	20.54	19.53	8.05	*
49	AGAL326.661+00.519	0.36	100	334.51	10.63	3.68	*	0.17	24	169.20	5.36	2.21	*	0.95	18	151.69	4.80	1.98	*
50	AGAL326.987-00.032	0.28	28	61.97	9.28	3.21	*	0.18	54	63.15	9.42	3.26	*	0.79	20	45.92	6.85	2.37	*
51	AGAL327.119+00.509	0.24	42	90.43	26.34	9.12	*	0.24	38	69.34	20.13	8.30	*	1.00	22	49.12	14.26	5.88	*
52	AGAL327.393+00.199	0.32	54	140.73	47.32	16.39	*	0.14	54	84.02	28.16	9.75	*	0.77	22	67.46	22.61	7.83	*
53	AGAL329.029-00.206	0.25	42	179.16	226.91	78.61	*	0.23	94	172.95	218.34	75.64	*	0.55	38	145.34	183.49	63.56	*
54	AGAL329.066-00.307	0.24	42	111.89	143.95	49.86	*	0.17	46	86.23	110.58	63.52	*	0.77	24	65.68	84.22	48.38	*
55	AGAL330.879-00.367	0.38	76	716.58	118.97	41.21	*	0.33	110	570.27	94.37	32.69	*	0.66	92	583.59	96.58	33.45	*
56	AGAL330.954-00.182	0.57	54	519.36	432.79	149.92	*	0.22	102	487.98	405.33	140.41	*	0.43	70	462.96	384.55	133.21	*
57	AGAL331.709+00.582	0.44	48	275.53	293.09	101.53	*	0.16	76	163.27	173.12	59.97	*	0.85	40	125.29	132.84	46.02	*
58	AGAL332.094-00.421	0.38	56	257.43	32.01	11.09	*	0.18	68	183.51	22.74	7.88	*	0.76	44	185.02	22.93	7.94	*
59	AGAL332.826-00.549	0.46	48	416.12	51.74	17.92	*	0.26	94	400.36	49.62	17.19	*	0.55	76	438.98	54.40	18.85	*
60	AGAL333.134-00.431	0.47	52	711.47	88.46	30.64	*	0.15	68	686.75	85.11	29.48	*	0.79	50	738.38	91.51	31.70	*
61	AGAL333.284-00.387	0.29	28	250.92	31.20	10.81	*	0.19	76	208.57	25.85	8.95	*	0.76	30	193.79	24.02	8.32	*
62	AGAL333.314+00.106	0.37	82	318.10	39.55	13.70	*	0.18	88	156.50	19.40	6.72	*	0.83	32	112.52	13.94	4.83	*
63	AGAL333.604-00.212	0.37	52	892.79	111.00	38.45	*	0.18	68	1018.59	126.23	43.73	*	0.79	50	1109.47	137.50	47.63	*
64	AGAL333.656+00.059	0.29	26	80.47	21.60	7.48	*	0.15	28	37.24	9.96	3.45	*	0.87	30	31.73	8.49	2.94	*
65	AGAL335.789+00.174	0.28	54	350.01	45.23	15.67	*	0.15	94	206.53	26.60	9.21	*	0.82	46	189.92	24.46	8.47	*
66	AGAL336.958-00.224	0.35	40	86.22	98.45	34.10	*	0.23	60	50.64	57.63	19.97	*	0.86	22	28.95	32.95	11.42	*
67	AGAL337.176-00.032	0.37	34	97.82	113.55	39.34	*	0.18	30	62.38	72.18	25.00	*	0.70	32	61.29	70.92	24.57	*
68	AGAL337.258-00.101	0.51	20	39.65	8.08	2.80	*	0.20	30	46.90	54.26	18.80	*	0.93	26	44.80	51.84	17.96	*
69	AGAL337.286+00.007	0.38	32	40.76	34.84	12.07	*	0.24	24	16.26	13.85	4.80	*	0.97	12	9.80	8.35	2.89	*
70	AGAL337.406-00.402	0.58	56	243.43	24.82	8.60	*	0.58	116	309.66	31.47	10.90	*	1.31	66	256.30	26.05	9.02	*
71	AGAL337.704-00.054	0.43	32	101.60	146.50	50.75	*	0.27	60	167.49	240.73	83.39	*	0.97	36	168.65	242.41	83.97	*
72	AGAL337.916-00.477	0.97	140	897.61	88.18	30.55	*	0.42	110	638.22	62.49	21.65	*	0.70	88	607.40	59.48	20.60	*
73	AGAL338.066+00.044	0.44	58	124.04	26.18	9.07	*	0.22	40	35.35	7.44	2.58	*	1.15	12	15.34	3.23	1.12	*
74	AGAL338.786+00.476	0.33	18	50.57	9.78	3.39	*	0.16	20	18.99	3.66	1.27	*	0.84	14	17.82	3.43	1.19	*
75	AGAL338.926+00.554	0.49	58	244.95	45.50	15.76	*	0.20	86	244.47	45.26	15.68	*	1.00	50	242.78	44.95	15.57	*
76	AGAL339.623-00.122	0.45	62	242.43	21.07	7.30	*	0.25	78	197.35	17.10	5.92	*	0.89	42	147.88	12.81	4.44	*
77	AGAL340.374-00.391	0.35	48	63.05	7.84	2.72	*	0.20	56	45.55	5.64	1.96	*	0.94	22	40.20	4.98	1.73	*
78	AGAL340.746-01.001	0.29	32	164.06	11.99	4.15	*	0.16	68	97.74	7.12	2.47	*	1.22	22	71.16	5.18	1.80	*
79	AGAL340.784-00.097	0.35	40	114.61	109.73	38.01	*	0.17	42	47.41	45.25	15.67	*	0.74	24	38.09	36.35	12.59	*
80	AGAL341.217-00.212	0.36	68	176.05	22.75	7.88	*	0.17	86	160.76	20.71	7.17	*	0.91	58	159.15	20.50	7.10	*
81	AGAL342.484+00.182	0.43	34	136.93	206.90	71.67	*	0.14	54	81.07	122.10	70.14	*	0.70	30	64.75	97.53	56.02	*
82	AGAL343.128-00.062	0.37	82	680.59	60.34	20.90	*	0.24	104	571.99	50.55	17.51	*	1.20	76	552.46	48.82	16.91	*
83	AGAL343.756-00.164	0.51	34	99.60	8.04	2.78	*	0.19	42	77.30	6.22	2.15	*	1.10	20	91.39	7.35	2.55	*
84	AGAL344.227-00.569	0.52	104	321.68	19.60	6.79	*	0.27	96	164.03	9.96	3.45	*	0.91	40	137.89	8.37	2.90	*
85	AGAL345.003-00.224	0.55	58	236.55	20.70	7.17	*	0.94	108	381.10	33.24	11.51	*	1.27	96	454.00	39.59	13.72	*
86	AGAL345.488+00.314	0.34	28	278.89	13.19	4.57	*	0.24	56	232.56	10.96	3.80	*	1.13	34	232.16	10.94	3.79	*

Table A.6: continued.

ID	CSC Name	CO(4–3)					CO(6–5)					CO(7–6)				
		rms	FWZP	$S_{\text{int}}$	$L_{\text{CO}}$	$\sigma_{\text{L}}$	rms	FWZP	$S_{\text{int}}$	$L_{\text{CO}}$	$\sigma_{\text{L}}$	rms	FWZP	$S_{\text{int}}$	$L_{\text{CO}}$	$\sigma_{\text{L}}$
87	AGAL345.504+00.347	0.42	52	388.73	18.88	6.54 *	0.31	72	297.81	14.42	4.99 *	1.03	40	251.73	12.19	4.22 *
88	AGAL345.718+00.817	0.37	24	77.99	1.82	0.63 *	0.20	24	50.60	1.18	0.41 *	0.96	12	34.86	0.81	0.28 *
89	AGAL351.131+00.771	0.31	12	71.39	2.27	0.79 *	0.17	16	37.63	1.19	0.41 *	0.91	12	27.49	0.87	0.30 *
90	AGAL351.161+00.697	0.38	70	567.62	18.04	6.25 *	0.17	84	461.74	14.63	5.07 *	0.62	64	468.44	14.84	5.14 *
91	AGAL351.244+00.669	0.34	50	544.55	17.30	5.99 *	0.22	146	604.24	19.14	6.63 *	0.81	66	641.90	20.33	7.04 *
92	AGAL351.416+00.646	1.02	72	785.21	13.53	4.69 *	0.99	130	699.69	12.01	4.16 *	0.93	142	706.14	12.12	4.20 *
93	AGAL351.444+00.659	0.55	56	418.17	7.20	2.50 *	0.20	94	371.22	6.37	2.21 *	1.25	66	408.63	7.02	2.43 *
94	AGAL351.571+00.762	0.41	18	52.86	0.91	0.32 *	0.30	14	16.09	0.28	0.10 *	2.85	12	25.21	0.43	0.15 *
95	AGAL351.581–00.352	0.55	60	144.40	64.24	22.25 *	0.35	84	228.92	101.52	35.17 *	1.07	54	206.39	91.53	31.71 *
96	AGAL351.774–00.537	0.85	100	740.71	7.11	2.46	0.88	162	816.24	7.81	2.70	1.37	96	777.98	7.44	2.58
97	AGAL353.066+00.452	0.58	10	29.88	0.21	0.07 *	0.19	26	63.88	0.45	0.16 *	1.39	10	28.05	0.20	0.07 *
98	AGAL353.417–00.079	0.63	24	42.10	14.83	5.14 *	0.22	18	11.63	4.08	1.42 *	1.84	10	16.82	5.91	2.05 *
99	AGAL354.944–00.537	0.62	12	36.75	1.29	0.45	0.23	22	18.97	0.66	0.23	1.42	8	10.72	0.37	0.13

**Notes.** The columns are as follows: (1)-(2) ID and CSC name of the source; (3) rms of the CO(4–3) data (in K), (4) the full width at zero power (FWZP, in  $\text{km s}^{-1}$ ); (5) integrated intensity of the line ( $S_{\text{int}}$ , in  $\text{K km s}^{-1}$ ); (6)-(7) the line luminosity and its associated uncertainty ( $L_{\text{CO}}$  and  $\sigma_{\text{L}}$ , in  $\text{K km s}^{-1} \text{pc}^2$ ) of the CO(4–3) spectra; (8) an asterisk mark indicates if the spectrum is contaminated by a self-absorption feature; the same properties computed for the CO(6–5) and CO(7–6) data are presented in columns (9)-(14) and (15)-(20), respectively.

Table A.7: Excitation temperature derived from the CO (6–5) spectra convolved to 13'4.

ID	CSC Name	$T_{\text{ex}}$	$\sigma_T$	$T_{\text{ex,gauss}}$	$\sigma_{T+}$	$\sigma_{T-}$	
1	AGAL008.684–00.367	28.0	0.3	43.2	5.9	5.2	*
2	AGAL008.706–00.414	14.2	0.3	13.9	0.3	0.3	
3	AGAL010.444–00.017	17.5	0.2	39.9	21.2	13.9	
4	AGAL010.472+00.027	52.3	0.4	97.0	0.6	0.6	
5	AGAL010.624–00.384	84.9	0.2	131.5	27.9	28.0	
6	AGAL012.804–00.199	97.1	0.2	143.0	11.5	12.4	
7	AGAL013.178+00.059	31.0	0.2	32.1	7.4	7.7	
8	AGAL013.658–00.599	29.7	0.2	30.8	18.6	16.2	
9	AGAL014.114–00.574	24.4	0.1	35.3	4.2	3.8	*
10	AGAL014.194–00.194	34.0	0.2	37.1	17.0	18.6	
11	AGAL014.492–00.139	20.5	0.2	22.8	6.1	6.8	
12	AGAL014.632–00.577	38.1	0.2	41.6	10.9	11.3	
13	AGAL015.029–00.669	146.9	0.2	67.2	41.2	25.5	
14	AGAL018.606–00.074	26.1	0.1	33.8	6.1	6.3	
15	AGAL018.734–00.226	29.4	0.2	29.2	2.7	2.8	
16	AGAL018.888–00.474	36.8	0.2	36.8	6.6	6.8	
17	AGAL019.882–00.534	49.7	0.5	50.0	2.8	2.8	
18	AGAL022.376+00.447	20.4	0.4	29.0	13.1	15.2	
19	AGAL023.206–00.377	32.4	0.1	34.9	0.5	0.5	
20	AGAL024.629+00.172	15.8	0.3	15.8	7.8	11.3	
21	AGAL028.564–00.236	15.3	0.3	17.7	4.8	5.8	
22	AGAL028.861+00.066	46.1	0.5	45.4	10.7	11.0	
23	AGAL030.818–00.056	44.1	0.2	66.7	43.0	45.2	
24	AGAL030.848–00.081	25.8	0.2	30.4	14.9	10.0	
25	AGAL030.893+00.139	18.8	0.3	18.5	6.8	9.1	
26	AGAL031.412+00.307	42.9	0.2	61.5	10.4	10.5	
27	AGAL034.258+00.154	87.4	0.5	59.9	9.8	8.4	*
28	AGAL034.401+00.226	52.5	0.1	59.5	47.8	23.8	
29	AGAL034.411+00.234	34.0	0.3	35.7	1.0	1.0	
30	AGAL034.821+00.351	29.3	0.2	32.4	2.2	2.2	
31	AGAL035.197–00.742	65.3	0.1	84.1	0.1	0.1	
32	AGAL037.554+00.201	28.3	0.3	32.8	3.4	3.5	
33	AGAL043.166+00.011	84.9	0.3	135.3	98.8	57.1	
34	AGAL049.489–00.389	58.3	0.4	56.3	8.9	7.7	*
35	AGAL053.141+00.069	49.2	0.1	61.7	7.0	7.0	
36	AGAL059.782+00.066	51.7	0.1	57.4	0.4	0.4	
37	AGAL301.136–00.226	59.7	0.9	73.6	0.1	0.1	
38	AGAL305.192–00.006	33.5	0.7	40.6	23.9	26.9	
39	AGAL305.209+00.206	69.7	0.2	68.9	2.2	2.2	
40	AGAL305.562+00.014	74.5	0.2	74.8	2.9	3.0	
41	AGAL305.794–00.096	15.9	0.3	15.5	1.0	1.0	
42	AGAL309.384–00.134	32.1	0.2	35.1	5.8	5.9	
43	AGAL310.014+00.387	30.4	0.2	30.0	2.4	2.4	
44	AGAL313.576+00.324	35.5	0.2	37.7	3.7	3.8	
45	AGAL316.641–00.087	21.0	0.3	20.4	3.0	3.3	
46	AGAL317.867–00.151	28.2	0.3	29.2	0.4	0.4	
47	AGAL318.779–00.137	20.6	0.3	22.3	4.9	5.3	
48	AGAL320.881–00.397	24.0	0.2	24.5	4.5	4.8	
49	AGAL326.661+00.519	89.7	0.2	89.7	13.6	13.7	
50	AGAL326.987–00.032	23.8	0.2	27.0	14.4	19.1	
51	AGAL327.119+00.509	28.2	0.3	33.8	6.1	6.3	
52	AGAL327.393+00.199	28.8	0.2	29.9	4.9	5.1	
53	AGAL329.029–00.206	36.0	0.3	40.3	7.8	7.9	
54	AGAL329.066–00.307	28.8	0.2	29.5	3.9	4.0	
55	AGAL330.879–00.367	64.9	0.3	75.0	0.5	0.5	
56	AGAL330.954–00.182	74.8	0.2	94.9	17.0	17.1	
57	AGAL331.709+00.582	37.3	0.2	51.3	29.3	18.6	
58	AGAL332.094–00.421	46.5	0.2	35.3	1.1	1.1	
59	AGAL332.826–00.549	85.2	0.3	73.6	13.3	11.2	*
60	AGAL333.134–00.431	91.3	0.2	76.8	14.1	11.9	*

Table A.7: continued.

ID	CSC Name	$T_{\text{ex}}$	$\sigma_T$	$T_{\text{ex,gauss}}$	$\sigma_{T+}$	$\sigma_{T-}$
61	AGAL333.284–00.387	67.4	0.2	72.8	0.7	0.7
62	AGAL333.314+00.106	35.8	0.2	38.1	7.8	8.0
63	AGAL333.604–00.212	140.5	0.2	136.3	1.2	1.2
64	AGAL333.656+00.059	21.9	0.2	22.4	7.6	8.9
65	AGAL335.789+00.174	40.3	0.2	49.3	27.8	29.8
66	AGAL336.958–00.224	21.7	0.3	20.9	3.5	3.7
67	AGAL337.176–00.032	30.0	0.2	29.9	5.2	5.4
68	AGAL337.258–00.101	22.4	0.2	21.8	0.3	0.3
69	AGAL337.286+00.007	15.2	0.3	14.2	0.9	1.0
70	AGAL337.406–00.402	61.6	0.6	95.4	31.0	31.3
71	AGAL337.704–00.054	41.7	0.3	45.5	6.4	5.6 *
72	AGAL337.916–00.477	68.9	0.4	76.4	0.3	0.3
73	AGAL338.066+00.044	17.4	0.3	18.6	2.1	2.3
74	AGAL338.786+00.476	17.1	0.2	17.4	0.3	0.3
75	AGAL338.926+00.554	51.4	0.2	62.3	37.5	23.4
76	AGAL339.623–00.122	42.5	0.3	42.6	12.2	12.6
77	AGAL340.374–00.391	17.1	0.3	18.3	4.7	5.6
78	AGAL340.746–01.001	32.9	0.2	34.1	17.6	20.1
79	AGAL340.784–00.097	21.4	0.2	23.5	2.5	2.6
80	AGAL341.217–00.212	42.8	0.2	51.9	11.2	11.4
81	AGAL342.484+00.182	27.4	0.2	27.1	1.1	1.1
82	AGAL343.128–00.062	68.0	0.2	75.3	0.6	0.6
83	AGAL343.756–00.164	31.5	0.2	34.1	14.1	15.3
84	AGAL344.227–00.569	34.1	0.3	37.4	2.2	2.3
85	AGAL345.003–00.224	63.4	1.0	86.9	30.5	30.8
86	AGAL345.488+00.314	59.6	0.3	61.6	10.2	8.7 *
87	AGAL345.504+00.347	63.4	0.3	67.0	145.2	141.7
88	AGAL345.718+00.817	26.3	0.2	27.3	3.1	3.2
89	AGAL351.131+00.771	26.5	0.2	30.6	0.2	0.2
90	AGAL351.161+00.697	89.9	0.2	99.1	0.1	0.1
91	AGAL351.244+00.669	112.8	0.2	126.5	16.3	16.3
92	AGAL351.416+00.646	84.5	1.0	105.7	19.2	19.3
93	AGAL351.444+00.659	62.2	0.2	81.2	45.1	46.1
94	AGAL351.571+00.762	19.7	0.4	19.6	0.5	0.5
95	AGAL351.581–00.352	40.4	0.4	49.0	4.3	4.3
96	AGAL351.774–00.537	74.1	0.9	88.0	9.1	9.1
97	AGAL353.066+00.452	28.7	0.2	13.2	4.9	3.6
98	AGAL353.417–00.079	15.5	0.3	32.9	16.5	11.0
99	AGAL354.944–00.537	16.6	0.3	20.6	8.9	6.2

**Notes.** The columns are as follows: (1)–(2) ID and CSC name of the source (given in Table A.1); (3)–(4) excitation temperature (in K) and its uncertainty derived from the peak intensity of the CO (6–5) spectra; (5)–(7) excitation temperature (in K) and its upper and lower uncertainty derived from the peak intensity of the Gaussian fit of the CO (6–5) spectra; (8) an asterisks indicates the cases where the Gaussian fit is dubious and, therefore, the excitation temperature was obtained from the relation  $\log(T_{\text{ex}}) = (0.75 \pm 0.10) + (0.21 \pm 0.02) \log(L_{\text{bol}})$  (see Sect. 4.4 for further details).

## Appendix B: CO spectra and CO (6–5) maps

In Fig. B.1 we show the integrated CO (6–5) maps towards the TOP100 sample together with the CO (4–3) spectra from FLASH<sup>+</sup> observations, the convolved CHAMP<sup>+</sup> mid-*J* CO spectra using a fixed beam size of 13''<sub>4</sub> and the isotopologue C<sup>17</sup>O (3–2) or C<sup>18</sup>O (2–1) spectra from Giannetti et al. (2014). The CO profiles that are not overlaid by the Gaussian fit correspond to those that were not properly fitted.

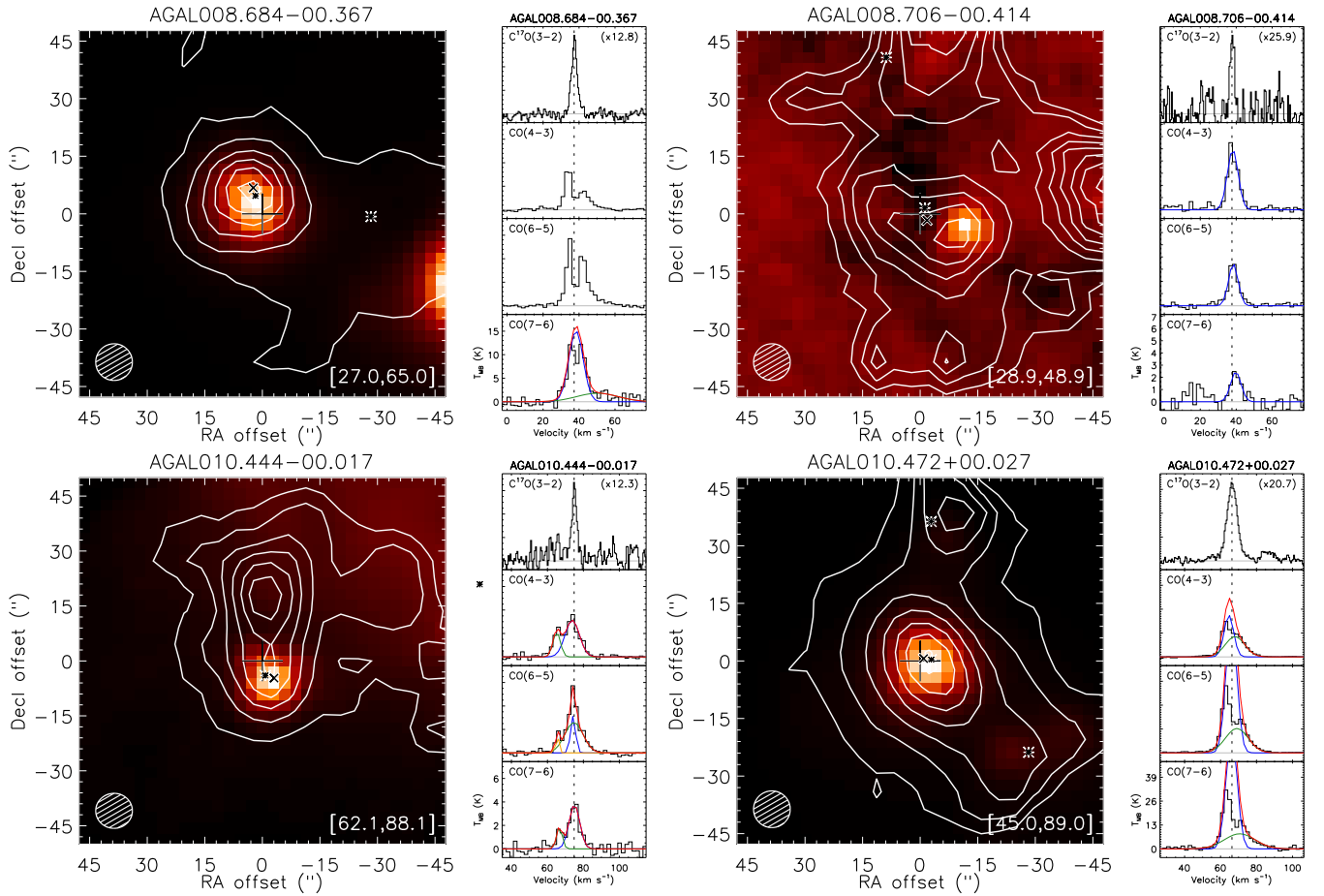


Fig. B.1: Left: False-colour *Herschel*/PACS images at 70 $\mu$ m overlaid by the CO (6–5) emission contours towards the TOP100 source. The CO contours correspond to the emission integrated over the full-width at zero power (FWZP) of the CO (6–5) profile, the velocity range shown in the bottom right side of the image, and the contour levels are shown from 20% to 90% of the peak emission of each map, in steps of 10%. The (0,0) position of the map is shown as a + symbol, the position of the CSC source from Contreras et al. (2013) is shown as a  $\times$  symbol and the dust continuum emission peaks from Csengeri et al. (2014) are shown as asterisks. Right, from top to bottom panel: C<sup>17</sup>O (2–1) or C<sup>18</sup>O (1–0) from Giannetti et al. (2014), CO (4–3), CO (6–5) and CO (7–6) profiles towards the TOP100 sample, convolved into a fixed beam size of 13''<sub>4</sub> (shown in black) and their fitted Gaussian components. The narrower Gaussian component fitted to the data is shown in blue, the second and broader component is shown in green and the third component is shown in yellow. The sum of all Gaussian components is shown in red, except for the cases where a single component was fitted. The vertical dashed black line is placed at the rest velocity ( $V_{\text{LSR}}$ ) of each source. The horizontal filled grey line displays the baseline of the data. *ArXiv only*: the full Fig. B.1 is available in the A&A version.

## Appendix C: Additional material

### Appendix C.1: Analysis of the mid-*J* CO emission in the distance-limited sub-sample

For completeness, in this section we present the analysis of the CO emission for the distance-limited sample (defined in Sect. 3.3).

Figure C.1 shows the average CO spectra per class integrated over a linear scale ( $\sim 0.24$  pc) for the distance-limited sub-sample. When compared to Fig. 6, which shows the same kind of spectra but for the full sample (using the spectra convolved to 13''<sub>4</sub>, see Sect. 3.3), we found that the IRw and IRb classes are much better separated in the distance-limited sample than in the full dataset smoothed to 13''<sub>4</sub>. In fact, the IRw and IRb gets less distinguishable when including the outlier IRw clumps located at  $d \geq 12$  pc (AGAL018.606–00.074, AGAL018.734–00.226, AGAL342.484+00.182).

Figure C.2 presents the CDF for CO (6–5) and CO (7–6) line luminosity.  $L_{\text{CO}}$  ranges from 2.7 to 284.0 K km s<sup>–1</sup> pc<sup>2</sup> for the CO (6–5) transition, and 1.2 to 276.5 K km s<sup>–1</sup> pc<sup>2</sup> for the CO (7–6) line. The KS tests indicate that the evolutionary classes are



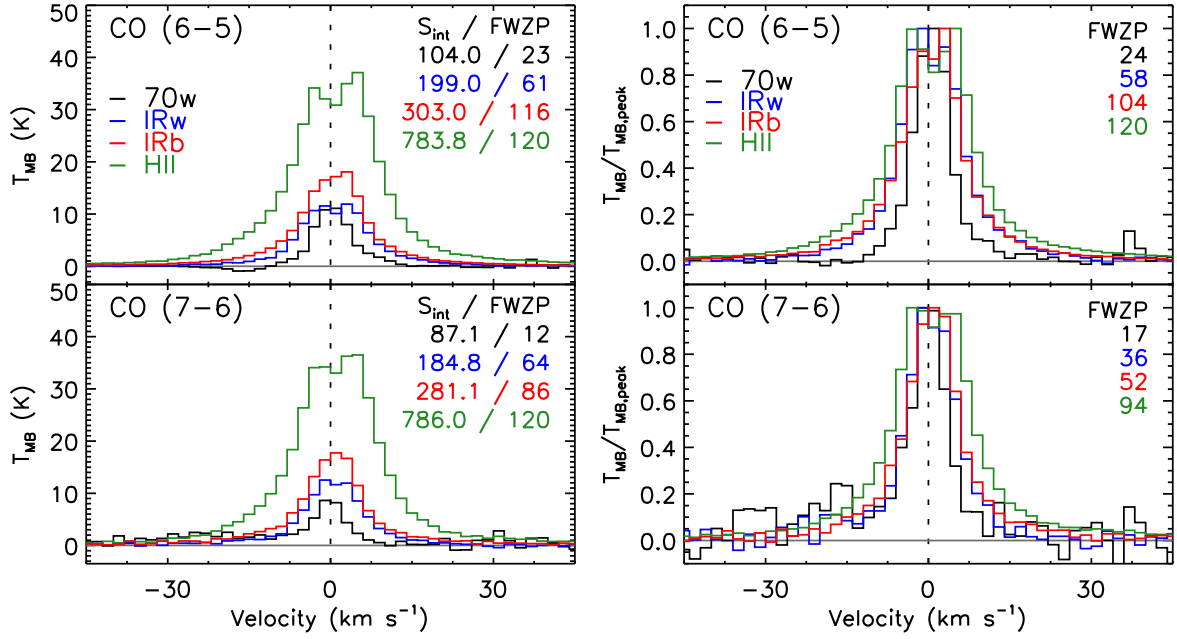


Fig. C.1: Left: Average CO (6–5) and CO (7–6) spectra of each ATLASGAL class scaled to the median distance of the distance-limited sub-sample ( $d=3.26$  kpc). Right: Same plot, but the average CO spectra were normalised by their peak intensity. The baseline level is indicated by the solid grey line. The black dashed line marks a velocity of  $0 \text{ km s}^{-1}$ . The FWZP of the profiles are shown in the upper right side of the panels (in  $\text{km s}^{-1}$  units), together with the integrated intensity ( $S_{\text{int}}$ , in  $\text{K km s}^{-1}$  units) of the CO profiles shown in the left panels.

Table C.1: Kolmogorov-Smirnov statistics of the mid- $J$  CO line luminosity for the distance-limited sub-sample as a function of the evolutionary class of the clumps.

Transition	70w-IRw	70w-IRb	70w-H II	IRw-IRb	IRw-H II	IRb-H II
CO (6–5)	0.60, $p < 0.001$	0.80, $p < 0.001$	0.95, $p < 0.001$	0.31, $p = 0.08$	0.71, $p \leq 0.001$	0.51, $p = 0.001$
CO (7–6)	0.73, $p < 0.001$	0.80, $p < 0.001$	1.00, $p < 0.001$	0.34, $p = 0.04$	0.68, $p \leq 0.001$	0.52, $p = 0.001$

**Notes.** The rank KS and its corresponding probability ( $p$ ) are shown for each comparison. A  $p$ -value of  $< 0.001$  indicate a correlation at 0.001 significance level.  $p$ -values of 0.05, 0.002 and  $< 0.001$  represent the  $\sim 2$ , 3 and  $> 3 \sigma$  confidence levels.

relatively more distinguishable based on the distance-limited sub-sample than on the full sample (excluding the comparison between IRw and IRb, all tests indicated ranks  $\text{KS} \geq 0.51$ , with  $p \leq 0.001$  for both  $J$  transitions, see Table C.1).

We also looked at the CO (6–5) and CO (7–6) line luminosities as function of the bolometric luminosity of the sources (see right panel of Fig. C.2), their mass and their luminosity-to-mass ratio (See Fig. C.3). Table C.2 lists the Spearman correlation factor,  $\rho$ , and its associated probability,  $p$ , for the CO line luminosity versus the bolometric luminosity, the clump mass and the luminosity-to-mass ratio of the clumps. For  $L_{\text{bol}}$  and  $M_{\text{clump}}$ , the partial Spearman rank, excluding the dependency on the distance, is also provided. The  $\rho$  values are similar to those reported on Table 8 for the correlation between  $L_{\text{CO}}$  and  $L_{\text{bol}}$ , based on the 13''4 dataset, indicating no significant improvement on the correlation between these quantities. The correlation with  $M_{\text{clump}}$ , however, is weaker ( $\rho \leq 0.44$ ,  $p < 0.001$ ) than the one found towards the 13''4 dataset ( $\rho \geq 0.72$ ,  $p < 0.001$ , see Table 8). The weaker correlation between  $L_{\text{CO}}$  and  $M_{\text{clump}}$  on the distance-limited sub-sample might arise from the fact that the CO line luminosity is integrated over only a fraction of the beam used for estimating the mass of the clumps. Indeed König et al. (2017) used a minimum aperture size of  $55''1$  for their study, while the minimum beam size adopted for the convolution of the CO was about  $10''$  (see Sect. 3.3).

We also found that  $L_{\text{CO}}$  is relatively better correlated with  $L/M$  for the distance-limited dataset ( $\rho \geq 0.67$ ,  $p < 0.001$  for all lines, see Table C.2) rather than the 13''4 spectra ( $\rho \leq 0.50$ ,  $p \leq 0.003$  for the mid- $J$  CO lines, see Table 8).

We compared the best fits obtained for the mid- $J$  CO line luminosity convolved to the same linear scale with those derived using the 13''4 data. Table C.3 reports the coefficients of the individual fits. We find that  $L_{\text{CO}}$  vs.  $L_{\text{bol}}$  follows a power-law distribution with indices of  $0.53 \pm 0.03$  and  $0.59 \pm 0.03$  for the CO (6–5) and CO (7–6) lines, respectively. Such power-law distributions are relatively less steeper than those derived towards the 13''4 dataset, with indices of  $0.61 \pm 0.03$  and  $0.67 \pm 0.03$  for the same  $J$  transitions (see Table 7). The offset of the fits indicates the brightness of the CO emission is roughly 0.4 dex larger than the  $L_{\text{CO}}$  values derived using the spectra convolved to a 13''4 beam. At least for the closest sources, such an increment in  $L_{\text{CO}}$  is expected due to the larger size of the beam corresponding to 0.24 pc. For example, at  $d = 1.85$  kpc, the linear scale of 0.24 pc corresponds to a beam of  $26''8$ , which is sampling an area 4 times larger than the 13''4 dataset.

Finally, we further investigated the effects of beam dilution on our results by integrating the CO emission over the full maps for those clumps where the aperture used by König et al. (2017) to derive the bolometric luminosity of the clumps,  $\Delta\theta_{\text{ap}}$ , was larger or equal to the CO emission extension ( $\Delta\theta \leq \Delta\theta_{\text{ap}}$ ). Such criterion was satisfied for 92 of the 99 clumps. The best fit of the

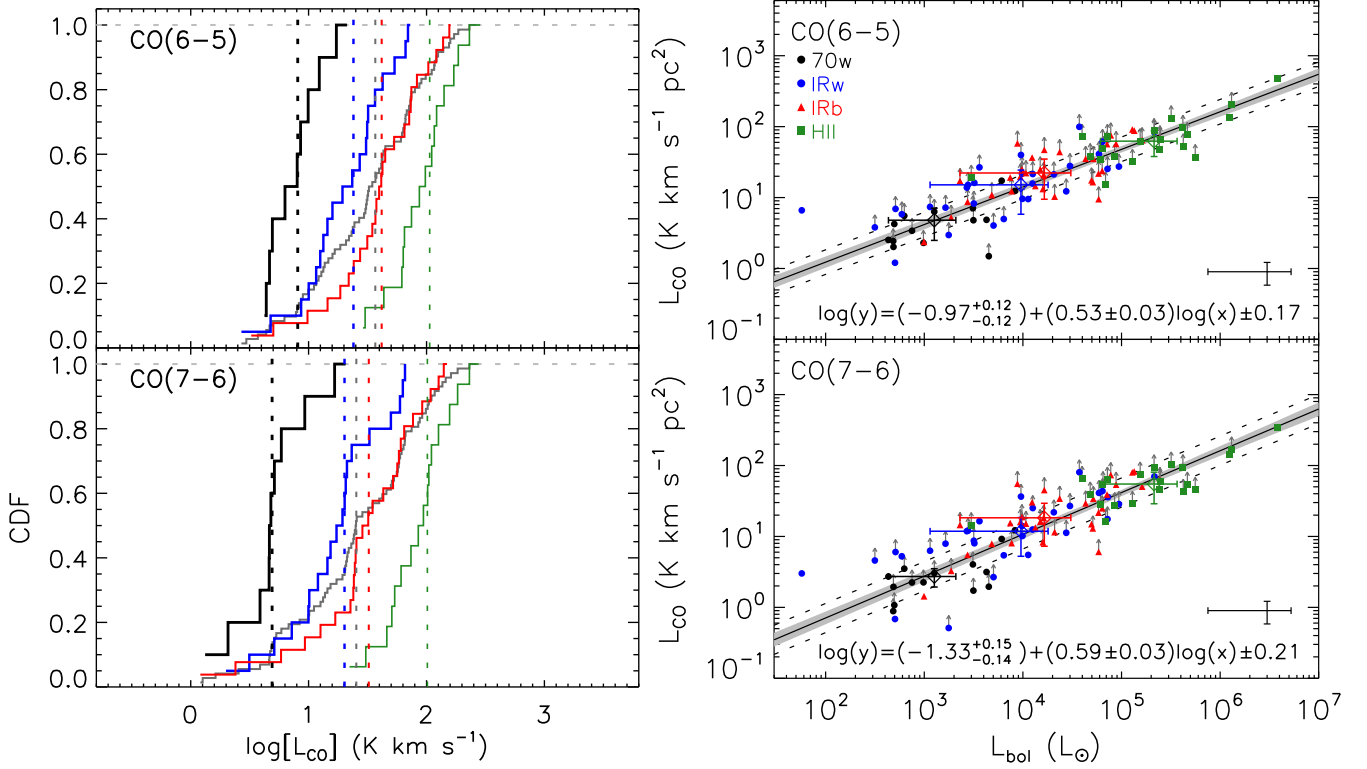


Fig. C.2: Left panels: Cumulative distribution function (CDF) of the CO line luminosity derived using the spectra convolved to the same linear scale of 0.24 pc. The median values per class are shown as vertical dashed lines in their corresponding colours. Right: Line luminosity of the same CO lines versus the bolometric luminosity of the TOP100 clumps in distance-limited sub-sample. The median values for each class are shown as open diamonds and their error bars correspond to the absolute deviation of the data from their median value. Points having an upward arrow indicate a self-absorption feature in the spectrum and correspond to a lower limit. The typical error bars are shown in the bottom right side of the plots. The black solid line is the best fit, the light grey shaded area indicates the 68% uncertainty, and the dashed lines show the intrinsic scatter ( $\epsilon$ ) of the relation.

Table C.2: Spearman rank correlation statistics for the CO line luminosity as a function of the clump properties towards the distance-limited sub-sample.

Property	CO(6-5)	CO(7-6)
$L_{\text{bol}}$	0.86, $p < 0.001$ ; $\rho_p = 0.91$	0.87, $p < 0.001$ ; $\rho_p = 0.88$
$M_{\text{clump}}$	0.44, $p < 0.001$ ; $\rho_p = 0.85$	0.41, $p < 0.001$ ; $\rho_p = 0.81$
$L/M$	0.67, $p < 0.001$	0.79, $p < 0.001$

**Notes.** The rank  $\rho$  and its corresponding probability ( $p$ ) are shown for each comparison. A  $p$ -value of  $< 0.001$  indicate a correlation at 0.001 significance level.  $p$ -values of 0.05, 0.002 and  $< 0.001$  represent the  $\sim 2$ , 3 and  $> 3$   $\sigma$  confidence levels. For  $L_{\text{bol}}$  and  $M_{\text{clump}}$ , the partial correlation coefficient,  $\rho_p$ , is also shown.

Table C.3: Parameters of the fits of  $L_{\text{CO}}$ , extracted within a common linear scale, as a function of the clump properties.

Transition	Property	$\alpha$	$\beta$	$\epsilon$
CO(6-5)	$L_{\text{bol}}$	$-0.97^{+0.12}_{-0.12}$	$0.53 \pm 0.03$	0.17
	$M_{\text{clump}}$	$-0.18^{+0.24}_{-0.23}$	$0.48 \pm 0.08$	0.43
	$L/M$	$0.68^{+0.05}_{-0.06}$	$0.54 \pm 0.05$	0.32
CO(7-6)	$L_{\text{bol}}$	$-1.33^{+0.15}_{-0.14}$	$0.59 \pm 0.03$	0.21
	$M_{\text{clump}}$	$-0.26^{+0.26}_{-0.29}$	$0.47 \pm 0.08$	0.51
	$L/M$	$0.47^{+0.06}_{-0.06}$	$0.64 \pm 0.05$	0.32

**Notes.** The fits were performed by adjusting a model with three free parameters in the form of  $\log(y) = \alpha + \beta \log(x) \pm \epsilon$ , where  $\alpha$ ,  $\beta$  and  $\epsilon$  correspond to the intercept, the slope and the intrinsic scatter, respectively.

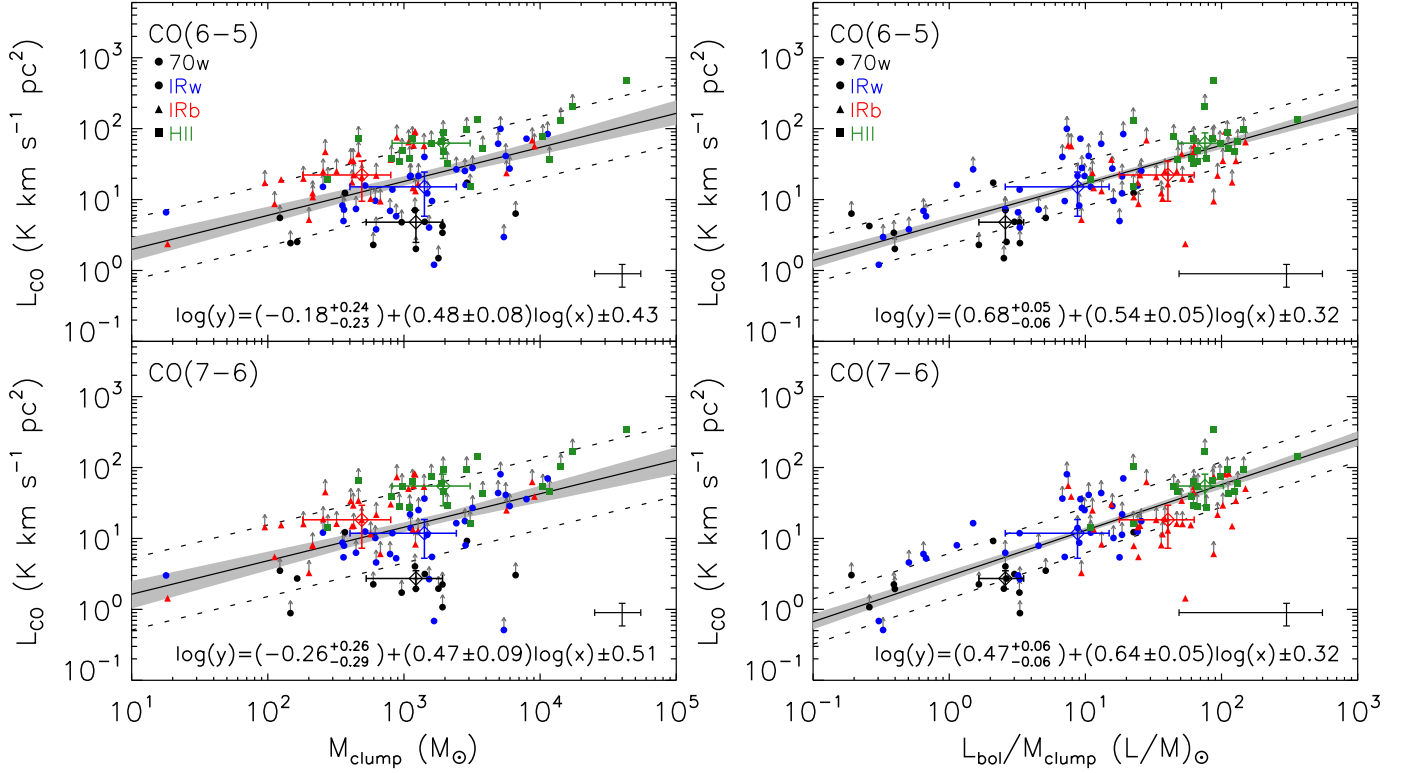


Fig. C.3: The CO line luminosity derived using the spectra convolved to the same linear scale of 0.24 pc are shown versus their masses (left panels) and their luminosity-to-mass ratios (right). For a complete description of the plots, see Fig. C.2.

data indicates that  $L_{\text{CO}}$  increases with  $L_{\text{bol}}$  with a power-law index of  $0.59 \pm 0.03$  and  $0.68^{+0.05}_{-0.06}$  for the CO(6–5) and CO(7–6) transitions, consistently with the results based on the 13'4 dataset (see Fig. 7). Similar results are also found when comparing  $L_{\text{CO}}$  versus  $M_{\text{clump}}$  and  $L/M$ . The overall results suggests that the analysis of the mid- $J$  CO emission is robust in terms of beam dilution effects.

Table C.4: Spearman statistics for the CO line luminosity as a function of the clump properties using the spectra integrated on the whole CHAMP<sup>+</sup> maps.

Transition	$L_{\text{bol}}$	$M_{\text{clump}}$	$L/M$
CO(6–5)	0.84, $p < 0.001$ $\rho_p = 0.96$	0.72, $p < 0.001$ $\rho_p = 0.93$	0.43, $p < 0.001$
CO(7–6)	0.82, $p < 0.001$ $\rho_p = 0.97$	0.59, $p < 0.001$ $\rho_p = 0.94$	0.49, $p < 0.001$

**Notes.** The rank  $\rho$  and its corresponding probability ( $p$ ) are shown for each comparison. A  $p$ -value of  $< 0.001$  indicates a correlation at 0.001 significance level.  $p$ -values of 0.05, 0.002 and  $< 0.001$  represent the  $\sim 2$ , 3 and  $> 3\sigma$  confidence levels.

### Appendix C.2: Analysis of the CO emission using the Gaussian profiles

We further investigated the effects of self-absorption by computing the CO line luminosities using the integrated flux over the Gaussian fit of the CO profiles (see Sect. 3.5). Then, we compared the Gaussian CO luminosities with the clump properties and compared the results with those reported in Sect. 4.3.

First, we checked the correlation between the Gaussian  $L_{\text{CO}}$  values and the clump properties by means of their Spearman rank correlation factor. The results are summarised in Table C.5. When compared to the Spearman factors of the observed CO line luminosity against the clump properties (see Table 8), we found a slight improvement on the correlation between  $L_{\text{CO}}$  and the bolometric luminosity of the clumps (e.g. for the CO(6–5) line, the correlation slightly improves from  $\rho = 0.85$  to 0.88), and with their  $L/M$  ratio (e.g. from  $\rho = 0.46$  to 0.49 for the same transition). No significant changes in the correlation between  $L_{\text{CO}}$  and  $M_{\text{clump}}$  were found (e.g. from  $\rho = 0.72$  to 0.74 for the CO(6–5) line), indicating that the observed correlation is likely dependent on the distance rather than the mass of the clumps.

Figure C.4 presents the distribution of the Gaussian CO line luminosities as a function of the clump properties. The parameters of the fits are summarised in Table C.6. Although the distribution of the points indicates higher correlation with  $L_{\text{bol}}$  and  $L/M$ , the steepness of the relations are consistent with those reported in Sect. 4.3. For example, the slope of the best fit of  $L_{\text{CO}}$  against  $L_{\text{bol}}$  is

Table C.5: Spearman rank correlation statistics for the CO line luminosity as a function of the clump properties towards the TOP100 sample for the observed and the Gaussian CO luminosities.

Property	Observed $\rho$ / Gaussian $\rho$		
	CO(4–3)	CO(6–5)	CO(7–6)
$L_{\text{bol}}$	0.71 / 0.78	0.85 / 0.88	0.89 / 0.90
$M_{\text{clump}}$	0.75 / 0.77	0.72 / 0.73	0.69 / 0.69
$L/M$	0.29 / 0.34	0.46 / 0.49	0.50 / 0.54

**Notes.** The rank  $\rho$  are shown for each comparison between the observed and Gaussian CO luminosities ratio (Observed/Gaussian). The corresponding probability ( $p$ ) of most comparisons are  $p < 0.001$ , except for the comparison between the CO(4–3) luminosity vs  $L/M$  ( $p = 0.09$ ). A  $p$ -value of  $< 0.001$  indicate a correlation at 0.001 significance level.  $p$ -values of 0.05, 0.002 and  $< 0.001$  represent the  $\sim 2$ , 3 and  $> 3\sigma$  confidence levels.

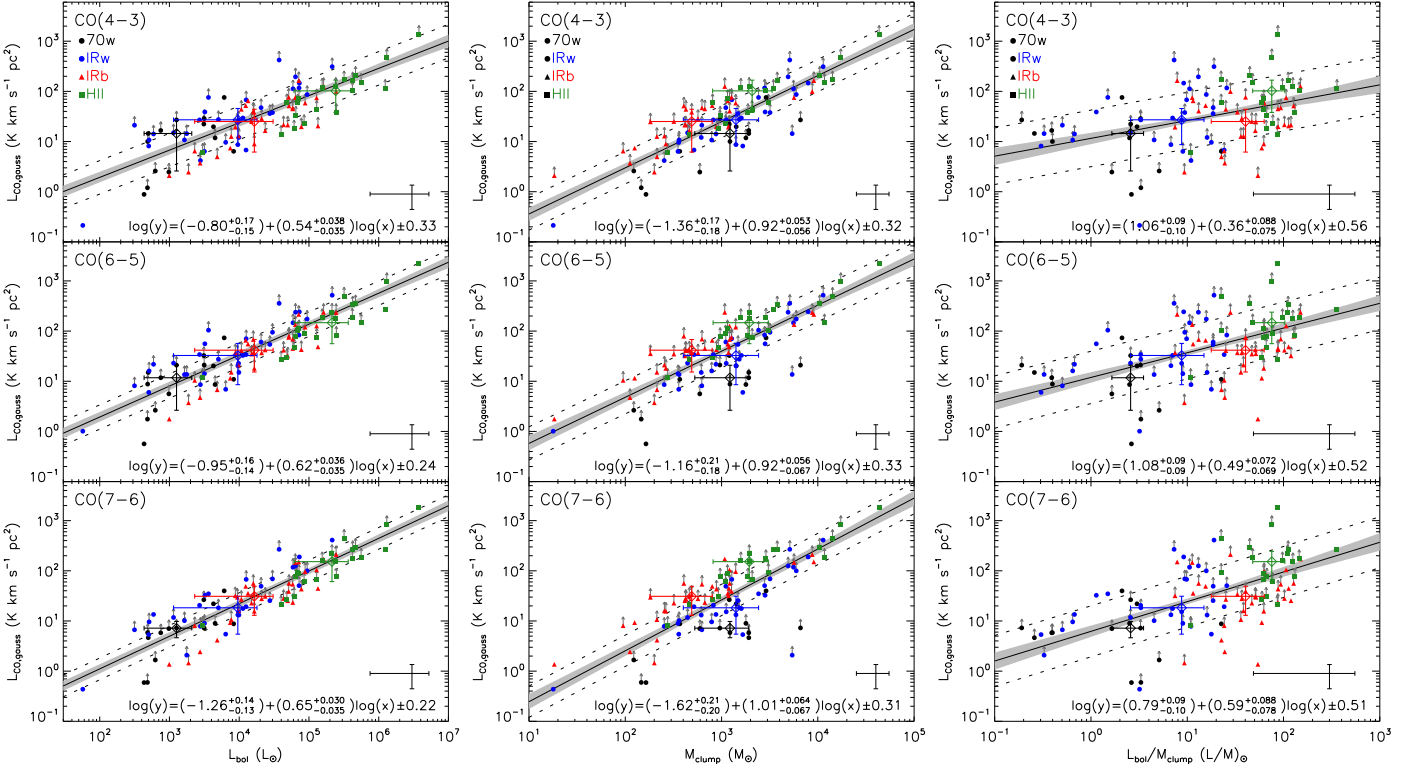


Fig. C.4: Line luminosity of the CO(4–3) (upper panels), CO(6–5) (middle) and CO(7–6) emission (bottom) versus the bolometric luminosity (left panels), the mass of the clumps (middle) and the  $L/M$  ratio (right) of the TOP100 sources. The median values for each class are shown as open diamonds and their error bars correspond to the absolute deviation of the data from their median value. Points having an upward arrow indicate a self-absorption feature in the spectrum convolved to  $13''/4$  and correspond to a lower limit. The typical error bars are shown at the bottom right side of the plots. The black solid line is the best fit, the light grey shaded area indicates the 68% uncertainty, and the dashed lines show the intrinsic scatter ( $\epsilon$ ) of the relation.

$0.63 \pm 0.04$  for the observed  $L_{\text{CO}}$  values, and  $0.62 \pm 0.04$  for the Gaussian CO luminosities, respectively. These findings suggest that the relations between the CO line luminosities and the clump properties are robust in terms of the self-absorption observed in the CO spectra of the TOP100.

### Appendix C.3: Integrated CO intensity maps of the secondary Gaussian components

Figure C.5 presents the  $870\ \mu\text{m}$  LABOCA maps towards five TOP100 clumps displaying secondary CO peaks in their spectra. The integrated CO(6–5) distribution of the two velocity components clearly shows that the two components trace different structures in the observed field.

Table C.6: Parameters of the fits of  $L_{CO}$  as a function of the clump properties for the Gaussian fluxes.

Transition	Property	$\alpha$	$\beta$	$\epsilon$
CO (4–3)	$L_{bol}$	$-0.80^{+0.17}_{-0.15}$	$0.54 \pm 0.04$	0.33
	$M_{clump}$	$-1.36^{+0.17}_{-0.18}$	$0.92 \pm 0.06$	0.32
	$L/M$	$1.06^{+0.09}_{-0.10}$	$0.36 \pm 0.09$	0.56
CO (6–5)	$L_{bol}$	$-0.95^{+0.16}_{-0.14}$	$0.62 \pm 0.04$	0.24
	$M_{clump}$	$-1.16^{+0.21}_{-0.18}$	$0.92 \pm 0.07$	0.33
	$L/M$	$1.08^{+0.09}_{-0.09}$	$0.49 \pm 0.07$	0.52
CO (7–6)	$L_{bol}$	$-1.26^{+0.14}_{-0.13}$	$0.65 \pm 0.03$	0.22
	$M_{clump}$	$-1.62^{+0.21}_{-0.20}$	$1.01 \pm 0.07$	0.31
	$L/M$	$0.79^{+0.09}_{-0.10}$	$0.59 \pm 0.09$	0.51

**Notes.** The fits were performed by adjusting a model with three free parameters in the form of  $\log(y) = \alpha + \beta \log(x) \pm \epsilon$ , where  $\alpha$ ,  $\beta$  and  $\epsilon$  correspond to the intercept, the slope and the intrinsic scatter, respectively.

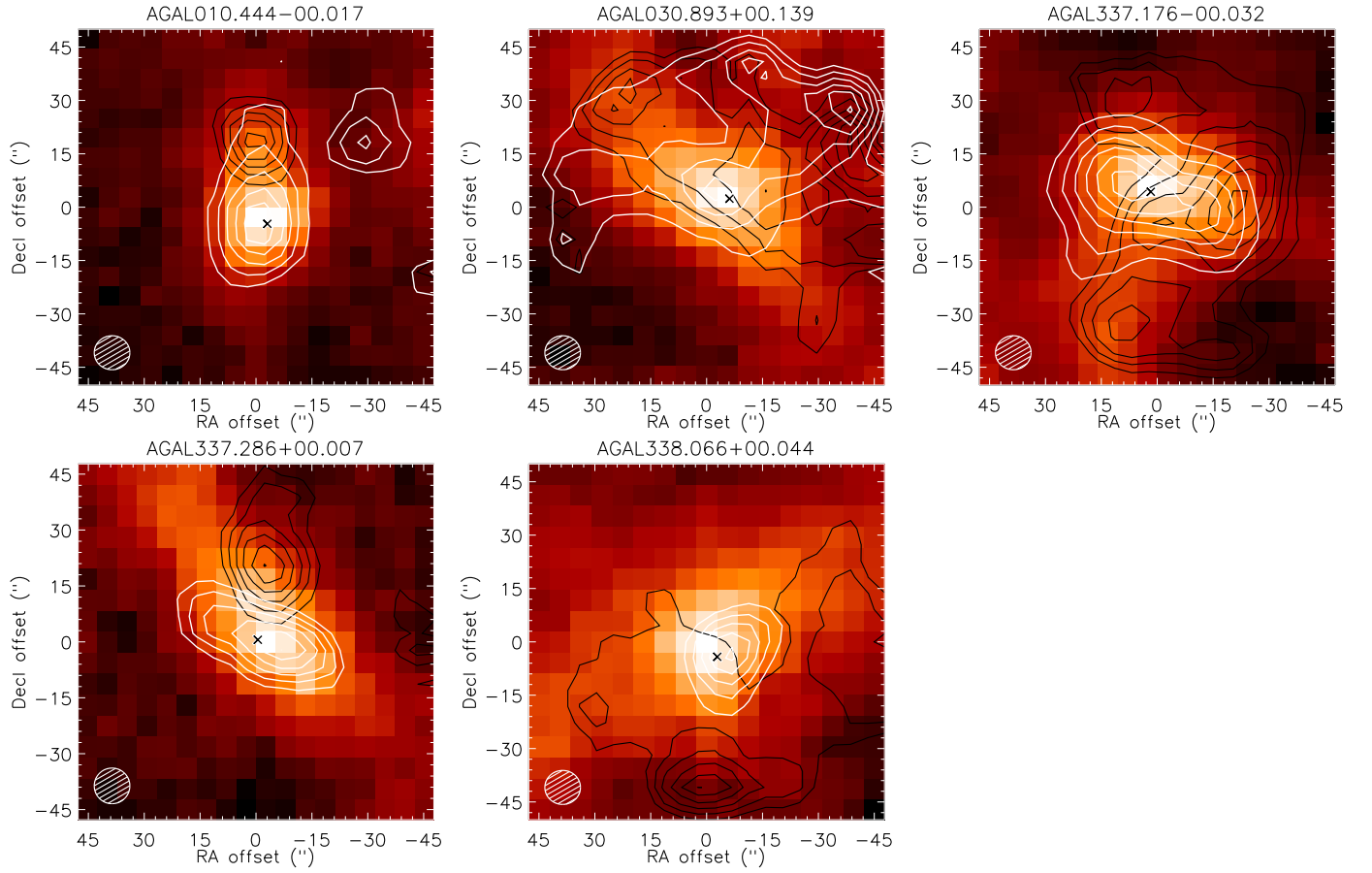


Fig. C.5: APEX-LABOCA images at  $870 \mu\text{m}$  overlaid by the CO (6–5) emission contours (C1 component in white, C2 component in black; in both cases, the contours are from 30% to 90% of the peak emission of the corresponding component in steps of 10%) towards the TOP100 clumps. The position of the CSC source from Contreras et al. (2013) is shown as a  $\times$  symbol.